

# **Composites of Nanoporous Gold and Polymer**

Dem Promotionsausschuss der  
Technischen Universität Hamburg-Harburg  
zur Erlangung des akademischen Grades  
Doktor-Ingenieur(in) (Dr.-Ing.)  
genehmigte Dissertation

Von

**Ke Wang**

Aus

Guizhou, China

2015

Gutachter:

Prof. Dr. -Ing. Jörg Weissmüller, Technische Universität Hamburg-Harburg

Prof. Dr. -Ing. Bodo Fiedler, Technische Universität Hamburg-Harburg

Vorsitzender des Prüfungsausschusses:

Prof. Dr. Stefan Müller, Technische Universität Hamburg-Harburg

Tag der mündlichen Prüfung: 23.03.2015





# Acknowledgements

It is my pleasure to thank the people who made this doctoral thesis possible.

First and foremost, I would like to express my sincere gratitude to Prof. Dr.-Ing. Jörg Weissmueller, my Ph.D supervisor, for his kind guidance, enthusiastic encouragement and immense knowledge, for his continuous support of my Ph.D study and research. Without his enlightening instruction, impressive kindness and patience, I could not have completed my thesis. His keen and vigorous academic observation enlightens me not only in this thesis but also in my future study.

I shall extend my thanks to Dr. Jürgen Markmann, who has helped me in many ways, not only for academic comments but also for an invaluable friendship.

I gratefully acknowledge the help of Mr. Rainer Behn for his help in doing compression test and with building the tension test specimen holders. Special thanks to Dr. Hans Jelitto from the institute of Advanced Ceramics at Hamburg University of Technology for using four point-bending test and valuable discussions. Dr. Manuel Grewer at Saarland University, Germany, is thanked for the measuring of the elastic modulus using ultrasonic velocity. I gratefully acknowledge the help of Dr. Martin Ritter from Central Division Electron Microscopy at Hamburg university of Technology in obtaining professional transmission electron micrographs of my samples. My grateful thanks are also extended to Dr. Markus Ziehmer from Institute of Materials Research at Helmholtz-Zentrum Geesthacht (HZG), Germany, for his help in doing the atomic force microscopy, to Mrs. Claudia Plaumann for her help in doing light microscopy measurements and to Mr. Jens Timmermann for his help in doing scanning electron microscope.

I would also like to express my thanks to all my colleagues and friends at Hamburg University of Technology, for giving me the help and sharing their knowledge and expertise. Also special thanks to Dr. Robert Günther and Dr. Jürgen Markmann, who provided critical comments on my thesis.

And many thanks to whoever helped in any way contributing to this thesis.

Last but not least, I want to thank my husband and my parents for their love, patience, support and understanding throughout my research.



# Abstract

Experimental investigations of the strength of small objects — such as micropillars or nanowires — point towards a trend of increasing strength with decreasing dimension,<sup>[1-3]</sup> approximating the theoretical shear strength when the size drops to the lower nanometer region.<sup>[1-4]</sup> Nanoporous metal synthesis via dealloying<sup>[5-7]</sup> provides mm- or cm-sized monolithic samples consisting of a homogeneous network structure of nanoscale “ligaments” with uniform size that can be controlled down to well below 10 nm.<sup>[8-10]</sup> The strength of the ligaments increases with decreasing size, attaining the theoretical strength of the metal at ligament diameters in the lower nanometer region.<sup>[3, 11]</sup> This high strength at the nanoscale, along with the low mass density of porous metals, suggests a search for design strategies that yield strong, lightweight composite materials by exploiting the mechanical properties of metal nanostructures.

Nanoporous gold(npg) can be deformed to large plastic strain in compression, in contrast to many other nanomaterials that fail after few percent of deformation.<sup>[12]</sup> The deformability of npg may be understood from the macroscopic constitutive behavior. Yet, the absence of transverse plastic strain in the macroscopic nanoporous metal implies that compression under uniaxial stress is completely carried by densification of the network of ligaments. The densification causes work hardening at the macroscopic scale, promoting stable and uniform plastic flow in compression. Yet, the same argument also points at the central deficiency of nanoporous metals as structural materials: Plastic flow under tensile loading reduces the density, resulting in work softening and, hence, in shear instability and brittle failure. Thus, in spite of the high local strength of the nanoscale ligaments, nanoporous gold is poorly suited to be applied as structural material. Obviously, ductilization of the material requires, first and foremost, a materials design that prevents the density change under load.

In this work, it shows that nanoporous gold made by alloy corrosion can be vacuum-impregnated with polymer to produce an interpenetrating phase nanocomposite that is reinforced by an interconnected network of metal nanostructures. The mechanical behavior including tensile ductility and plastic deformation of this novel nanocomposite material with various interpenetrating polymer phase were systematically explored. The tensile and compression tests have been carried out to study the mechanical behavior of the composite material in comparison with its constituent nanoporous gold and polymer materials. Compared to the deformation behavior of npg, the composite can suppress the densification during the compression deformation. It is found that the composite has a significant improvement of tensile ductility of npg and a drastic increasing of strength in both tension and compression case.

The mechanical tests demonstrate that impregnation with a polymer is an efficient way of reducing the density change during plastic flow under uniaxial load and results in a drastic reduction of the tension/compression anisotropy of the work hardening. The interpenetrating nanocomposite material which is thus formed has an isotropic microstructure and exhibits a number of unusual and technologically attractive properties, specifically ductility in tension, the option of cold-forming, high electric conductivity and a strength significantly exceeding that of each of the constituent phases. The finding validates a novel materials design strategy that exploits the trend of “smaller is stronger” in metal nanostructures by incorporating them as reinforcement into a bulk composite material. Future studies promise insights into size- and interface or interphase effects on the mechanical properties of the metallic and the polymer phases, as well as progress towards a new class of strong, ductile and electrically conductive nanocomposites.



# Contents

<b>Abstract.....</b>	<b>III</b>
<b>Chapter 1. Introduction .....</b>	<b>1</b>
1.1 Motivation .....	1
1.2 Scope and structure of this work .....	3
1.3 State of the art.....	4
1.3.1 Dealloying .....	4
1.3.2 Introduction of nanoporous gold .....	8
1.3.3 Traditional composite materials .....	14
1.3.4 Interpenetrating phase composites .....	17
<b>Chapter 2. Experimental procedures .....</b>	<b>21</b>
2.1 Nanoporous gold.....	21
2.1.1 Bulk alloy preparation .....	21
2.1.2 Dealloying and tuning the ligament size .....	21
2.2 Nanoporous gold-polymer composites .....	22
2.2.1 Introduction of vacuum impregnation method.....	22
2.2.2 Introduction of polymer .....	23
2.2.3 Polymers used .....	24

2.2.4	Vacuum impregnation procedure .....	25
2.3	Measurement procedure and setups.....	26
2.3.1	Scanning electron microscope and energy-dispersive x-ray analysis .....	26
2.3.2	Dilatometry.....	26
2.3.3	Transmission electron microscope .....	26
2.3.4	Atomic force microscopy .....	27
2.3.5	Dynamic mechanical analysis .....	27
2.3.6	Resistance meter.....	28
2.3.7	Vickers microhardness test.....	28
2.3.8	Instrumented indentation test .....	29
2.3.9	Compression test .....	30
2.3.10	Three-point bending test.....	30
2.3.11	Tensile test.....	31
2.3.12	Four-point bending test .....	32
2.3.13	Load-unload compression test.....	33
<b>Chapter 3.</b>	<b>Characterization.....</b>	<b>34</b>
3.1	Characterization of microstructure .....	34
3.2	Electrical properties .....	39
3.3	Thermal properties.....	39
<b>Chapter 4.</b>	<b>Plastic deformation .....</b>	<b>43</b>
4.1	Compression .....	43
4.1.1	Experimental results .....	43
4.1.2	Discussion .....	51
4.2	Tension .....	58
4.2.1	Experimental results .....	58
4.2.2	Discussion .....	64
<b>Chapter 5.</b>	<b>Elastic deformation: A preliminary study .....</b>	<b>67</b>
5.1	Experimental results .....	67
5.1.1	Instrumented indentation tests.....	67
5.1.2	Load-unload compression tests .....	68

5.1.3	Dynamic mechanical analysis .....	70
5.2	Discussion.....	71
5.2.1	Elastic modulus of npg .....	71
5.2.2	Elastic modulus of composite .....	72
<b>Chapter 6.</b>	<b>Summary and outlook.....</b>	<b>74</b>
<b>Reference.....</b>		<b>79</b>



# Chapter 1.

## Introduction

### 1.1 Motivation

A body of research carried out on small objects, for example nanowires or micropillars, mostly presents a major trend of decreasing dimension with increasing strength.<sup>[1-3]</sup> It approximates the theoretical shear strength that is present at a moment when the size decreases to the lower nanometer region.<sup>[1-4]</sup> The observation of theoretical strength in defect-free crystals, such as whiskers, irrespective of their size exemplifies that the trend of “smaller is stronger” is related to the defect structure.<sup>[13-15]</sup> The interaction of dislocations with the surface is another important factor, as is evidenced by in-situ observation of large recoverable flow-stress changes during interfacial charging or electro sorption.<sup>[16]</sup> Regardless of its microscopic source, the presence of such a high strength in small size objects implies a need for design solutions that could offer high-strength materials by making use of mechanical properties of metal nanostructures. In this case, synthesis via dealloying can offer a solution to the major problem, namely, how to assemble a high number of nanoscale objects ( $10^{18}$  for  $1 \text{ cm}^3$  of material with a structure size of 10 nm) into a macroscopic object.<sup>[5, 6, 17]</sup> Nanoporous metals made by dealloying take the form of monolithic bodies consisting of an interconnected network of nanoscale ‘ligaments’ in a polycrystalline microstructure with typically 10 to 100  $\mu\text{m}$  grain size<sup>[18, 19]</sup>. Each micron-sized grain is nanoporous, so that neighboring ligaments share the same crystal lattice. In other words, the local structure in volumes of, for instance,  $1 \mu\text{m}^3$ , is that of a single crystal containing a contiguous nanoscale pore network. The mechanical behavior of these materials obeys scaling

equations derived for foams with macroscopic porosity, and the local strength of the ligaments follows the same<sup>[3, 11, 20, 21]</sup> or similar<sup>[19, 22]</sup> trends as individual nanowires. The material is under study as a model material for clarifying the deformation mechanisms and mechanical properties of small metal bodies such as nanowires or nanopillars.

Nanoporous gold (npg) made by dealloying has attracted a lot of interest due to its unique mechanical and electrical properties<sup>[3, 11]</sup> and its wide variety of applications in actuation<sup>[23, 24]</sup>, sensing<sup>[25, 26]</sup>, and catalysis<sup>[27, 28]</sup>. Previous researchers have revealed extremely large local strength of the individual ligaments<sup>[11]</sup> and excellent compressive ductility of macroscopic nanoporous gold samples<sup>[19]</sup>. While microscale and more recently macroscale nanoporous gold samples show excellent deformability in compression, studies so far have invariably indicated brittle failure in tension. This behavior has been linked to a tension-compression asymmetry of the mechanical behavior of porous bodies: While densification of the network implies work hardening in compression, density loss in tension results in work softening. This latter behavior implies a plastic instability with shear localization and brittle failure in tension. Structural applications of nanoporous gold generally have been limited to the absence of tensile ductility caused by the density changing under loading<sup>[16, 29]</sup>. Obviously, a materials design that prevents the density change under load is necessary for requires of ductilization of the material.

Metallic nanoporous materials are sometimes regarded as the type of composite where the air phase in the pores is considered to be the second phase.<sup>[30]</sup> Nevertheless, the relatively low influence of the gas phase in the pores on the foams' properties attracts few attentions to the research on the second phase's effects. A majority of studies on mechanical properties of porous metals concentrated on the deformation of solid matrix in compression as well as in tension. Another vital research topic has been volume fraction and dimension and morphology of the ligaments.<sup>[11, 21, 31-35]</sup> However, it is still important to note that the influence of the second phase on the metal foams' properties may still be of great significance if the gas phase is substituted. Jin and Weissmueller<sup>[16]</sup> demonstrated a hybrid material concept that designed a hybrid nanostructure consisting of porous metal that is interpenetrated by an electrolyte as the second component. By polarizing the internal interface via an applied electric potential, the material's strength and ductility can thus be matched to altering requirements in service. The concept allows the user to select, for instance, a soft and ductile state for processing and a high-strength state for service as a structural material.

It can be assumed that if a lightweight, ductile phase, such as polymer, is used to fill the pores, it will make the effects of the second phase more significant. This method yields a composite referred to as interpenetrating phase composite. It is a more advanced kind of nanostructure composite characterized by the component materials that are in a co-continuous state. The composite are composed of two different material classes (for instance polymer, metal or ceramic) that are combined on a macroscopic level. Each of the interpenetrating component materials is characterized by different unique properties. Synergetic effects are expected with the approach of interpenetrating nanocomposites, in other words, relevant properties may be having higher values as well as some additional traits and new property combinations may be realized.

In this work, impregnation of the nanoporous metal with a polymer is explored as a method that can help achieve a major goal that is to realize high-strength and ductilization of composite material so that it can serve as a structural material. The interpenetrating nanoporous metal-polymer composite material which is thus formed is expected to have various novel properties.

## 1.2 Scope and structure of this work

This work introduces an approach to generate an interpenetrating phase nanocomposite material that combines this high-strength and uniform metallic network structure with an interpenetrating polymer phase. Nanoporous gold is used as host foam and the entire interconnected pore structure was vacuum-impregnated with different kinds of polymer. The present research concentrates on investigating the properties of composites compared to their constituent materials, polymer and nanoporous gold. A systematic study is necessary to fully explain and understand the structure-property relations for npg-polymer composites and native npg. Another issue to be explored is the way the ligament size and structure of nanoporous gold as well as the different interpenetrating phase of polymer influences the mechanical traits of composites, in particular tensile ductility. All of the above mentioned problems will be addressed in the following chapters.

The electrochemical technology is applied for preparation of pure npg host foam throughout this work. The fundamental principles of electrochemistry and the basic introduction of structure, properties and structure-property relations of npg will be described in the third section of Chapter 1. The general introduction and literature review about different type of composites will be also introduced in the third section of Chapter 1.

The detailed experimental procedures will be described in Chapter 2, including the samples preparation, characterization and corresponding mechanical measurement setups.

The characterization of microstructure was investigated in the first section of Chapter 3 by using scanning electron microscope (SEM), transmission electron microscope (TEM) and atomic force microscope (AFM). The electrical and thermal properties of materials were explored in the second and third section of Chapter 3, respectively. The results in this chapter have partly been published in the journal of *Advanced Materials*<sup>[36]</sup>, and submitted to journal *NPG Asia Materials* for publication.

The purpose of this work is to develop ductile high-strength nanocomposite material. Therefore, Chapter 4 focuses on studying plastic deformation of npg-based composites with different polymers that occurs in both compression and tension, and compares it to its parent material, namely, npg and polymer. Structure-property relations of npg-polymer composites and native npg will be further researched for full understanding of the issue. In the first section, microhardness and compression tests will be performed on npg, polymer and their composites to investigate the plastic deformation behavior in compression. The compressive behavior of composites is compared to that of their constituents phase to illustrate the important distinction.

The polished cross-sections of deformed sample investigated by SEM were used to study the deformation mode during plastic flow of nanoporous metals under uniaxial load. A part of results obtained in this chapter have been published in the journal of Ref. [36]. The second section of this chapter demonstrates a design of a protocol which makes it possible for cm-sized samples to be tested in tension. The specimen can be prepared by a custom-made apparatus to eliminate the effects of subtle testing misalignment of the test specimen in the testing machine. The plastic deformation in tension of nanoporous gold-polymer composites is explored by tensile test, three- and four-point bending tests. The results in this chapter have partly been submitted to journal *NPG Asia Materials* for publication.

In Chapter 5, the elastic deformation behavior of materials was explored with three methods: instrumented indentation test, load-unload compression test and dynamic mechanical analysis (DMA). The elastic modulus of npg and composites will be discussed in the section of this Chapter.

This dissertation ends with Chapter 6, which summarizes the whole work and gives an outlook on future research possibilities.

## **1.3 State of the art**

### **1.3.1 Dealloying**

The process of dealloying is a selective dissolution process of a precursor alloy, which until recently has usually been researched in the context of corrosion<sup>[37]</sup>. An important element of the process is selective dissolution of the precursor alloy's constituents, usually the less noble ones. It is conducted through chemical or electrochemical means, where the more noble atoms are not leached off and aggregate instead. What is left behind are porous skeletons of other elements.

Dealloying has a long and rich history. Selective dissolution is an ancient technology: early Andean metal smiths used this technique, which was known as depletion gilding, to enhance the surfaces of their artifacts<sup>[38]</sup>. By this technique, a non-gold element near the surface of a less expensive alloy such as Au-Cu or Au-Ag was selectively dissolved by chemicals to create a surface of pure Au, and during this process copper or silver was removed from the surface of alloys.

An important condition for the process to be completed is that one of the constituents of the starting alloy should be less noble than the other. It makes it easier to selectively remove one of the constituents from the alloy in potentiostatic conditions or when it is exposed to an oxidizing medium. From the point of view of electrochemistry, it is crucial that the standard oxidizing potential of the less noble component is much lower than in case of the nobler component.



### 1.3.1.1 The overview mechanism of dealloying

A complete model of selective dissolution has been developed over the years. Four possible mechanisms may account for the formation of nanoporous structures by dealloying: ionisation–redeposition, volume diffusion, surface diffusion and the percolation model.

(1) Ionisation-redeposition mechanism proposed by Brahm<sup>[39]</sup>: in the initial stage the two elements in the alloy ionize or are dissolved in the electrolyte. Next, redeposition of the more noble metal onto the surface occurs. Nevertheless, studies show that only one of the metal atoms is preferentially dissolved. It is important to note that most often in experimental conditions of nanoporosity formation the dealloying potential is much lower than the minimal potential necessary for dissolution of the more noble element to take place.

(2) Volume diffusion mechanism suggested by Pickering *et al.*<sup>[40, 41]</sup>: from all atoms, only the less noble ones can be dissolved from the alloy and get into the solution. Volume diffusion enables the transfer of both metals through the solid phase. There are voices stating that this factor is especially significant for the movement of species in the solid state. It has been assumed that less noble atoms at kink sites, as presented in Figure 1, are dissolved and then ionized. Given the driving force is high enough, atoms found at non-kink sites, as shown in Figure 1, can find their way into the solution in the form of a divalent ion. The less noble atoms on a complete lattice layer can be disposed of and reach the solution, which results in surface vacancies. Such surface vacancies can be filled either by lone absorbed atoms coming from the surface or by atoms on the lattice layer below the surface. The vacancies filled in the latter way will lead to atom's movement from the bulk alloy to the surface. Consequently, the less noble atoms transferred to the surface causes additional vacancies in the alloy's interior. An excess vacancy concentration near the surface increase progressively, which will improve diffusion of less noble atoms from the bulk alloy to the surface. At the same time, more noble atoms are diffused backwards due to the gradient of the ration between these two atoms.

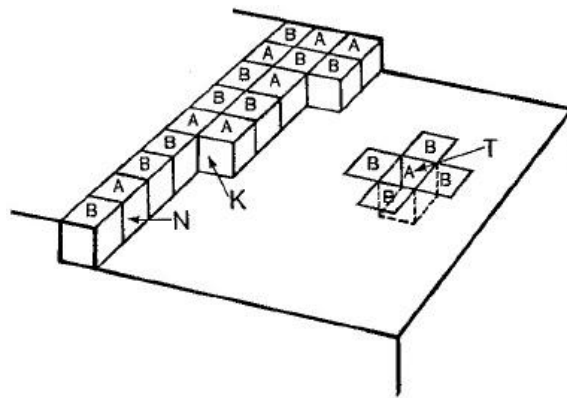


Figure 1:<sup>[42]</sup> Schematic representation on an atomic scale of the surface of an alloy composed of dissolvable A atoms and noble B atoms. K is a kink site on a surface step, N is a non-kink site on a step, and T is a terrace site. A atoms at the kink sites will dissolve first, while those at the N and T positions will be removed when greater activation energy can be obtained.

(3) Surface diffusion mechanism, which was proposed by Forty *et al.*<sup>[43, 44]</sup> by studying Au–Ag and Au-Cu systems, suggested that the dissolution of the more active element causes system disorder and subsequently, the system is reordered through aggregation of the remaining more noble element caused by surface diffusion in order to reduce the surface energy.

(4) The percolation model was proposed by Sieradzki *et al.*<sup>[45, 46]</sup> for the selective dissolution process, which expands upon the surface diffusion model. Following this model, the continuous connected cluster of less noble elements makes dissolution possible, as well as the electrolyte that can not only dispose of less noble atoms on the surface and those located interior, but it can also enter the bulk solid. The electrolyte penetration is also supported by coarsening of the initial clusters producing a skeletal structure labeled a backbone which contains most of the cluster, which precedes the nanoporous structure developed in the process of dealloying. The coarsening was achieved by surface diffusion of the more noble atoms.

### **1.3.1.2 Parting limit**

Importantly, dealloying exhibits a sharp compositional threshold or parting limit which is expressed in the form of critical atom percentages of the less noble component. Only above this value can the more active component be removed from the alloy through electrochemical dissolution that takes part in an oxidizing environment. Early theories of the parting limit appealed to geometrical thresholds in a compositionally ordered alloy lattice.<sup>[47]</sup> Recently, the connectivity of reactive atoms in the more usual case of a disordered alloy has been the focus of attention.<sup>[45]</sup> This concept is still used in noble metal technology to separate noble from base metals. For instance, an alloy of 55 at.% gold and 45 at.% silver does not dealloy, but if the atomic fraction of silver in the alloy reaches the value exceeding 60 percent, then the gold can be separated almost completely in an oxidizing environment such as nitric acid or by application of a suitable potential.<sup>[48]</sup> In principle, dealloying does not take place if the percentage of reactive element is below the parting limit, irrespective of the potential.

### **1.3.1.3 $E_c$ – Critical potential for dealloying**

In some cases, an alloy does not undergo selective dissolution below a certain potential known as critical potential, even if it meets the requirements for dealloying (like parting limit). An available definition describes it as the onset of selective dissolution which is characterized by an abrupt increase in current density with increasing potential, which represents the transition from alloy passivity to porosity formation. Sieradzki *et al.*<sup>[49]</sup> determine the critical potential by physics of the processes, which showed that for most systems  $E_c$  is determined by a balance between selective dissolution, which roughens the surface and surface diffusion which smoothens the surface. Below the critical potential, surface diffusion of the nobler component is more predominant and with time it enriches the surface preventing a bulk dealloying. When the critical potential is exceeded, bulk dealloying controls the surface diffusion and porosity

evolution can be observed. The value of  $E_c$  is determined by the concentration of the more noble component and grows together with the increase in its concentration.

### 1.3.1.4 Volume shrinkage during dealloying

Parida *et al.* found that the macroscopic volume is reduced up to 30% during electrochemical dealloying of Au-Ag alloys.<sup>[18]</sup> They suggested that the volume contraction of npg was correlated with the dealloying rate, which was dependent on the applied dealloying potentials  $E_D$  as well as transferred charge  $Q$ . More shrinkage and faster dealloying was seen with higher potentials, and relative length change  $\Delta l/l_0$  varies in proportion to the amount of the transferred charge  $Q$ . Figure 2 shows the correlations between length change and  $Q$ , as well as characteristic time,  $t_{1/2}$  which represents the time at which half of the total dealloying charge was transferred. From Figure 2(c), the extent of shrinkage is larger and dealloying is faster (with lesser  $t_{1/2}$ ) at higher  $E_D$ . It has been suggested that plastic deformation is an important factor that should be considered in order to rationalize the increasing defect density that occurs at higher  $E_D$ , simultaneously with the growing shrinkage. A particularly important factor for such dimensional changes was the surface stress-induced compressive yielding, despite the fact that it was initially expected to take place only in ligaments characterized by several nanometers or less. However, such small diameter ligament exists in a transient state, which is subject to rapid coarsening. Parida *et al.*<sup>[18]</sup> assumed that the volume shrinkage occurring during dealloying is caused by plastic deformation. This process requires a mechanism for the nucleation of dislocation, due to the fact that large numbers of dislocations have to be present to account for the high level of shrinkage. It was suggested that the dislocation was caused by the collapse of pores that had to be small enough.

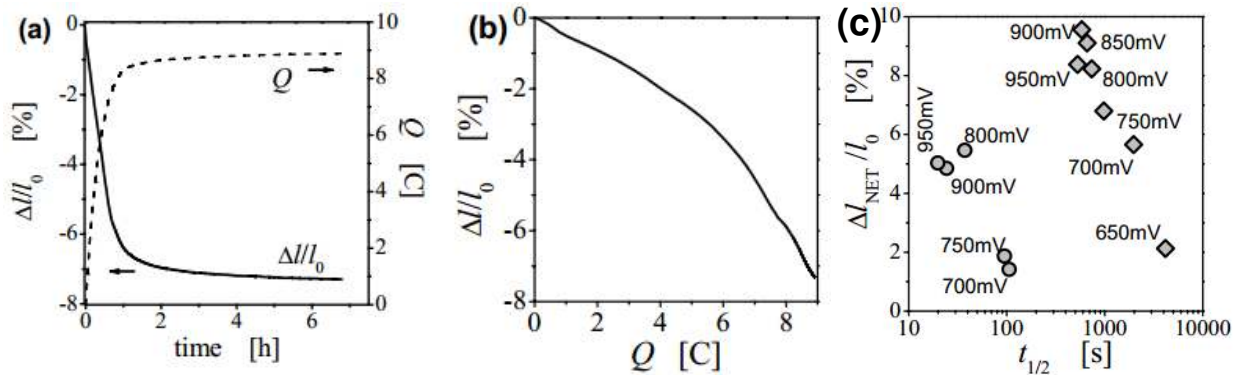


Figure 2<sup>[18]</sup>: (a) In situ dilatometry traces for a 0.9 mm<sup>3</sup> bulk Ag<sub>75</sub>Au<sub>25</sub> cube showing the time evolution of relative length change  $\Delta l = l_0$  and of transferred charge  $Q$  at dealloying potential 850 mV versus Ag/AgCl. (b) The relative length change  $\Delta l/l_0$  versus transferred charge  $Q$  for the data in (a). (c) Net length change after completion of dealloying versus the half-time of dealloying for bulk (♦) and 11 carat leaf (●) samples. Data points are labeled according to applied potential.

### 1.3.1.5 Crack formation during dealloying

The dealloying process for nanoporous gold typically leads to a high density of cracks<sup>[3, 18, 35, 50, 51]</sup>, which impair the mechanical performance. The underlying cracking mechanism as well as ways to prevent it have to be completely understood since the mechanical integrity is a crucial condition in nanoporous metals' application. Volume shrinkage is a factor behind the crack formation, and it usually occurs during dealloying. It is brought about by tensile stress observed in freshly formed porous materials found the dealloying front.<sup>[18, 19]</sup>

Due to the volume contraction that typically accompanies dealloying and the macroscopically brittle nature of nanoporous metals, crack formation seemed inevitable during processing.<sup>[3, 51, 52]</sup> However, some researchers found that the cracking can be reduced or even eliminated by controlling the dealloying potential or temperature, and also by reducing residual stresses in the master alloy through recovery anneals.<sup>[19, 50]</sup>

Parida et al.<sup>[18]</sup> found that accelerated corrosion observed at higher potentials resulted in the largest change in volume. Samples dealloyed under these conditions were found to have many lattice defects and were subject to extensive macroscopic cracking. In comparison, the starting alloys and samples dealloyed at a slower rate with a lower potential are found to have significantly fewer defects. This suggests that the defects and subsequent macroscopic cracking caused by aggressive dealloying procedures are generated from the dealloying.<sup>[17]</sup>

Sun et al.<sup>[53]</sup> have successfully synthesized the crack-free thin film npg, and Senior and Newman<sup>[50]</sup> have fabricated relatively thin (100  $\mu\text{m}$ ) bulk npg foil by optimizing the Au content of the alloy, controlling the applied potential and/or increasing the temperature of the electrolyte. It should be noted that the crack-free 100  $\mu\text{m}$  thick npg was not completely dealloyed through the thickness; only a thin surface layer, several microns thick, was dealloyed<sup>[50]</sup>.

Sun and Balk<sup>[54]</sup> produced bulk nanoporous gold with ligament width of 14 nm by using a simple two-step dealloying method. No volume change is found and only a few narrow intergranular cracks at isolated locations on the sample surface were observed. They proposed that the galvanostatic dealloying method used in their work appears superior to potentiostatic methods for fabricating millimeter-scale samples.

Zhong et al.<sup>[55]</sup> discussed the role of the parameters (i) lattice parameter change, (ii) dealloying potential and rate, and (iii) thermo-mechanical treatment of the master alloys in their work. They found that changing the starting alloy from  $\text{Au}_{25}\text{Ag}_{75}$  to  $\text{Au}_{25}\text{Cu}_{75}$  at applied dealloying potential of 1.1 V versus Ag/AgCl can completely suppress the formation of the crack and successfully yielded ligament size below 10 nm.

## 1.3.2 Introduction of nanoporous gold

Nanoporous gold (npg) is a relatively new material and has attracted more and more interest in recent years due to its interesting properties and structural features. The material represents a

homogeneous interconnected network of ligament with dimension that can be controlled down to well below 10 nm.<sup>[8-10]</sup> Investigations by transmission electron microscopy, focused ion beam imaging, and electron backscatter diffraction have established that nanoporous metals prepared in this way are polycrystalline with a grain size of 10-100  $\mu\text{m}$ .<sup>[18, 19]</sup> Each micron-sized grain is nanoporous, so that neighboring ligaments share the same crystal lattice. In other words, the local structure in volumes of, say, 1  $\mu\text{m}^3$ , is that of a single crystal containing a contiguous nanoscale pore network.

### 1.3.2.1 Methods to tune the microstructure of npg

The ligament sizes of npg can be alternated from a few nanometers to micrometer. There are at least four methods to change the ligament size: changing dealloying conditions such as dealloying potential<sup>[56]</sup>, types of electrolyte, and dealloying time; cathodic cyclic voltammograms (CV) scans; acid coarsening after dealloying<sup>[57]</sup>; and thermal post-treatment where nanoporous specimens are exposed to elevated temperatures after dealloying.<sup>[5, 21, 32, 58, 59]</sup> Considering that gold cannot be oxidized in the open air, it is easy to tune the ligament and pore dimension from nanometer to micrometer in length scale by applying a simple furnace anneal that has different annealing time and temperature. The basis of this principle is Ostwald ripening theory<sup>[21, 35, 45, 52]</sup> which states that it is diffusion that drives the formation of larger and more thermodynamically stable structures. In the case of nanoporous gold, the coarsening of ligaments and pores is driven by the reduction of surface energy, which involves surface diffusion of gold atoms in order to form nanoporous structures with minimal surface energy.

### 1.3.2.2 Mechanical properties of npg

Recently, the mechanical properties of nanoporous gold have attracted a lot of research attention. Several studies have been devoted to deformation mechanisms and ligament strength of npg<sup>[3, 20, 21, 60-63]</sup>.

#### 1) Yield strength

The Gibson-Ashby scaling equation may be used for estimating the local yield stress based on the effective materials behavior of npg.<sup>[3, 20]</sup> According to the standard model of foam plasticity developed by Gibson-Ashby<sup>[64]</sup>, the relationship between yield strength and the relative density  $\varphi = (\rho_{\text{np}}/\rho_{\text{s}})$  of an open-cell isotropic foam can be calculated as follows:

$$\sigma_{\text{y}} = C_1 \sigma_{\text{s}} (\rho_{\text{np}}/\rho_{\text{s}})^n \quad (1)$$

where  $\sigma_{\text{s}}$  is the yield strength of the solid materials,  $\rho_{\text{s}}$  and  $\rho_{\text{np}}$  are the density of the solid materials and the porous counterpart,  $C_1$  and  $n$  stand for empirical constants.

Biener *et al.*<sup>[20]</sup> performed depth-sensing nanoindentation measurements on bulk nanoporous gold with a relative density of 42%. The hardness of npg was calculated according to the ratio of the applied load and the projected indentation area as a function of the contact depth. They found

that the mean hardness ( $H$ ) of npg was 145 ( $\pm 11$ ) MPa. In the case of porous metals, the yield strength  $\sigma$  is simply equal to the hardness,  $\sigma = H$ ,<sup>[64, 65]</sup> due to densification. Since the surrounding material does not constrain the deformation under the indenter, the indentation tests plays a role of a uniaxial compression test. Following this correlation, the yield strength of npg is assumed to equal 145 MPa. Applying the literature value<sup>[66]</sup> for the Au macroscopic strength is  $\sigma = 200$  MPa. Equation 1 shows that the yield strength of nanoporous gold characterized by 42% relative density will equal 16.3 MPa. Therefore, as demonstrated in the Biener's research, the yield strength of npg measured by nanoindentation (145 MPa) exceeds approximately 10 times the value estimated by scaling laws of open-cell foams proposed by Gibson-Ashby. Jin *et al.*<sup>[19]</sup> also measured the hardness value of npg by a series of microhardness tests. However, they found the hardness of npg is approximately three times the yield stress ( $\sigma_Y = HV/3$ ), as in a conventional, massive material.

Volkert *et al.*<sup>[3]</sup> investigated mechanical properties of npg by running uniaxial compression tests using a flat punch in a nanoindenter on npg micron-sized columns made by a focused ion beam (FIB). The stress-strain curves of npg columns show an elastic region and a yield point at around 100 MPa, followed by increasing flow stress with strain. All columns with different diameters display a high yield strength of 100 MPa for 15 nm diameter npg ligaments. Solving equation 1 for the ligament strength yields:

$$\sigma_Y^L = C_1^{-1} \sigma_Y (\rho_{np}/\rho_s)^{-n}, \quad (2)$$

where  $\sigma_Y^L$  acts as the strength of the solid part. In the case of Volkert's study above, the measured yield stress of 100 MPa of npg with the relative density of 36% predict a yield stress of 1.5 GPa for the 15 nm diameter ligaments. This value is 10-100 times larger than typical yield stresses for bulk Au. The value of 1.5 GPa measured here is even close to the expected theoretical shear strength of Au<sup>[67]</sup>.

Jin *et al.*<sup>[19]</sup> performed compression tests on macroscopic, crack-free nanoporous gold samples. The yield strength,  $\sigma_Y$ , was found to be 7.5 and 27 MPa for samples with  $L = 55$  and 15 nm, respectively. Both values are considerably lower than typical values for npg micropillars that amount to 70-90 MPa at a similar solid fraction ( $v_s = 0.3$ )<sup>[11]</sup>. Following the equation 2, the estimated  $\sigma_Y^L$  equals 190 and 625 MPa for samples while their  $L = 55$  and 15 nm respectively. However, this value is inconsistent with the last nanoindentation<sup>[11, 20, 21, 61, 68]</sup> and micropillar compression<sup>[3, 11]</sup> tests on npg, where  $\sigma_Y^L$  was compatible with the master curve of individual submicron columns. What is more,  $\sigma_Y^L$  in this case is also much lower than the value found in individual, free-standing gold columns or similar size wire (for example 3.5 GPa for 100 nm Au nanowire)<sup>[69-74]</sup> and likewise for arrays of parallel nanowires<sup>[75]</sup>.

## 2) Elastic modulus

Analogous to the yield strength, the relationship of elastic modulus for the open-cell materials to the relative density and the properties of the fully dense material has been derived analytically.<sup>[64]</sup> The scaling relation for elastic modulus is:

$$E = C E_s (\rho_{np} / \rho_s)^n \quad (3)$$

where  $\rho_{np} / \rho_s$  stands for the relative density of the porous material and  $E$  and  $E_s$  are the elastic modulus of porous and solid gold, respectively.<sup>[64]</sup>  $C$  and  $n$  are empirical constants. The proportionality constant  $C$  and the density exponent  $n$  describe the cell geometry. Experimental data indicate that a wide range of open-cell macroporous foam materials can be adequately described by  $C = 1$  and  $n = 2$ .<sup>[64]</sup> The elastic modulus of dense Au is 78 GPa.<sup>[76]</sup>

Biener *et al.*<sup>[20]</sup> measured the Young's modulus of npg with a relative density of 42% and a ligament length scale of around 100 nm. A Young's modulus of 11.1 ( $\pm 0.9$ ) GPa was obtained from the analysis of the load-displacement curves. Volkert *et al.*<sup>[3]</sup> performed multiple load-unload cycles during uniaxial compression tests on npg columns. Young's modulus of npg was determined from the unloading segments as a function of plastic strain. It increased from 7 GPa to 12 GPa when the plastic strain changes from 2% to 36%. These values agree closely to the  $E$  of npg between 7 and 11 GPa which is estimated according to the scaling law in the same relative density and using  $E_s$  of Au,  $E_s = 57-85$  GPa<sup>[2]</sup>, as a reference.

Balk *et al.*<sup>[29]</sup> proposed a testing method that allows both tension and compression tests in small samples. It turned out that the tested elastic modulus of approximately 3 GPa did not differ considerably in tension and compression state, however, it was much smaller than the expected modulus of 7 GPa for npg with the same relative density implied by scaling relation of Gibson-Ashby. It was also lower than moduli values derived from nanoindentation testing<sup>[3]</sup>.

### 3) Mechanical test methods

There are three widely used mechanical test techniques to explore the mechanical properties of npg. 1) Nanoindentation has been used by many researchers<sup>[20, 33, 59, 61]</sup> to explore the compressive strength and Young's modulus using the methods. 2) Compression test: there are two compression testing methods for npg. One is actually a variant of indentation. Volkert *et al.*<sup>[3]</sup> performed compression on npg columns which were made by focused ion beam (FIB) using a nanoindenter with a diamond punch having a flat end. The other are conventional compression tests carried out on macroscopic nanoporous gold samples<sup>[19]</sup>, which requires crack-free samples. 3) Three-point bending. Li *et al.*<sup>[5]</sup> obtained load-displacement curves to fracture of npg with various ligament sizes by using the traditional three-point bending method.

### 4) Size effects on mechanical properties – “smaller is stronger”

It has been well established that the size of ligaments or pores of npg can be tuned. So it is of interest to know how the mechanical behavior changes with variations in ligament size. Biener *et al.*<sup>[11]</sup> explored the ligament size effects on mechanical properties of npg by using a combination of nanoindentation, column microcompression and molecular dynamics simulations. They found that the hardness and yield strength increased dramatically with decreasing ligament size. The strength of nanoporous gold can be compared to that of bulk Au, even though it is a highly porous material and its ligaments' yield strength is nearly the same as the theoretical yield strength of gold.<sup>[11]</sup>

Furthermore, Hodge *et al.*<sup>[21]</sup> studied comprehensively the relationship between yield strength,  $\sigma$ , relative density and ligament sizes,  $L$ , for nanoporous gold foams. They performed depth-sensing nanoindentation tests on nanoporous gold foams ranging from 20 to 42% relative density with ligament sizes ranging from 10 to 900 nm and modified the Gibson and Ashby yield strength equation for open-cell macro-cellular foams in order to incorporate ligament size effects. They found that the yield strength of ligaments ( $\sigma_{yc}$ ) followed a Hall-Petch type law in the relationship to  $L^{-1/2}$ :

$$\sigma_{yc} = (\sigma_0 + k_{Au} L^{-1/2}) \quad (4)$$

where  $\sigma_0$  is related to the bulk material yield strength, and  $k_{Au}$  is a material constant that describes the yield strength size-dependence in the regime of 10 nm to 1  $\mu$ m. ( $k$  has the unit MPa·nm<sup>1/2</sup>).  $L$  stands for the ligament size. Specifically, they obtained a relationship for  $\sigma_{yc} = 200 + 9821 L^{-1/2}$  between the yield strength of ligaments in MPa and ligament size in nm. Combining equation 1 and 4, they obtained a modified scaling equation:

$$\sigma^* = C_s (\sigma_0 + k_{Au} L^{-1/2}) (\rho_{np}/\rho_s)^{3/2} \quad (5)$$

where  $C_s$  is a fitting coefficient,  $\sigma_0$  is the bulk material yield strength,  $k$  is the Hall-Petch type coefficient for the theoretical yield strength of Au in the regime (10 nm to 1  $\mu$ m), and  $L$  stands for the ligament size. For macroporous foams ( $L \gg 500$  nm),  $kL^{-1/2}$  becomes negligible and equation 5 yields equation 1. This study demonstrates that at the nanoscale, foam strength is governed by ligament size, in addition to relative density.

Hakamada *et al.*<sup>[33]</sup> investigated the size effect of ligament size on the yield strength of npg also by Nanoindentation tests. They annealed npg to achieve various ligament sizes. They found that the yield strength of the Au ligaments increases with decreasing ligament size according to:

$$\sigma_{ys} = K d_1^m \quad (6)$$

where  $d_1$  is the ligament size,  $K$  is a constant and  $m$  is the ligament size dependence, which was determined to be approximately -0.20 in the present npg in their work. They found the yield stresses of cell ligament Au solids were much higher than that of bulk polycrystalline Au. Grain refinement strengthening and dimensional constraint theory for a micron-sized metal were inappropriate for explaining the high strength of npg. They concluded that size and surface effects, which are the same as those in metallic nanowires, possibly play important roles as strengthening mechanisms in npg.

Mathur *et al.*<sup>[77]</sup> explored the Young's modulus of freestanding, large-grained, and stress-free npg thin films with a controlled porosity variation between 3 and 40 nm by using a buckling-based method. The results showed that the effective Young's modulus of npg dramatically raised with decreasing ligament size, especially if the ligament size is below 10 nm.

The mechanical behavior of npg material obeys scaling equations derived for foams with macroscopic porosity, and the local strength of the ligaments follows the same<sup>[3, 11, 20, 21]</sup> or similar<sup>[19, 22]</sup> trends as individual nanowires, of which the strength increases with decreasing dimension<sup>[1-3]</sup>. The observation of theoretical strength in defect-free crystals, such as whiskers,



irrespective of their size exemplifies that the trend of “smaller is stronger” is related to the defect structure.<sup>[13-15]</sup> The interaction of dislocations with the surface is another important factor, as is evidenced by in-situ observation of large recoverable flow-stress changes during interfacial charging or electrosorption.<sup>[16]</sup> The material, and in particular nanoporous gold, has thus been studied as a model system for size-effects on the plasticity of nanostructures.

##### 5) Failure behavior of npg – “macroscopic brittleness and microscopic ductility”

Nanoporous gold can be deformed to large plastic strain in compression, in contrast to many other nanomaterials that fail after few percent of deformation.<sup>[12]</sup> The deformability of npg may be understood from the macroscopic constitutive behavior. Similar to nanopillars or nanowires,<sup>[4]</sup> the individual nanoscale ligaments are expected to show little work hardening. Yet, the absence of transverse plastic strain in the macroscopic nanoporous metal implies that compression under uniaxial stress is completely carried by densification of the network of ligaments.<sup>[19]</sup> By virtue of the scaling<sup>[64]</sup> of the flow stress,  $\sigma_F$ , with solid volume fraction,  $\phi$ , as  $\sigma_F \propto \phi^{3/2}$ , the densification causes work hardening at the macroscopic scale, promoting stable and uniform<sup>[19]</sup> plastic flow in compression. Yet, the same argument also points to the central deficiency of nanoporous metals as structural materials: Plastic flow under tensile loading reduces the density, resulting in work softening and, hence, in shear instability and brittle failure<sup>[16, 29]</sup>.

Li *et al.*<sup>[5]</sup> studied the failure behavior of nanoporous gold with various ligament sizes by analyzing the load-displacement curves ( $P$ - $\delta$ ) of npg in three-point bending test. It was observed that npg showed a sample-size-driven ductile-brittle transition that is transformed from brittle to ductile as the ligament or pore size grows with respect to the sample dimensions. They evaluated scaled fracture displacement  $\Delta_f$  and strains  $e_f$  versus the scaled sample size  $\acute{L}$ , where  $\Delta_f = \delta_f / (A/N)^{0.5}$ ,  $\acute{L} = L / (A/N)^{0.5}$  and  $e_f = \Delta_f / \acute{L}$ .  $L$  is the width of the beam in  $\mu\text{m}$ ,  $(A/N)^{0.5}$  is the average cell size in  $\mu\text{m}$  and  $\delta_f$  is the load point displacement at fracture. They found the fracture strains  $e_f$  at small  $\acute{L}$  are large, which indicates ductile behavior, whereas the fracture strains at large  $\acute{L}$  are small, which is more typical of brittle behavior. The conclusion was that npg is characterized by a ductile-brittle transition that was governed by the microstructure length scale. What is more, they observed that this transition is most probably universal if one considers the exact nature of the constitutive behavior of the individual ligaments in the random structure, especially when analyzed in relation to the overall sample geometry. The whole conclusion was derived from the assumption that when the sample size is big enough, no microscopic ductile-brittle transition occurs in the failure mechanism.

Biener *et al.*<sup>[35]</sup> reported the failure behavior of npg with ligaments on nanometer length scale by observing fractured npg samples which were manually bent to fracture using a three-point bending setup with electron microscopy. Even though there are no signs of plastic deformation before failure, which would normally point to brittle npg fracture macroscopically, in fact, npg is from the microscopic point of view a very ductile material. It was observed, when indentation induced cracking, that some of the ligaments found near the cracks were strained by as much as 200%. Furthermore, cell-size effect on the microscopic failure mechanism was also studied by

observing the deformation of annealed npg. Elongation of the cell structure and slip bands in ligaments were detected after deformation of the annealed samples. It was proposed that the annealing process allowed sufficient distribution to eliminate defects that would serve as crack nucleation sites. They concluded that the macroscopic brittleness of npg arises from the network structure rather than reflecting a microscopic brittleness.

### 1.3.3 Traditional composite materials

Majority of traditional composite materials contain discrete fibres or particles that are dispersed within a binding matrix phase.<sup>[78]</sup>

#### 1.3.3.1 Fibre reinforced polymer composites

FRP, the fibre reinforced polymer is a composite material that contains polymer matrix implanted with fibres of high strength, for instance glass, aramid or carbon.<sup>[79]</sup> It may seem like a modern idea to have pseudo one-dimensional fillers perform the role of a reinforcing agent, but, in fact, there are example of applying this method that date back until about 4000 BC, for example, using a straw in order to strengthen mud brick construction. In more recent times, fibres made from materials such as alumina, glass, boron, silicon carbide and especially carbon have been used as fillers in composites. Composite materials reinforced with synthetic fibres, particularly with glass, are widely used in industrial applications. On the other hand, many questions appeared asking whether the use of glass fibres reinforced polymer composites is safe from the environmental point of view, it has been even implied that it may pose a substantial threat to human health. The reasons behind this controversy are high energy consumption and the pollutants emission that occurs in the fabrication process.<sup>[80]</sup> In recent years, the use of nature fibres to replace glass fibres as an alternative reinforcement in polymer composites has gained the attention of many researches and scientists due to their advantages over man-made glass and carbon fibres, such as low cost, low density, comparable specific tensile properties, non-abrasive to the equipments, non-irritation to the skin, reduced energy consumption, less health risk, renewability, recycle ability and bio-degradability.<sup>[81]</sup> The most important natural fibres are flax, hemp, jute, sisal, kenaf, coir, kapok, banana, henequen and many others.<sup>[82]</sup>

The chemical, mechanical, and physical properties of natural fibres have distinct properties; depending upon the cellulosic content of the fibres which varies from fibre to fibre. Ku *et al.*<sup>[83]</sup> summarized three factors that can influence the performance of natural fibre reinforced composites. The mechanical properties of composites are influenced mainly by the adhesion between matrix and fibres. Chemical and physical modification methods were incorporated to improve the adhesion between fibre and matrix resulting in the enhancement of mechanical properties of the composites.<sup>[81]</sup> In addition to the hydrophilic nature of fibre, it is important to note the significant influence of fibre content on the properties of natural fibre reinforced composite. To put it shortly, high fibre content equals high performance of the composites. It is often observed that the increase in fibre loading leads to an increase in tensile properties.<sup>[84]</sup> The

choice of processing parameters to apply is another significant factor that considerably changes the properties and interfacial characteristics of the composites. That is why it is crucial to wisely select the most fitting processing methods and parameters in order to receive the optimum composite products.

The nature fibre composite materials are suitably applicable for aerospace, leisure, construction, sport, packaging and automotive industries, especially for the last mentioned application.<sup>[81, 83, 85]</sup> Nevertheless, despite excellent in-plane specific mechanical properties of fibre reinforced polymer composites, majority of standard FRP laminates are affected by poor out-of-plane performance. In addition to this, natural fibre reinforced polymer composites are incompatible with hydrophilic natural fibres, which can result in certain unwanted properties of the composites.<sup>[83]</sup>

### ***1.3.3.2 Carbon nanotube reinforced polymer composites***

Since carbon nanotubes (CNTs) were discovered by Iijima in 1991<sup>[86]</sup>, they have generated huge activity in most areas of science and engineering due to their special physical and chemical properties. What is particular about them are their extraordinary mechanical, electronic and thermal properties combined. Thanks to their special properties they are regarded as perfect for advanced filler materials in composites. Recent results have been reported on the use of nanotubes in polymer<sup>[87]</sup>, metallic<sup>[88]</sup> or ceramic<sup>[89]</sup> matrix composite.

In recent years, the development of nanoparticle reinforced composites has become an attractive new subject in materials science. Nanoparticles in general are regarded as high potential fillers to improve the mechanical properties of polymers.<sup>[90]</sup> Moreover, depending on the type of filler used, nanoparticles can have an effect on thermal and electrical conductivity of the final nanocomposite. Carbon black and carbon nanotubes due to their unique properties, are interesting candidates.

Especially, CNTs have shown a high potential to improve the strength and stiffness of polymers as well as add multi-functionality (such as electrical conductivity) to polymer based composites systems.<sup>[91-93]</sup> Kilbride *et al.*<sup>[94]</sup> have envisaged taking advantage of their conductivity and high aspect ratio to produce conductive plastics with exceedingly low percolation thresholds. In another area, it is thought that their massive thermal conductivity can be exploited to make thermally conductive composites.<sup>[95, 96]</sup> However, the most promising area of composites research probably involves the mechanical enhancement of plastics using carbon nanotubes as reinforcing fillers.<sup>[97]</sup>

Coleman *et al.*<sup>[97]</sup> summarized four main system requirements for effective reinforcement. These are large aspect ratio, good dispersion, alignment and interfacial stress transfer. A more or less linear increase of modulus with aspect ratio is predicted by the rule of mixtures<sup>[98]</sup> and the Halpin-Tsai equations models<sup>[99]</sup>. Dispersion is thought to be the major prerequisite. For the efficient load transfer to the nanotube network to occur, it is necessary for CNTs to be dispersed in a uniform way to the level of isolated nanotubes that are coated with polymer. A more

uniform stress distribution can also minimize the presence of stress concentration centers that are thought to be connected with the uniform dispersion. Decrease in strength and modulus usually goes along with poor dispersion<sup>[100]</sup> and it can be observed in a number of system when the nanotube loading level exceeds the point where aggregation starts. Alignment is a less crucial issue. The difference between random orientation and perfect alignment is a factor of five in composite modulus.<sup>[97]</sup> While alignment is crucial to increase strength and stiffness, it is not always an advantage. It cannot be denied that aligned composite possess anisotropic mechanical properties and there may be a need to avoid them in bulk samples. On the other hand, in fibres there are no drawbacks of alignment and it is a good method to increase reinforcement. When a critical value of the interfacial shear stress is present, rupture of the matrix near the interface of the matrix-nanotube bond will occur and lead to debonding.<sup>[97]</sup> The shear stress value can be defined as the interfacial shear strength and it controls the maximum stress transfer to the nanotube. It is a significant parameter for a fibre-reinforced composite and it has been a subject of many experiments. First of all, one has to make sure whether any stress reaches the nanotubes. It is assumed that the most significant prerequisite here is that external stress that is applied to the composite is completely and efficiently moved to the nanotubes which provides them with a disproportionate share of the load.<sup>[97]</sup>

CNTs attract more and more interest due to their excellent properties that make them a good choice when selecting fillers for polymer composite systems. On the other hand, using it as filler particles is also connected with aggravated challenges. To illustrate the problem, the surface area of a nanotube is a suitable interface for stress transfer, however, it also induces strong attractive forces between the CNTs which results in excessive agglomeration behavior. In polymer matrix, the dispersion of CNTs is not homogenous which can negatively affect composites' mechanical properties. In addition to this, the second problem is the debonding between the CNTs and the matrix polymer that affects the development of CNT reinforced polymer composites.

### ***1.3.3.3 A comparison of fibres and carbon nanotube***

Coleman *et al.*<sup>[97]</sup> reviewed the difference of properties between fibres and carbon nanotubes. Fibres made from materials such as alumina, glass, boron, silicon carbide and especially carbon have dimensions on the meso-scale with diameters of tens of microns and lengths in the order of millimeters. Their mechanical properties are impressive with carbon fibres typically displaying stiffness and strength in the ranges 230-725 GPa and 1.5-4.8 GPa, respectively<sup>[98]</sup>. In recent years carbon nanofibres have been grown from the vapor phase with diameters in the order of 100 nm and lengths between 20 and 100  $\mu\text{m}$ . These small dimensions mean they have much higher surface area per unit mass than conventional carbon fibres allowing much greater interaction with composite matrices. They also tend to have impressive mechanical properties with Young's modulus in the range 100-1000 GPa and strengths between 2.5 and 3.5 GPa<sup>[101]</sup>.

In comparison to carbon fibres, the ultimate mechanical filler material must be carbon nanotubes. Nanotubes can have diameters ranging from 1 to 100 nm and lengths of up to millimetres.<sup>[102]</sup> Their densities can be as low as  $\sim 1.3 \text{ g/cm}^3$  and their Young's moduli are superior to all carbon

fibres with values greater than 1 TPa<sup>[103]</sup>. However, their strength is what really sets them apart. The highest measured strength for a carbon nanotube was 63 GPa<sup>[104]</sup>. This is an order of magnitude stronger than high strength carbon fibres. Even the weakest type of carbon nanotubes have strengths of several GPa<sup>[105]</sup>.

### **1.3.3.4 Polymer matrix**

In natural fibre-polymer composites, the polymer matrix holds the fibres together to provide a shape and transfer the load to the fibres by adhesion and/or friction, and also provides rigidity and shape to the structural member, protects fibres from chemical and corrosion, influence the performance behaviors such as impact and ductility.<sup>[106]</sup> Generally, polymer can be classified into two classes, thermoplastics and thermosettings. The commonly used thermoplastic polymer matrix is polypropylene (PP) and several synthetic thermoplastics such as polyethylene (PE), polystyrene (PS). The primary thermoset resins used are phenolic, epoxy and polyester resins.<sup>[81]</sup>

Yan *et al.*<sup>[106]</sup> summarized the advantages and disadvantages of different polymer matrices. Thermoplastics have many advantages over thermoset polymers in composites fabrication such as low processing cost, design flexibility, and ease of moulding complex parts. However, the development of thermoplastic natural-fibre composites is restricted by the processing temperature, which should be below 230 °C to avoid degradation of nature-fibres. Although thermoplastic materials currently dominate as matrices for nature-fibres, nowadays thermosets attract more and more attentions. This is because thermoset polymers outperform thermoplastics in some areas, including mechanical properties, chemical resistance, thermal stability, and overall durability. In addition, thermosets allow for more flexibility in structural fibre configurations and can be processed at room temperature or at temperatures comfortably within the safe range for natural fibres. Among thermosets, epoxy is the most common one in many studies<sup>[107-113]</sup>.

## **1.3.4 Interpenetrating phase composites**

### **1.3.4.1 Introduction**

As opposed to standard composite that are built of discrete fibres or particles dispersed within a binding matrix phase,<sup>[78]</sup> there is no isolated phase in an interpenetrating phase composite (IPC). Such composites are characterized by a completely interconnected and contiguous network formed by each phase. Their growing popularity is observed as an important class of composites materials where the components are in a co-continuous state and are described as a combination of two different materials classes, such as polymer or metal, those are combined on a macroscopic level. As said before, a completely interconnected network is formed within fully dense composite form during each individual solid phase. In case any of the constituent phases is missing, a self-supporting, open-celled foam is created by the remaining phases. Interpenetrating composites, with their unique properties, can cause synergetic effects, for instance, higher values

of relevant properties may be observed as well as additional and new properties may appear. Therefore, recently more and more researches focus on investigate novel composites such as interpenetrating phase composite that can have different structure and novel exciting mechanical behaviors.

Wegner and Gibson<sup>[78]</sup> carried out a finite element study to investigate two-phase interpenetrating phase composites. The thermal-mechanical properties of IPCs were compared with those of non-interpenetrating phase composites. Their results indicate that the elastic, strength and thermal expansion properties of IPCs are enhanced when compared with those of non-IPCs. The best enhancements results can be yielded in cases when the phases' properties differ considerably to such an extent that theoretical bounds on the effective properties of composites are separated. On the other hand, any differences will be significantly lowered if phase properties have the same order of magnitude and the significance of the volume fraction increases.

This leads to the conclusion that the most advantageous property of an IPC lies in its ability to achieve several desirable properties at once by combining a number of continuous phases, each of which possesses one of the properties desired. Clearly, the main purpose of the studies on new composite materials has been to obtain combination of material properties that are not present in single phase materials. From this point of view, IPCs are particularly beneficial since they provide a number of possibilities for property combinations, especially when an isotropic is needed.

IPCs are becoming an important class of materials by virtue of an increasing number of processing techniques to create them. There are several types of IPCs, such as ceramic-metal IPCs, that were developed with new processing techniques by Günther *et al.*<sup>[114, 115]</sup>. Another example are IPCs produced by Lanxide Corporation with directed metal oxidation (DIMOXtm)<sup>[116]</sup>, the so-called 'C4' materials that are achieved a result of sacrificial oxide displacement reactions<sup>[117-120]</sup>. Other examples are materials obtained as a result of spontaneous infiltration<sup>[121, 122]</sup>, squeeze casting<sup>[123]</sup>, or gas pressure assisted infiltration<sup>[124-128]</sup>. The 'cemented steels' of the 1940s<sup>[129, 130]</sup> are early examples of IPCs. Finally, the recently developed three-dimensional printing process can be used to produce materials with an interpenetrating microstructure<sup>[131]</sup>.

It can happen that metallic nanoporous materials are regarded as a type of interpenetrating composite. They are characterized by air phase in the pores that is treated as the second phases.<sup>[30]</sup> However, they are not as attractive from the point of view of research on the second phase effect since the contribution of gas phase in the pores to the general properties of the foam is relatively low. Nevertheless, the second phase effect on metal foams' properties can be considerable if the gas phase is substituted. Jin and Weissmueller<sup>[16]</sup> presented a hybrid material concept that developed a hybrid nanostructure that was composed of porous metal which is interpenetrated by an electrolyte as the second component. The material's properties, such as strength and ductility, can be adjusted to altering requirements in service through polarizing the internal interface via an applied electric potential. It offers a user new options, for instance, it is

possible to choose a soft and ductile state for the purpose of processing and a high-strength condition to serve as a structural material. Still, if the damping phase filling the pores is stiffer or damper in order to substitute the gas phase, the second phases' direct effect can also play an important role.

#### **1.3.4.2 Bounds on elastic modulus**

Although considerable work has been conducted on modeling the effective elastic properties of composites, no known work targets IPCs specially. Only two works identified by Wegner and Gibson<sup>[78]</sup> have some application to IPCs. Perhaps the most well-known bounds on effective elastic moduli are those of Hashin and Shtrikman<sup>[132]</sup>, derived on the basis of variational principles in the linear theory of elasticity and formulated in terms of the so-called polarization tensor. Their bounds have been applied to all multiphase composites of arbitrary phase geometry, including IPCs, which may be regarded as quasi-isotropic and quasi-homogeneous when a sufficiently large volume of the composite is considered (i.e., specimen dimensions are much larger than dimensions of the microstructural features). They are the most restrictive bounds possible without incorporating information concerning microstructural geometry. Figure 3 illustrates that they are most useful when the modular ratio - the ratio of the larger to the smaller phase modulus - is not too large.<sup>[78]</sup>

Improved bounds may be obtained by incorporating information concerning microstructural geometry into theoretical calculations. This may be done in terms of the so-called  $n$ -point probability  $S_n$  functions<sup>[133-135]</sup>, which give the probability of  $n$  randomly located points all being located within the same phase of a composite. A review article by Torquato<sup>[136]</sup> summarizes how these probability functions have been used to derive certain  $n$ -point parameters which, in turn, are used to calculate improved bounds for various effective composite properties. Since only the lowest order probability functions are available in practice, it is still only possible to calculate bounds on the properties, rather than exact expressions. However, bounds incorporating third- or fourth-order functions can be much improved relative to those which account only for volume fraction (i.e., first-order functions). Figure 3 shows the bounds derived using three-point parameters for two theoretical microstructures<sup>[78, 136]</sup> which may, under certain conditions, represent IPCs. Higher order probability functions specific to IPCs are not available, so that, in their present form, the  $n$ -point parameter bounds are also rather limited in their usefulness for application to interpenetrating microstructures.

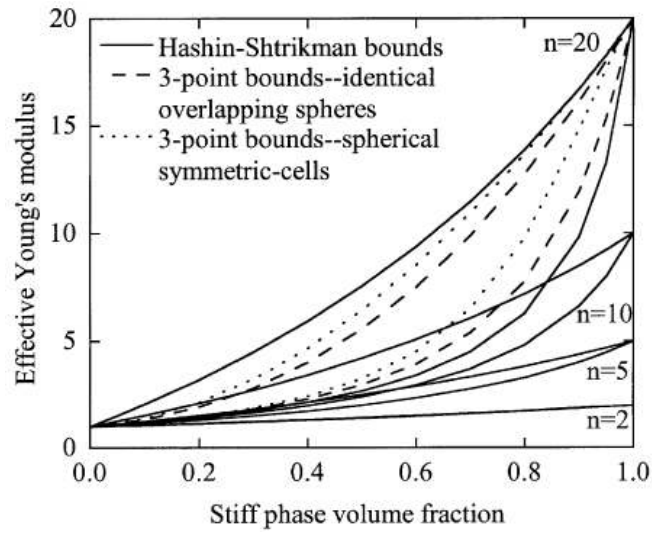


Figure 3<sup>[78]</sup>: Theoretical bounds on the effective Young's modulus of a composite for various ratios of phase moduli (modular ratio,  $n = E_{stiff}/E_{flexible}$ , where  $E$  is Young's modulus).



# Chapter 2.

## Experimental procedures

### 2.1 Nanoporous gold

#### 2.1.1 Bulk alloy preparation

In this work, nanoporous gold samples were prepared in bulk (mm-sized) form. Bulk npg samples were dealloyed from Au<sub>25</sub>Ag<sub>75</sub> alloys. The Au<sub>25</sub>Ag<sub>75</sub> alloy ingot was prepared by arc-melting Au (ChemPur, 99.995%) and Ag (ChemPur, 99.99%). The ingots were sealed in quartz glass and homogenized by annealing for 100 h at 850 °C. Then, ingots were formed into a 1 mm diameter wire, followed by cutting into 1.7 mm (for compression test samples) or 20 mm (for tension tests) in length by a diamond wire cutting machine. Some of ingots were rolled to 1 mm thick sheets and polished on one side down to 1 μm diamond finish, from which cuboid master alloy samples were obtained by cutting. Then samples were annealed in vacuum during 3h at 650°C for recovery.

#### 2.1.2 Dealloying and tuning the ligament size

For the purpose of dealloying, a three-electrode electrochemical cell with a luggin capillary controlled by a potentiostat (VoltaLab) was used. Before the start of the experiment all of the cells in this work were immersed in a standard Piranha solution (5 volume parts concentrated H<sub>2</sub>SO<sub>4</sub> + 1 part 30% H<sub>2</sub>O<sub>2</sub>) for 24 hours and then rinsed thoroughly with ultrapure 18.2 MΩ cm grade water (Arium 611, Sartorius) to remove adsorbed ions. The alloy samples were dealloyed

at an applied potential of 750mV versus a Ag/AgCl homemade-reference electrode(RE) in one molar perchloric acid (1 M HClO<sub>4</sub>), by means of a coiled silver wire as a counter electrode (CE). When the current fell to below 10 μA, a potential hold at 850 mV for 4 hours led to a completion of dealloying. The dealloying time depended on the sample size and the amount of samples.

The Ag/AgCl homemade-reference electrode was prepared by oxidizing a silver wire (0.5 mm diameter, Ag 99.99%, ChemPur) at 0.9 V for 60 seconds in one molar hydrochloric acid (1M HCl), using another Ag wire with larger surface area served as both reference and counter electrode. The 1 M HClO<sub>4</sub> electrolyte was prepared from ultrapure 18.2 MΩ cm grade water, and 70% concentrated perchloric acid solution of superpure grade from Merck with the corresponding volume shares.

Finally, the nanoporous gold samples were immersed in water to remove residual internal electrolyte. Then the samples were thoroughly dried in vacuum for 3 days. As-prepared nanoporous gold samples were annealed at 300 °C in a furnace (MR 170E, Heraeus, Germany) in air for different times to adjust the length scale of the ligaments.

## **2.2 Nanoporous gold-polymer composites**

### **2.2.1 Introduction of vacuum impregnation method**

Vacuum impregnation is a very useful technique used to fill polymer such as epoxy resin in pores or voids of specimens. The most effective technique is to pour the polymer under vacuum and/or apply pressure before or during the curing cycle. For porous specimens, the resin can aid in supporting structure features. Filling voids can be difficult depending on their size, with the smaller voids being much more difficult to impregnate than larger voids.<sup>[137]</sup> The main reason behind it is the compressibility and air volume within the void. By applying a vacuum to the specimen and pouring while under vacuum the total pressure of this air can be reduced significantly. Subsequent curing at an increased pressures will force (or push) the resin into the voids. It has to be added that it is important to restrict the vacuum time as much as possible on the resin and specimen to minimize the degassing of the resin.

The degree of impregnation depends on many characteristics: amount of closed vs. interconnected porosity; overall sample density; size of inherent porosity; overall thickness of coating.<sup>[138]</sup> Those factors that influence the vacuum impregnation method also affect the integrity of specimens: type of infiltrated polymer materials; viscosity of infiltrated materials; procedure to impregnate (vacuum vs. pressure); vacuum impregnation, pressure impregnation procedure (pressure gas media); curing time.<sup>[138]</sup>

## 2.2.2 Introduction of polymer

According to the Washburn law,<sup>[139, 140]</sup> the time-scale for imbibitions scales with the inverse square-root of the viscosity. In the interest of facile impregnation, a low viscosity polymer should be chosen. Still, polymer's mechanical properties are connected with the molecular weight. The polymer's viscosity and functionality increases along with the molecular weight. An important aspect to consider before selecting the impregnation polymer material is the balance between viscosity and polymer's mechanical characteristics. For this reason, reaction polymers,<sup>[141]</sup> such as epoxies and urethanes,<sup>[142, 143]</sup> are considered as impregnation materials. This kind of polymer can be obtained from industrial sources. In most cases they begin their life in liquid form which contains small molecular weight of resin and hardener, facilitating infiltration procedures. Curing is then carried out to convert liquid to the final solid state of thermosetting polymer. They have very high load bearing capability; excellent environmental and chemical resistance. What is more, generally formulated to be 100% solids (no solvent emissions to deal with); and come in a range of cure times and properties. Structural adhesives cure in an irreversible process which helps provide excellent temperature and solvent resistance. They do not need access to air to dry, moisture is not needed either and that is why they have unlimited depth of cure.

In this work, “two-part formulations” epoxies and polyurethanes were chosen. Two-part epoxies and urethanes require a certain amount of time for the cure to start after the two parts are mixed and the surfaces to be bonded are mated, which allows infiltration at low viscosity until some level of cure has occurred.

### 2.2.2.1 Epoxy resin

Epoxy resins offer very high mechanical performance (with respect to tensile strength and modulus, and compressive strength) and solvent resistance to environmental degradation. They tend to have higher vibration/impact resistance (thus, higher fatigue resistance) and higher performance in an extreme temperature. Therefore, epoxy resin has come to dominate the aerospace industry and it is widely used in custom-built aircrafts. There are a lot of researchers used epoxy as matrix in order to fabric materials found in composite construction.<sup>[90, 144-146]</sup>

Aufray and Roche<sup>[147]</sup> stated that epoxies offer good bonds to gold. Organo-metallic complex formation is achieved when epoxy-amine liquid combination is applied onto metallic substrates, such as Au as a result of which concomitant amine chemisorption and metallic surface dissolution take place. Epoxies come in the widest range of properties and can have the best overall properties on metals.

In this study two epoxies were used for impregnation. One is bisphenol A epoxy and the other is bisphenol F epoxy. Bisphenol A is a reaction product of phenol and acetone.<sup>[148]</sup> As presented in reference<sup>[149]</sup>, bisphenol A is reacted with epichlorohydrin to form diglycidylether bisphenol A resin (DGEBA). Adding more bisphenol A to liquid DGEBA forms semi-solid or solid resins

with increased molecular weight of the formulation. The higher the molecular weight is, the higher the viscosity and functionality of the resin are. Functionality is the number of functional side groups available for reaction with curing agents. More reactive sites per molecule lead to more three-dimensional crosslink density. Increasing functionality thus increases strength and chemical resistance. Purchased bisphenol A epoxy resin system composes of DGEBA and amine hardener. Purchased bisphenol F epoxy resin system are composed by two components: diglycidylether of bisphenol F (DGEBF) and diammine.<sup>[150]</sup> Bisphenol F is produced by phenol reacted with formaldehyde. The resultant phenolic chemical does not have the two methyl groups that are present between the ring structures in bisphenol A resins.<sup>[149]</sup> Because of the missing methyl groups, the viscosity of bisphenol F resins is lower than that of bisphenol A resins. Lower viscosity means fewer additives and diluents are needed to enhance application properties. Additives and diluents diminish the crosslink density, which in turn lowers chemical resistance of any epoxy system. Additionally, bisphenol F resins also have less of a tendency to crystallize at low temperatures compared to bisphenol A resins.

Balachandran *et al.*<sup>[150]</sup> compared the DGEBF resin system with the DGEBA resin system. They found that the DGEBF system has lower viscosity, glass transition temperature and mechanical strength at room temperature. The DGEBF resin system shows high flexibility at room temperature, but the Young's modulus is lower than that of the DGEBA resin system.

### **2.2.2.2 Polyurethane**

Polyurethane(PU) formulations cover an extremely wide range of stiffness, hardness, and density.<sup>[143]</sup> They are quite flexible and ductile, but have lower strength in general. They have been used since 1950s, and now become the most popular polymer material, widely used in the production of "sponge" products. Polyurethane polymers are formed by reacting an isocyanate with a polyol.<sup>[151]</sup> Both the isocyanates and polyols used to make polyurethanes contain on average two or more functional groups per molecule. They generally are lower priced than other types of structural adhesives.

### **2.2.3 Polymers used**

For the purpose of this research, three kinds of polymer are used:

- (1) A small chain-length Bisphenol F epoxy resin (BER 20, Buehler, Germany, number average molecular weight  $\leq 700$  g/mol) and amine hardener (BEH 20, Buehler, Germany). The epoxy resin and hardener (Buehler, Germany) were mixed at a weight ratio of 4:1 and warmed in water bath at 55 °C for further reducing the viscosity and providing deeper penetration into the porous sample;
- (2) Bisphenol A epoxy resin (RIMR 135, Hexion Specialty Chemicals, Netherlands, number average molecular weight  $\leq 700$  g/mol) and hardener (RIMH 137, Hexion Specialty Chemicals, Netherlands) were mixed using a resin-to-hardener ratio of 10:3 at ambient temperature;

(3) Polyurethane (PU) resin (Baytec CC 9803, BaySystems, Germany) and hardner (Desmodur 9804, BaySystems, Germany) were mixed with mass ratio of 1:1 at room temperature.

For brevity, the three polymers were designated as RIM, BE, and PU, respectively. In the interest of facile impregnation, low viscosity was achieved by selecting a small resin chain length and for BE epoxy by heating the resin/hardener mixture.

The choice of polymers was motivated as follows: Bisphenol-F was used due to its low chain length, promoting low viscosity and good imbibition. RIM is an epoxy that is commercially used for fibre-reinforced composites, for instance in the aircraft industry. One of its distinguishing features is its high strength. The higher performance of composites can be achieved by using epoxy resin. The PU used in this work has lower strength but considerably higher ductility than the resins. It is expected that the composites using flexible PU will have better ductility. All three composites use amine groups in the linker molecules. Amine groups are known to form covalent bonds with gold,<sup>[147]</sup> promoting low polymer-gold interface energy and, therefore, good imbibition of the polymer by the porous gold as well as good adhesion during mechanical deformation.

#### 2.2.4 Vacuum impregnation procedure

The nanoporous gold-polymer composites were prepared using a commercial vacuum impregnation unit (CitoVaca, Struers, Germany). Moulds containing dry nanoporous gold samples were put into the vacuum vessel of the impregnation unit and were evacuated for 30 minutes. Then molds were filled in situ with the liquid polymer/hardener mixture and the liquid then was pushed into the pores by venting the vessel to air. As the infiltration process was complete, molds containing epoxy-hardener mixture were placed in the oven at 60 °C for 20 minutes in order to speed up the curing rate. They were subsequently cured for minimum 24 hours at room temperature. On the other hand, the molds filled with polyurethane mixture were cured directly at room temperature for minimum 4 hours.

According to the data sheet of RIM epoxy from Hexion Company, curing at room temperature for 24h only results in partly cured RIM epoxy. The partly cured sample should be placed in an oven at 60 °C for 16 hours for full cure. All RIM-based samples of this work were post-cured at 60 °C for 2 hours. The only exception is samples for the DMA experiment, which will be post-cured for 24 hours at 60 °C.

Surplus polymer was removed by either (a) cutting the sample from the cured polymer or (b) lifting the sample out of the mixture before curing and then blotted with a soft tissue. Vacuum impregnation with a mixture of resin and hardener, followed by curing, yielded the composite samples.

## **2.3 Measurement procedure and setups**

### **2.3.1 Scanning electron microscope and energy-dispersive x-ray analysis**

A scanning electron microscope (LEO 1530 Gemini Column FESEM) operated at 15 kV equipped with an energy-dispersive x-ray (EDX) analyser with 10 mm<sup>2</sup> SDD detector, namely an Oxford INCA system was used for chemical analysis.

For the purpose of obtaining fracture surface, it was necessary to cleave the npg samples by bending with tweezers. In case of composite samples, the fracture surface could be obtained by means of cutting with a knife since it was not possible to bend them.

Fresh smooth cross-sectional surfaces for the characterization of the specimens were prepared by cutting, grinding and polishing steps. A diamond saw (Well Diamond Wire Saws, Inc., Germany) was used for exposing a fresh surface, which needs to be smoothed by grinding and polishing. Abrasive papers of 1000 grit (silicon carbide paper) were used wet for rapid removal of material by grinding. Finer grade of abrasive paper 4000 (silicon carbide paper) was used to remove damage produced by the earlier grit. After the 4000 grit grind, the surface was smooth enough to be polished with diamond pastes. Polishing removes the damage imparted by the sawing and grinding operations. A sequence of successively finer particle size diamond polishing suspensions (Struers, Germany) ranging from 3 µm to 0.25 µm, together with water based with lubricating agent (DP-Lubricant Red, Struers, Germany) and a low-relief polishing cloth were used for polishing. The smoothed surface was obtained using an automated polisher during subsequent polishing stages of 3 µm, 1 µm, and 0.25 µm suspensions for respectively 5, 3 and 3 minutes.

### **2.3.2 Dilatometry**

The dilatometer (Linseis, L75V) was used to record the sample dimension change during annealing. A cuboids' sample was mounted between support and pushrod, and measured at 300°C for 2 min and 30 min. The length change of the sample was transmitted to an inductive displacement sensor via the pushrod loaded by a fixed contact pressure of 20 mN.

### **2.3.3 Transmission electron microscope**

A transmission electron microscope (Jeol FX 2000) was performed on RIM-npg composite samples with ligament size of 50 nm. The sample was prepared by microtome cutting.

### 2.3.4 Atomic force microscopy

The atomic force microscopy (AFM) was performed by using the system XE-100E AFM (Park Systems Corp.). A 910M-NCHR cantilever with a 42 N/m force constant and about 330 kHz resonance frequency was used. The AFM image was a topography image made in so-called NC-AFM mode (non-contact mode), also known as "tapping mode".

### 2.3.5 Dynamic mechanical analysis

Dynamic mechanical analysis (DMA) can be described in simple words as a dynamic method that helps to characterize a material's viscoelasticity. It can be conducted by applying a sinusoidal force or displacement and then examining the response this input provokes. It is possible to measure viscoelasticity judging from the phase response.

The stress applied as a function of time at a given frequency,  $\omega$ , is given as

$$\sigma(t) = \sigma_0 \sin(\omega t + \delta), \quad (7)$$

where  $\sigma_0$  is the maximum stress applied and  $\delta$  is the phase angle.<sup>[152]</sup> The strain, which lags by the phase angle,  $\delta$ , is given by:

$$\varepsilon(t) = \varepsilon_0 \sin(\omega t), \quad (8)$$

where  $\varepsilon_0$  is the maximum strain amplitude.<sup>[152]</sup> Through Hooke's law, the input and the response are related by the dynamic modulus,  $E^*(\omega)$ ,

$$\sigma(t) = E^*(\omega) \varepsilon(t). \quad (9)$$

The dynamic (or complex) modulus has in phase and out of phase components, and is given by

$$E^*(\omega) = E'(\omega) + iE''(\omega), \quad (10)$$

where the in phase, or real, portion is  $E' = (\sigma_0/\varepsilon_0) \cos\delta$ , and the out of phase, or imaginary, portion is  $E'' = (\sigma_0/\varepsilon_0) \sin\delta$ .<sup>[152]</sup> The storage modulus,  $E'$ , is proportional to the energy stored per cycle and characterizes the elastic behavior of the material<sup>[153]</sup>. The loss modulus,  $E''$ , is proportional to the lost or dissipated energy per cycle and characterizes the viscous behavior of the material.<sup>[153]</sup> The ratio of energy dissipated to energy stored is the tangent of the phase angle,  $\delta$ , called tan delta, which is given by:<sup>[152]</sup>

$$\tan \delta = E''(\omega) / E'(\omega). \quad (11)$$

In this work dynamic mechanical analysis measurements were carried out with a DMA/SDTA861e (METTLER TOLEDO, Germany) equipped with a 40 N load cell using a compression clamp for the specimens, what the diameter was around 1 mm and the height was around 1.7 mm. The static load was 20 N, and the dynamic load was 4 N for the RIM-npg composite samples with  $L$  of 20 nm, 50 nm and 150 nm. The static load was 16 N and the dynamic load was 2.5 N for the pure RIM epoxy samples. For some of the specimen, they were

post-cured at 60 °C for 24 hours after the initial room temperature curing. The applied oscillation frequency was 10 Hz. All of the measurements for composite and epoxy were performed in temperature sweep mode from -30 °C to 140 °C with a constant heating rate of 3 K·min<sup>-1</sup>. The static load was 1.5 N and the dynamic load was 0.5 N for the bulk npg samples. All of the measurements for npg samples were performed in frequency sweep mode from 0.1 Hz to 250 Hz. For the purpose of DMA data analysis, it is necessary to plot storage modulus or tan delta against temperature.

The method of determining the  $T_g$  in the DMA can be a manner for disagreement, as at least five ways are in current use.<sup>[152]</sup> Depending on the industry standards or background of the operator, the peak or onset of the tan delta curve, the onset of the  $E'$  drop, or the onset or peak of the  $E''$  curve may be used.<sup>[152]</sup> The values obtained from these methods can differ up to 25 °C from each other on the same run.<sup>[152]</sup> Therefore, it is necessary to specify exactly the method of determining the  $T_g$  in practice. In this work, the glass transition temperature,  $T_g$ , is determined from the peak of the tan delta curve.

### 2.3.6 Resistance meter

The electric conductivity of composite samples was measured by a four-probe approach using a resistance meter (Resistomat®, Burster). An appropriate aspect ratio was obtained with samples 4.2×1.8×0.6 mm<sup>3</sup> in dimension, contacted at the end surfaces.

### 2.3.7 Vickers microhardness test

Vickers hardness (HV) was performed by a microhardness tester (UHL VMHT MOT). Loads of 10 g for the composites and 1 g for npg were chosen so as to obtain comparable indentation depths. The indentation times are 30 s. The two diagonals of the residual indentation marks were directly measured by optical microscopy and converted into hardness. For the indentation tests, one side of the samples was finely polished with 0.25 μm diamond suspension and the polished procedure was the same as for preparing the smooth cross-sectional surface for the characterization. At least 20 indents were made on each of several samples for each measurement. As an estimated error the variance for the set of indents was quoted. The Vickers hardness is calculated by following equation:

$$HV = \frac{1854.4 \times F}{d^2} \quad (12)$$

where the load  $F$  is in grams-force (1gf = 9.8 × 10<sup>-3</sup> N) and  $d$  is the diagonal of the residual indentation marks.



### 2.3.8 Instrumented indentation test

Instrumented indentation tests were conducted using the Fisherscope® H100 instrumented microhardness system (Helmut Fischer GmbH, Germany) with a Vickers indenter. Before the start of the measurement, a larger load on the sample is obtained by means of a hollow cylinder ring surrounding the indent, which is supposed to fix the specimen during measurement. That is why the measurement is not possible for npg since it is not strong enough and could be crushed by the cylinder.

The tests were performed on composite and polymer samples at constant displacement rate 0.5 mm/min with maximum indentation force of 49 mN. For each indentation, the applied load value is plotted with respect to the corresponding position of the indenter. The resulting load-displacement curves are used to calculate quantitative hardness and elastic modulus values.

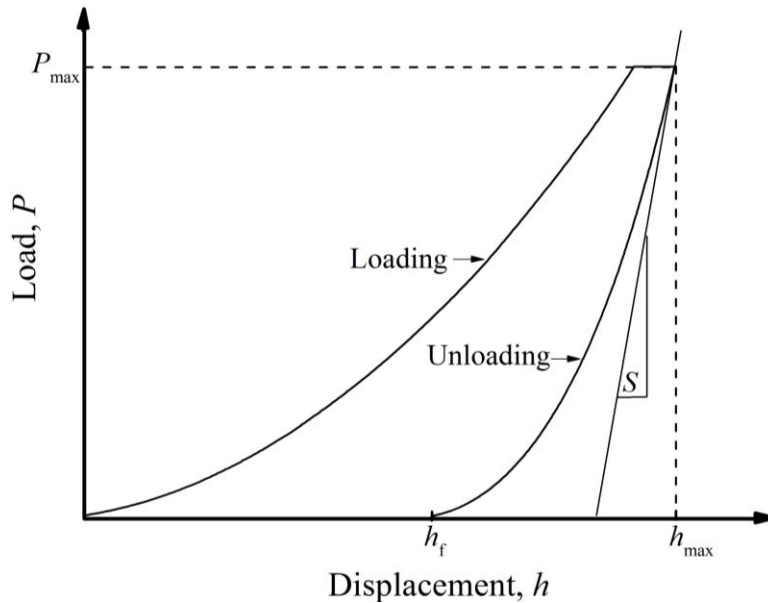


Figure 4: A typical load-displacement curve with a load-unload cycle with the maximum indenter displacement,  $h_{max}$ , at peak indentation load,  $P_{max}$ . The initial unloading stiffness,  $S$ , is defined as the initial unloading slope of the load-displacement curve, and  $h_f$  is the final depth.

The mechanical properties, such as elastic modulus and hardness value can be obtained by analyzing obtained load-unload cycle in the indentation load-displacement curve,<sup>[154-156]</sup> and without observing the residual indentation marks. The exact method used to measure the hardness and the elastic modulus is based on the unloading processed using equation 13 and 15, see schematic demonstration in Figure 4. This method was adopted from Oliver and Pharr<sup>[155, 156]</sup>. The hardness value obtained by Olive-Pharr method,  $H_{0-p}$ , is calculated according following equation:<sup>[156]</sup>

$$H_{O-P} = \frac{P_{\max}}{A} = \frac{P_{\max}}{24.5 \times (h_c)^2} \quad (13)$$

where  $P_{\max}$  is the maximum indentation force,  $A$  is the projected contact area and  $h_c$  is the contact depth, which is given by:<sup>[155]</sup>

$$h_c = h_{\max} - h_d = h_{\max} - \varepsilon \frac{P_{\max}}{S} \quad (14)$$

where  $h_{\max}$  and  $h_d$  is the maximum indentation depth and the elastic deflection depth, respectively,  $\varepsilon$  is a geometrical constant (0.75 for a conical indenter) and  $S$  is the initial unloading stiffness, which is defined as the slope of the beginning part of the load-displacement curve during unloading as shown in Figure 4.

The elastic modulus,  $E$ , is measured according to the following equation<sup>[155]</sup>:

$$E = \frac{S\sqrt{\pi}}{2A} = \frac{S\sqrt{\pi H}}{2\sqrt{P_{\max}}} \quad (15)$$

### 2.3.9 Compression test

Compression tests were performed using a Zwick 1484 testing machine, with cylindrical npg and composite samples of initial dimensions of 1 mm diameter of cross-section area and 1.7 mm height loaded by planar anvils. The polymer samples of initial cuboid dimension  $\sim 1 \times 1 \times 1.7$  mm<sup>3</sup> was cut by a diamond wire cutting machine from bulk polymer that were collected from the respective mould after vacuum impregnation procedure. The elongation measured between the load surface by displacement sensor. True stress,  $\sigma$ , and true strain,  $\varepsilon$ , were computed from the elongation by exploiting the findings of constant volume for polymer and composite or constant cross-section for npg, see Ref. [19]. A feedback loop controlled and progressively reduced the crosshead speed so as to maintain constant true strain rate of  $10^{-4} s^{-1}$  while the sample length varied. Work hardening indices,  $n(\varepsilon) = d \ln \sigma / d \ln \varepsilon$ , were estimated by taking derivatives on smoothed graphs of  $\ln \sigma$  versus  $\ln \varepsilon$ . Volume changes associated with the compression were estimated by measuring the sample dimension before and after compression with a toolmaker's microscope (Mitutoyo TM, Germany).

### 2.3.10 Three-point bending test

Three-point bending tests were also performed with the use of a custom-built three point bending mold on pure npg and BE-npg composite with  $L$  of 150 nm using a universal testing machine (Zwick 1484, Hottinger Baldwin Messtechnik, Germany). The dimension of sample is  $\sim 2$  mm  $\times$  1 mm  $\times$  6 mm. The surface of npg sample was carefully polished before dealloying, and the surface of the composite sample was polished after infiltration.

### 2.3.11 Tensile test

In this work, it was a serious challenge to test bulk nanoporous gold or composite material in tension conditions, considering how small and brittle nanoporous gold samples are and the fact that they lack machineability. Therefore, a major objective of this work was to prepare a protocol for tension tests. The various aspects of this design will now be described; for the results see 4.2 below.

For tension test, mm-sized bulk npg samples were dealloyed from  $\text{Au}_{25}\text{Ag}_{75}$  alloy ingots that were formed into a 1 mm diameter wire, followed by cutting into 20 mm in length. The long thin master alloy body was suspended in electrolyte during dealloying by using a custom-built gold container, which used thin gold wire to connect to the working electrode. The polymer samples of initial cuboid dimension  $\sim 1 \times 1 \times 20 \text{ mm}^3$  was cut by a diamond saw from bulk polymer that were collected from the respective mould after vacuum impregnation procedure.

Specimens for tensile testing were prepared as indicated in Figure 5: The cylindrical composite or cuboid polymer samples were glued into Al caps (Figure 5(D)) using a two-component glue<sup>[157]</sup> (UHU plus endfest 300, UHU, Germany). An alignment bench, Figure 5 (A) and (B), assured parallel mounting of the caps. The gauge section was around 12 mm in length. Tensile tests were performed in a testing machine (Zwick 1474, Germany) with a custom-build grip for the Al caps and the elongation measured by sensor clips attached to the gauge section (Figure 5(C)). A feedback loop controlled and progressively reduced the crosshead speed so as to maintain constant true strain rate of  $10^{-5} \text{ s}^{-1}$  while the sample length varied.

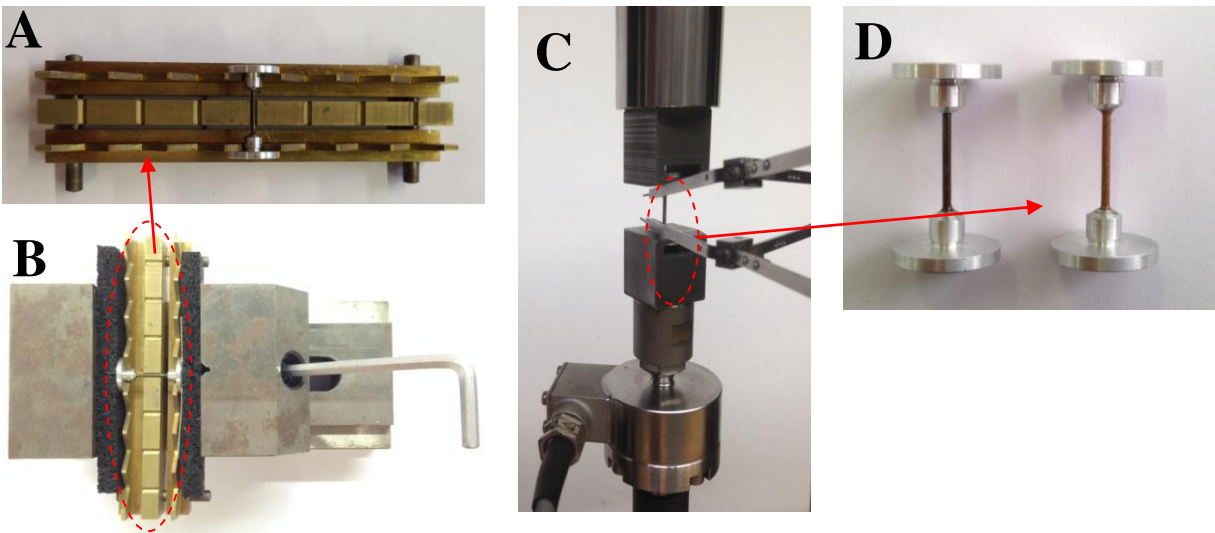


*Figure 5: Photos of a custom-built specimen preparation apparatus: (A) adjustment tool (B) bench vise. (C) A photo of the special custom-built specimen's holder of universal testing machine for aluminum shoulder of samples. (D) A photo of the final tensile testing specimens.*

### 2.3.12 Four-point bending test

Four-point bending tests were performed by using a custom-built machine developed at the Institute of Advanced Ceramics laboratory, Hamburg University of Technology. For this particular bending machine, the scheme of the machine is shown in Figure 6. Figure 7 shows the loading and support conditions. It shows a beam which is bent resting on two supports at distance  $L$ . The inner and outer support roller distances are 10 mm and 20 mm, respectively. The roller diameter is 5mm. The maximum measuring force and displacement of the device is 75 kN and 1500  $\mu\text{m}$ . The dimension of sample is  $\sim 1 \text{ mm} \times 2 \text{ mm} \times 26 \text{ mm}$ . The surface of the sample was carefully polished after infiltration. Force and displacement in the center of the beam were recorded during measurement by load sensor and displacement transducer.

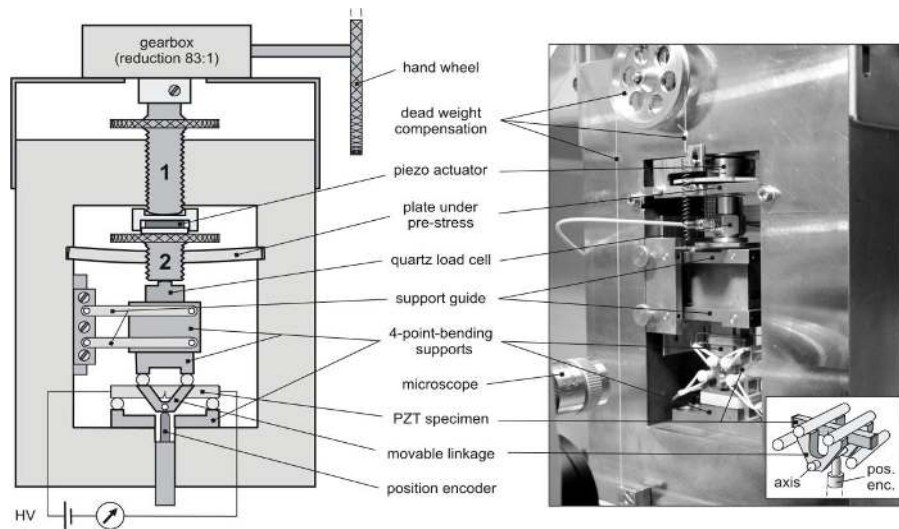


Figure 6: The scheme of custom-build four-point bending machine. Special thanks to Dr. Hans Jelitto from the institute of Advanced Ceramics at Hamburg University of Technology for the sectional drawing.

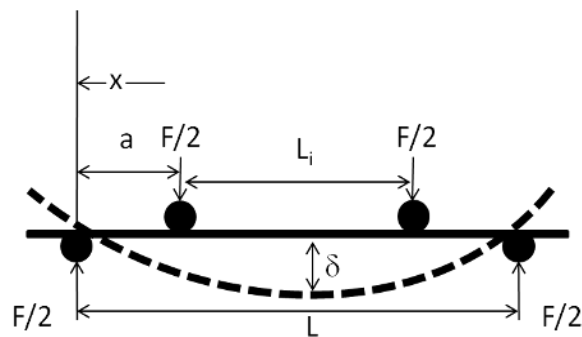


Figure 7: Four-point bending support schematic. The forces  $F/2$  are symmetrically loading the beam at the inner support rollers.  $L$  and  $L_i$  are the outer and inner support roller distances, respectively.  $a$  stands for a distance between the outer and inner support roller.

In order to discuss the result from bending test in relation to other tests on the same material, a stress-strain curve needs to be derived from the load-displacement curve. The measuring principle for stress and strain is based on Bernoulli's bending theory<sup>[158]</sup>. The theory considers bending as the behavior of a structural element under the influence of an external load applied perpendicular to the longitudinal axis of the beam. With the bending theory it is possible to find the current deflection ( $y$ ) in any given distance  $x$  from the outer support up to inner support:

$$y = \frac{Fx}{12EI}(3a(L-a) - x^2) \quad (16)$$

where  $E$  is the elastic modulus and  $I$  is the moment of inertia,  $I = bh^3/12$  here.  $b$  and  $h$  are the width and the height of the sample.  $F$  is the load force and  $L$  is the length of the outer loading span.  $a$  stands for the distance between the outer and inner support rollers. With this equation it is possible to define the displacement,  $\delta$ , in the center of the beam with a specific loading condition:<sup>[159]</sup>

$$\delta = \frac{Fa}{48EI(3L^2 - 4a^2)} \quad (17)$$

The stress,  $\sigma$ , was calculated by<sup>[159]</sup>:

$$\sigma = \frac{3Fa}{bh^2} \quad (18)$$

In elastic bending range, application of Hooke's Law with equation 17 and 18 yields the strain formula:

$$\varepsilon = \frac{12\delta h}{(3L^2 - 4a^2)} \quad (19)$$

### 2.3.13 Load-unload compression test

Load-unload compression tests served to explore the evolution of the stiffness as the compression proceeded. Rather than continuous compression, load-unload cycles were interposed between loading strains. The tests used exactly the same machine and strain rate as the compression test and performed on RIM-npg composite with ligament size of 50 nm, RIM epoxy, and npg with  $L$  of 20 nm, 50 nm and 150 nm. Samples shape and size is the same as those used in compression test. The minimum stress for each unloading step was 2 N. A high hysteresis of load-unload segment was found, especially at higher strain. In such situations, the elastic modulus is determined using a straight line fit of the unloading segment's upper half, as the one presented in Ref. [160]

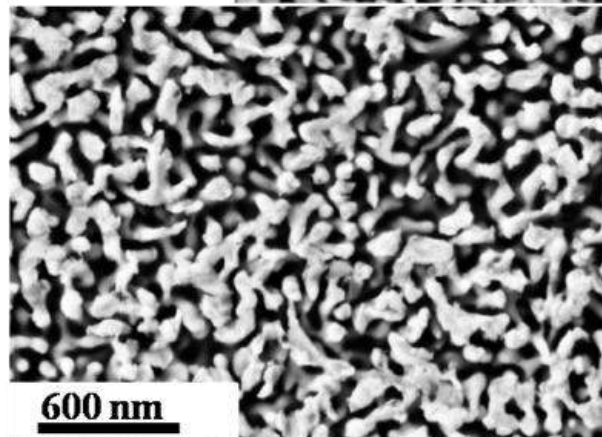
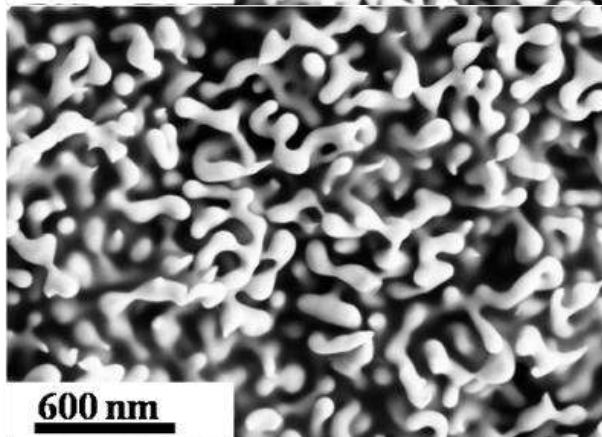
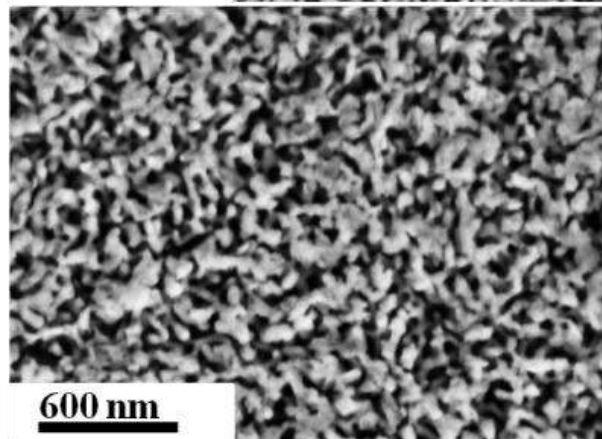
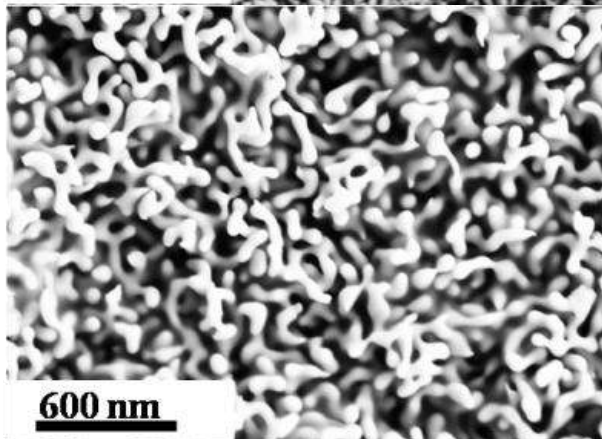
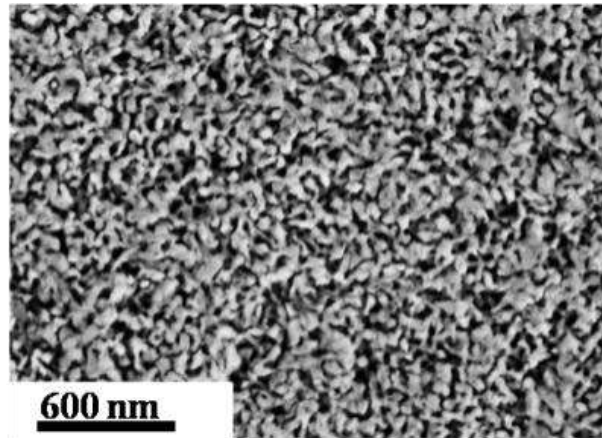
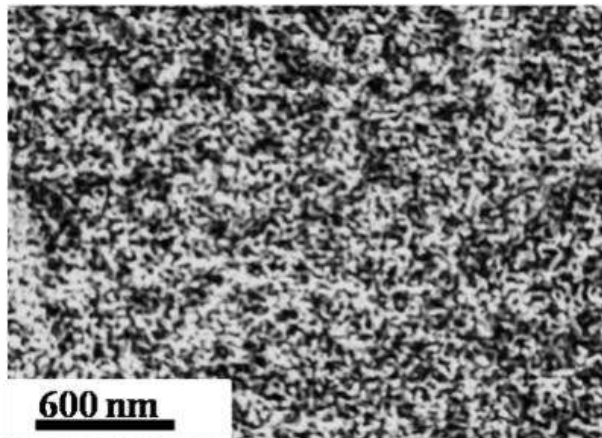
# Chapter 3.

## Characterization

### 3.1 Characterization of microstructure

As described in the experimental procedure section, npg samples with different structure size were prepared by alloy corrosion and subsequent thermal coarsening. Figure 8 shows scanning electron micrographs of cross-sections of RIM-npg composites with ligament sizes,  $L$ , of  $20\pm 5$  nm,  $50\pm 10$  nm,  $80\pm 20$  nm,  $120\pm 30$  nm,  $150\pm 50$  nm and  $250\pm 50$  nm, respectively. Evaluation of SEM images on cutting cross-sectional surface (see in left column of Figure 8) reveals mean diameters of npg ligament of around 20 nm in the as-prepared material. Samples with  $L$  of around 50, 80, 120, 150 and 250 nm were prepared by annealing at 300 °C in air for 2, 5, 10, 30 minutes and 3 hours, respectively.

The solid volume fraction,  $\varphi$ , was estimated based on the amount of Ag removed and on the macroscopic volume contraction. EDX reveals  $\leq 2$  at.-% Ag in the porous metal, while in-situ dilatometer puts the relative volume shrinkage during dealloying at  $\leq 2$  %.<sup>[16]</sup> This implies  $\varphi = 0.27\pm 0.01$  for the as-prepared porous metal. Dilatometry during the coarsening anneals shows volume shrinkages of  $< 3\%$  and  $\sim 15\%$  for 2 and 30 min anneals, respectively. This implies solid fractions of 0.27-0.30 and 0.42 for the samples with  $L$  of 50 nm and 150 nm, respectively.





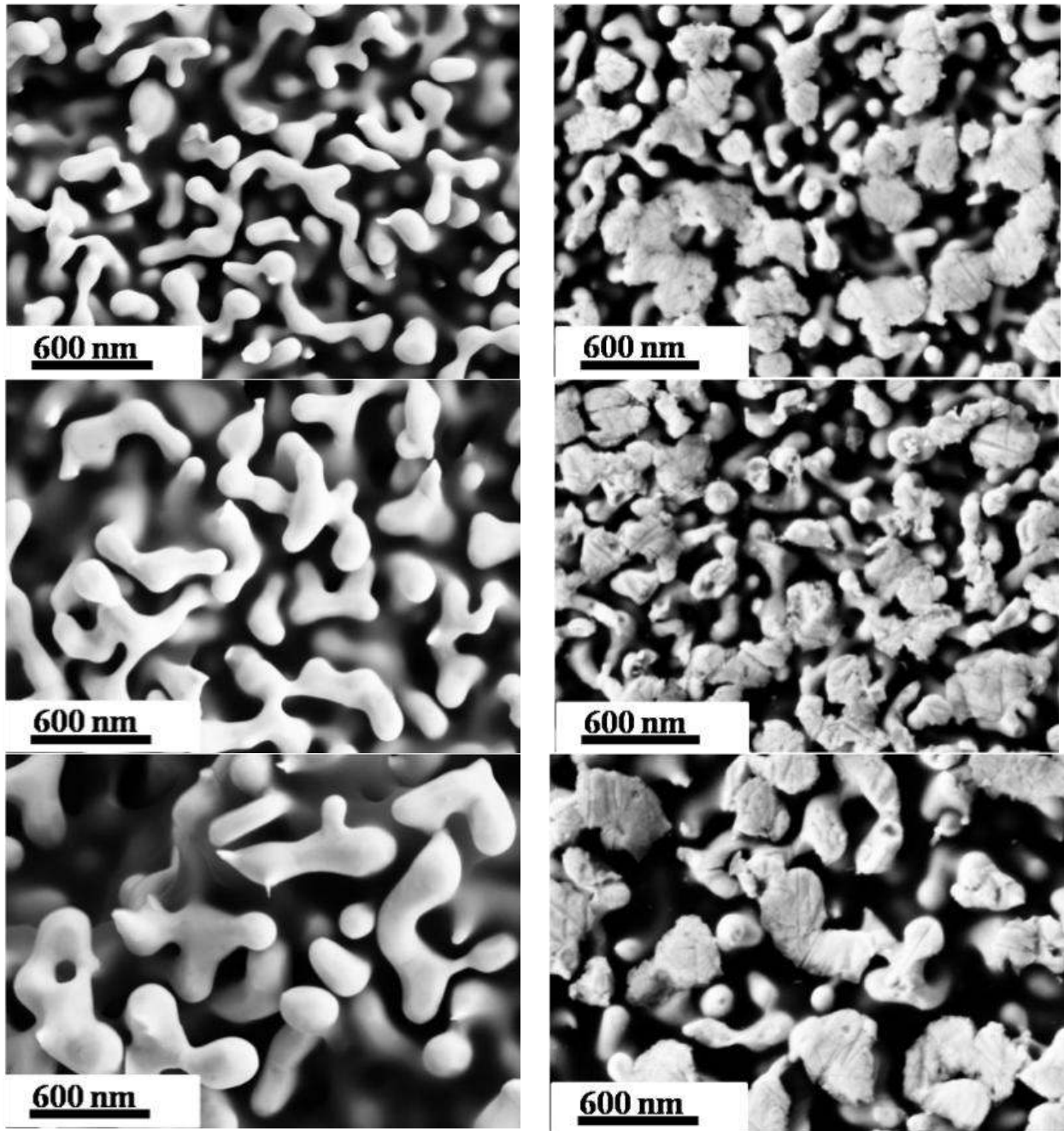


*Figure 8: Scanning electron micrographs of original (left column) and polished (right column) cross-sectional cut surfaces of RIM-npg composites. Top image reveals mean ligament diameters,  $L$ , of 20 nm in the as-dealloyed npg. Following top image, images from top to bottom show npg samples with ligament diameter of about  $50\pm 10$ ,  $80\pm 20$ ,  $120\pm 30$ ,  $150\pm 50$  and  $250\pm 50$  nm, which were prepared by annealing in air at 300 °C for 2, 5, 10, 30 minutes and 3 hours, respectively. Epoxy phase gives no contrast in the SEM and therefore is not imaged. Note that the ligament structure is conserved in spite of the polishing. This can only be explained by stabilization of the metal microstructure through the interpenetrating epoxy. Integrity of the microstructure on all cross-sections supports complete impregnation.*



EDX in the scanning electron microscope finds a uniform carbon signal on cross-sections of all composite samples (see Figure 9B), compared to EDX for pure npg (see Figure 9A), suggesting the complete impregnation. This notion is further confirmed by the SEM images of polished cross-sections in Figure 8 (right column). The polymer phase is not apparent in SEM images, however, its presence is evidenced by the conservation of the metal nanostructure. Polished surfaces of native npg, Figure 10, appear dense and featureless in the SEM due to the fact that polishing destroys the fragile ligament structure. By contrast, the ligament structure of the composites with different ligament size is perfectly retained at polished surfaces of the composite, Figure 8 (right column), even though the stabilization of the ligament structure decreases with increasing ligament size. This results from the stabilization of the metal phase against collapse by the interpenetrating polymer phase. The retention of the nanoporous structure in composite after polishing therefore testifies to the uniform and complete infiltration of the porous metal with polymer.

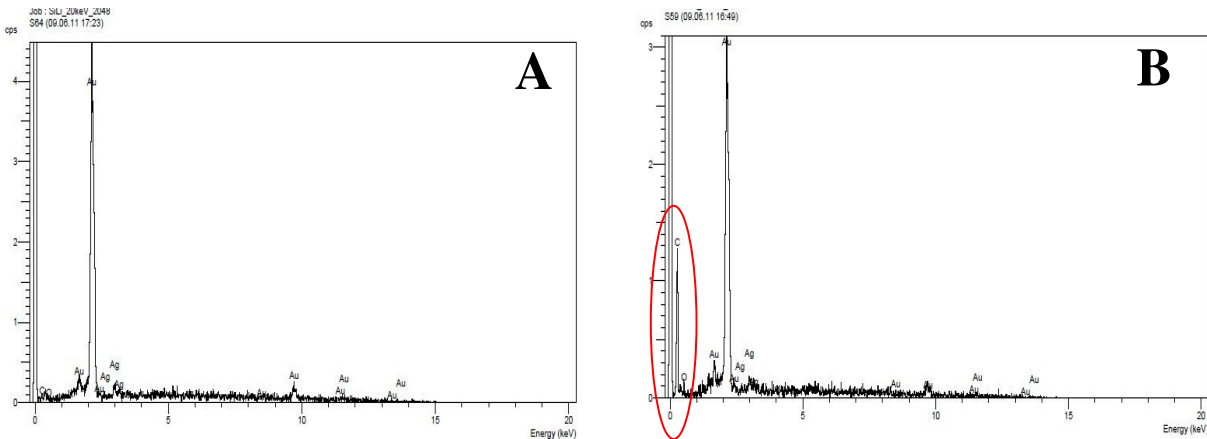


Figure 9: EDX in the scanning electron microscope for pure npg (A) and BE-npg composite (B). EDX finds a uniform carbon signal on cross-sections of all composite samples, suggesting the complete impregnation.

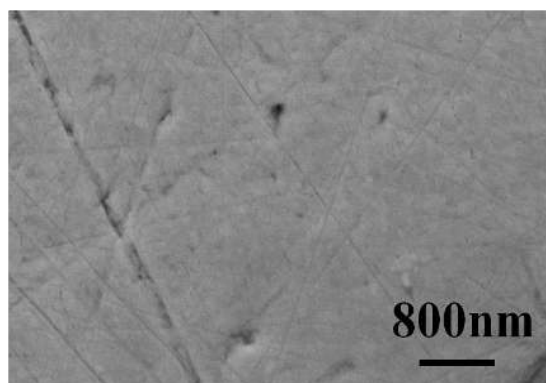
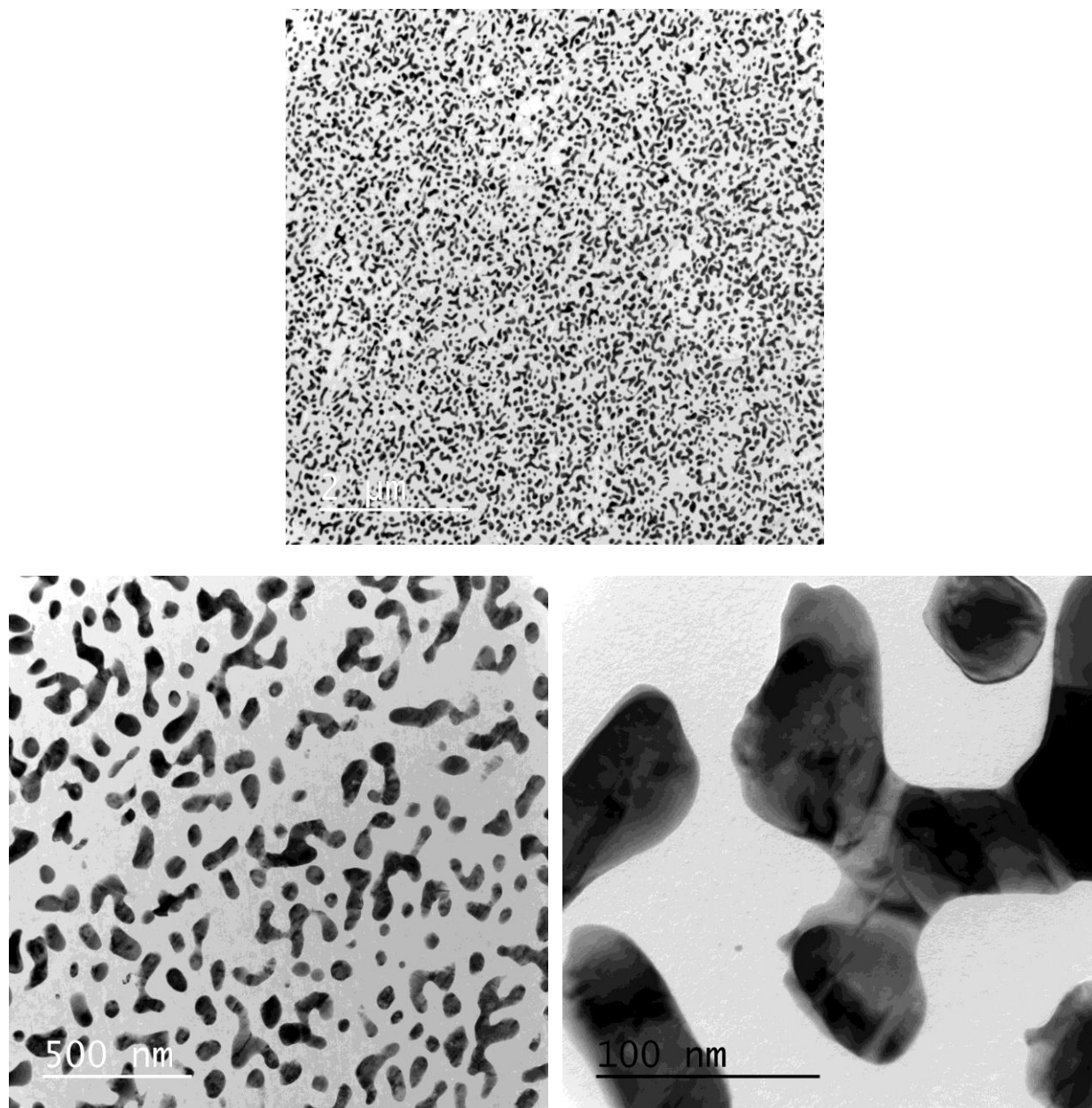


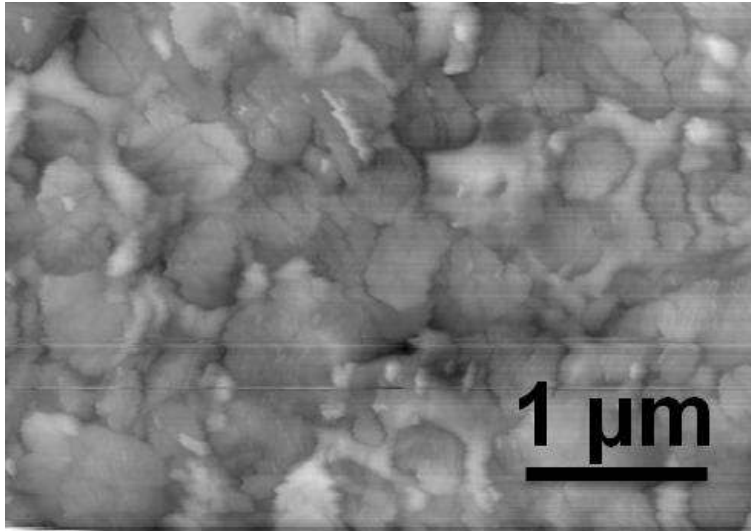
Figure 10: Scanning electron micrograph of a cross-sections surface of uninfiltred nanoporous gold with ligament size of 150 nm after polishing. Polishing destroys the microstructure of npg.

Figure 11 shows transmission electron microscope images of cross-section of RIM-npg composite with ligament size of 50 nm, which was prepared by microtome cutting, in different magnifications. The polymer phase is apparent in TEM images: gray phase is polymer and black phase is Au ligament. TEM images proved presence of polymer and confirmed complete infiltration. Extensive investigations of cross sectional TEM micrographs revealed no voids in the polymer.



*Figure 11 Transmission electron microscopy of a cross-section for the RIM-npg composite ( $L = 50$  nm) prepared by microtome cutting. The polymer phase is apparent in TEM images. Gray phase is polymer phase and black phase is Au ligament. TEM investigations of cross-sectional micrographs revealed no voids in the polymer.*

The complete infiltration is also confirmed by the AFM image of polished cross-section of composites in Figure 12. The polymer phase is apparent in AFM image, AFM investigation of cross sectional micrograph also revealed no voids in the polymer.



*Figure 12: Atomic force microscopy of a cross-section for the RIM-npg composite with ligament size of 150 nm after polishing. AFM investigation of cross-sectional micrograph revealed no voids in the polymer.*

## 3.2 Electrical properties

An exemplary study of electric conductivity was performed on several BE-based composite samples with  $L$  of 150 nm. Resistance measurements on samples with dimension of  $4.2 \times 1.8 \times 0.6$  mm<sup>3</sup> resulted in the electric conductivity value of  $260 \pm 30$  kS/m at 298 K. At roughly 1% of the conductivity of massive high-purity Cu, this is considerably larger than state-of-the-art composites of epoxy and carbon nanotubes, which reaches 13 kS/m<sup>[161]</sup>. The material achieves a near metallic conductivity, predestining it for applications where, for instance, static electric charging needs to be avoided or lightning-strike tolerated.

## 3.3 Thermal properties

The interpenetrating polymer phase of the composite exhibit a glass transition temperature,  $T_g$ , which is defined as the temperature at which amorphous, in other words noncrystalline polymers are transformed from a glassy, brittle state to a liquid or rubbery state, that is to say, if curing has already occurred.<sup>[162]</sup> It is important to note that it involves a local degrees of freedom change. Moreover, there are segmental motions above the glass transition temperature are relatively unhindered by neighboring chains. On the other hand, such motions are restricted to a great extent below the glass transition temperature and they are characterized by relatively long

relaxation times in comparison to the experiment's duration. It is a significant feature of the polymer, especially because mechanical behavior of polymers alters to a great extent at the glass transition temperature. Above the glass transition temperature, the properties of the material such as elastic modulus degrade significantly. In order to assure that the mechanical stiffness and creep resistance of the material is satisfactory in structural application, it is necessary that the application temperature for a polymeric composite is below the glass transition. The glass transition temperature, or typically a temperature well below the  $T_g$ , is often as an upper limit for the use of polymeric composites in structural applications.<sup>[162]</sup> The  $T_g$  of a material is usually measured by such thermal analysis techniques as differential scanning calorimetry (DSC), dynamic mechanical analysis (DMA), or thermo mechanical analysis (TMA). Although there are several thermal techniques available to make  $T_g$  measurements, by far the most sensitive technique is DMA.

In this work, the thermal properties of RIM-based composite and pure RIM epoxy have been studied by dynamic mechanical analysis. As was described in synthesis section 2.2.4, some of the specimens were post-cured at 60°C for 24h. Figure 13 shows the tan delta vs. temperature for RIM-based specimens that were post-cured for 2h and 24h, respectively. The glass transition temperature was determined from the peak of the tan delta curve, which is a good measure of the midpoint between the glassy and rubbery states of a polymer.<sup>[152]</sup>

RIM epoxy is a thermosetting polymer that undergoes an irreversible chemical reaction, known as curing, which produces a crosslinked structure.<sup>[162]</sup> The ultimate  $T_g$  of a thermoset material is determined by a number of factors: the chemical structure of the epoxy resin, the type of hardener and the degree of cure.<sup>[162]</sup>  $T_g$  increases significantly as the curing reaction proceeds to completion due to the decrease in the system's mobility caused by the formation of covalent bonds.<sup>[162]</sup> Eventually, as the thermoset completely cures, the  $T_g$  of the material will reach a limiting value.<sup>[162]</sup>

Figure 13 shows that the  $T_g$  of pure epoxy is larger than that of composites, especially for small- $L$  samples. It can be described in terms of the amine hardener depletion due to the formation of covalent bonds between amine groups and gold surface<sup>[147]</sup> when epoxy-amine hardener liquid mixtures are infiltrated into nanoporous gold. The depletion of amine hardener leads to a decrease of the curing degree of epoxy phase in composite. Figure 14 shows the graph of the  $T_g$  of RIM-epoxy and RIM-based composite specimens that were 24h post-cured versus different ligament size. It is found in Figure 14 that the glass transition temperature of RIM-based composite depends on the ligament size. A downward shift of the glass transition temperature for composite at small ligament size was observed in Figure 14. It could be attributed to the increase of surface per volume at small ligament size composite. The increase of the surface area by decreasing the ligament size will promote the amine hardener depletion.

Figure 13 shows that the  $T_g$  for the 24h post-cured specimen (see Figure 13(B)) is larger when compared to the 2h post-cured specimen (see Figure 13(A)). For instance,  $T_g$  of RIM-based composite with  $L = 50$  nm increases from 64 °C for 2h post-cured specimen to 87 °C for 24h post-cured specimen. Results indicate that  $T_g$  increases with increasing of post-cure time. It is

also speculated that this treatment will lead to enhanced mechanical properties. In some epoxy-based systems, the cure reaches a point where increased post-cure time causes little to no increase in either the modulus or  $T_g$ .<sup>[152]</sup> At this point, increased post-curing gives no advantage and only wastes money and time. In some systems, this occurs as low as 94% of complete cure.<sup>[152]</sup> Future experiments with a more purposeful curing step in the sample preparation are necessary in order to be aware of this value and of where full mechanical strength is developed.

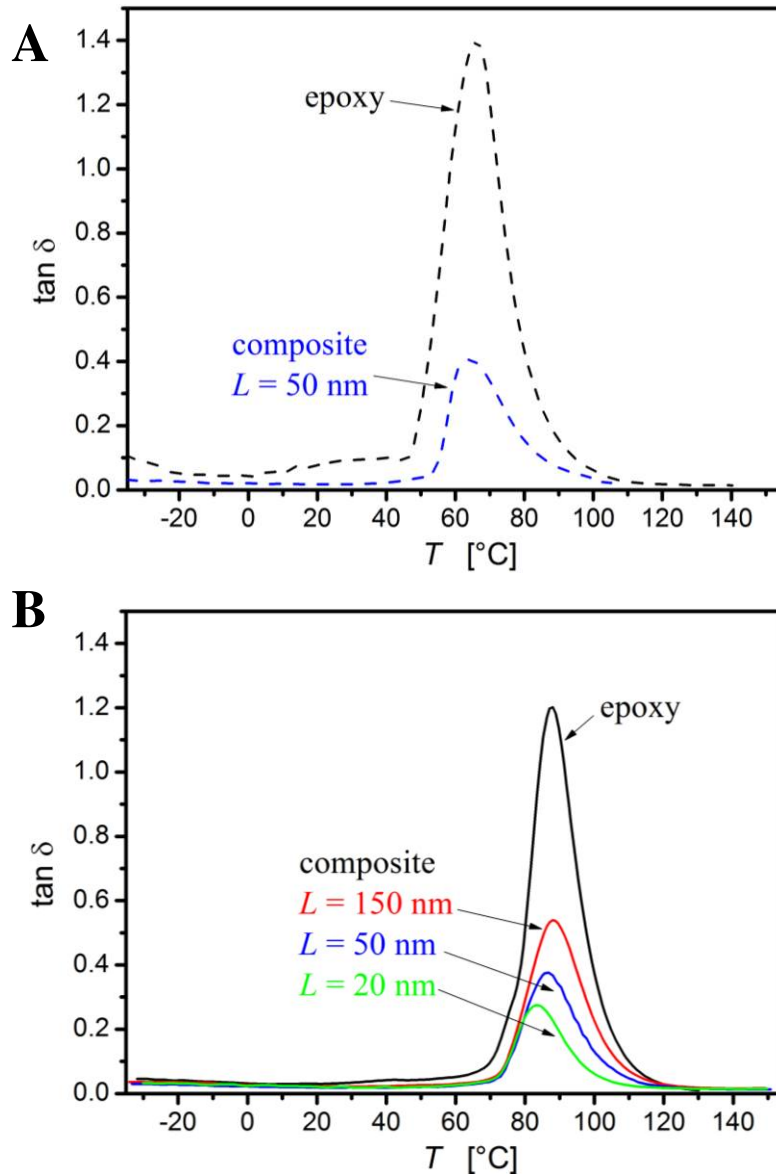


Figure 13: Tan delta,  $\tan \delta$ , determined from DMA vs. temperature,  $T$ , curves for (A) RIM epoxy and RIM-npg composite with ligament size,  $L$ , of 50 nm that were 2h post-cured, and for (B) the epoxy and composite with  $L$  of 20, 50 and 150 nm specimens that were 24h post-cured. The glass transition temperature was determined from the peak of the tan delta curve.

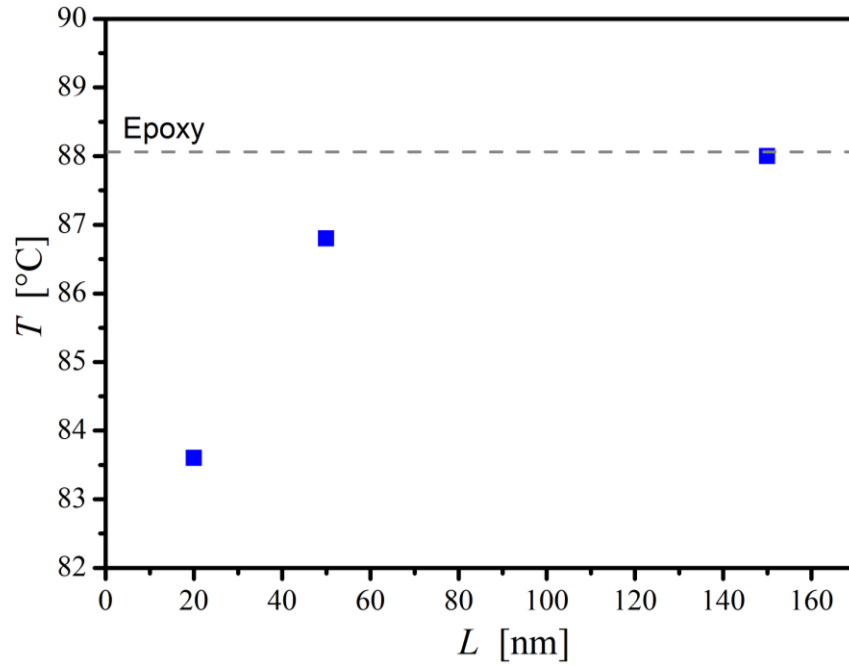


Figure 14: Glass transition temperature,  $T_g$ , of RIM-based composite specimens (blue squares) that were 24h post-cured versus ligament size,  $L$ , and  $T_g$  of RIM epoxy (gray dash line) that was 24h post-cured. The glass transition temperature of composites decreases with decreasing ligament size.

# Chapter 4.

## Plastic deformation

In this chapter plastic deformation observed in both compression and tension for npg-based composites is systematically studied taking into account different ligament size and varied interpenetrating polymers. The plastic deformation behavior of composite is compared with their constituent materials, such as npg and polymer. It concentrates on researching ductile behavior and strength of composites since the main purpose of this work is to create high-strength and ductile npg-based nanocomposite materials. A full understanding of structure-property relations of npg-polymer composites and native npg will be further researched.

### 4.1 Compression

#### 4.1.1 Experimental results

##### *4.1.1.1 Vickers hardness tests*

The Vickers microhardness,  $H_v$ , for all composite materials and their constituent phases are tabulated in Table 1. In case of some types of composite materials, it is difficult to measure the residual indentation diagonals due to the fact that indentation marks are not visible, especially when ligaments sizes are bigger. This is why there is no hardness data for PU-npg composites at 150 nm.

Figure 15(A) displays results of Vickers microhardness tests on the RIM-npg composite material and on its individual constituent phases versus different ligament size. Figure 15(B) and (C) show optical micrographs of indentation marks of Vickers hardness test in npg and BE-based composite with ligament size of 150 nm. It is observed that there are a lot of cracks surrounding the indent in npg, while in the indent of the composite, it is free of cracks.

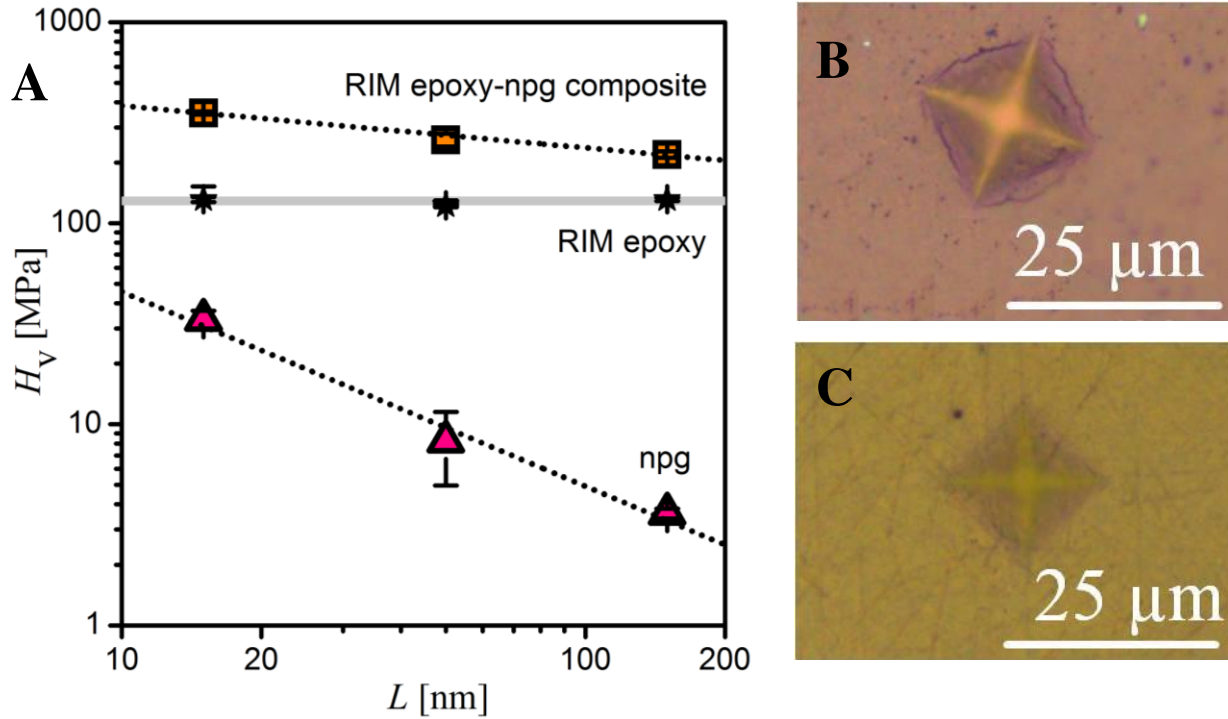


Figure 15: (A) Vickers microhardness,  $H_V$ , of npg, RIM epoxy and RIM-npg composite samples versus the ligament size,  $L$ . Epoxy samples were taken from the same mould as the composites and data is plotted at the respective  $L$ -value. Dotted lines represent best linear fits; grey line is a guide to the eye. Hardness data is tabulated in Table 1. Representative optical micrographs showing indentation marks of Vickers microhardness tests<sup>[36]</sup>: (B), as-prepared npg; (C), BE-based composite sample. Ligament size is 150 nm. Note cracks in npg and absence of cracks in composite.

From Figure 15 (A), it is observed that the hardness values for npg agrees well with the previously reported trend of increasing  $H_V$  with decreasing  $L$ . The dotted lines represent the best linear fits in the log-log graph, which gives a power-law  $H_V \propto L^{-1.0 \pm 0.1}$  for npg. It is steeper than in some of the previous data but in agreement with Ref. [19]. It is speculated that the samples densify during coarsening, and that increasing strength of metal foams at higher density may partly compensate the decreasing strength of the ligaments at larger  $L$ .  $H_V$  data from the epoxy were taken on samples collected from the same mould as the respective composite samples and are displayed at the  $L$ -value of the respective composite. The data testifies to a well reproducible, constant hardness of the pure epoxy. At  $H_V = 114 \pm 3$  MPa, the hardness of epoxy considerably



exceeds that of the nanoporous gold (around  $H_V = 33$  MPa with ligament of around 20 nm). Nonetheless, the hardness values for the composites are again higher. In fact, at  $H_V = 353 \pm 7$  MPa the hardest composite is threefold harder than the epoxy. Straight-line fits the composite data that gives  $H_V \propto L^{-0.21 \pm 0.01}$ . From Table 1, it could be seen that the Vickers hardness of RIM-npg composite increase with decreasing ligament size.

#### 4.1.1.2 Instrumented indentation test

For some composite materials, it is impossible to measure hardness value by the Vickers hardness method because the end edge of indentation marks is unclear. Due to the limitation of Vickers hardness method, the hardness of composites was also measured by the instrumented indentation method. An advantage of this method is that the hardness value can be directly determined from the indentation load-displacement curve without the need of optically observing the indentation marks. However, in this device the sample has to be fixed by a special cylinder ring, what make the application of this method impossible for npg because the it would be crushing.

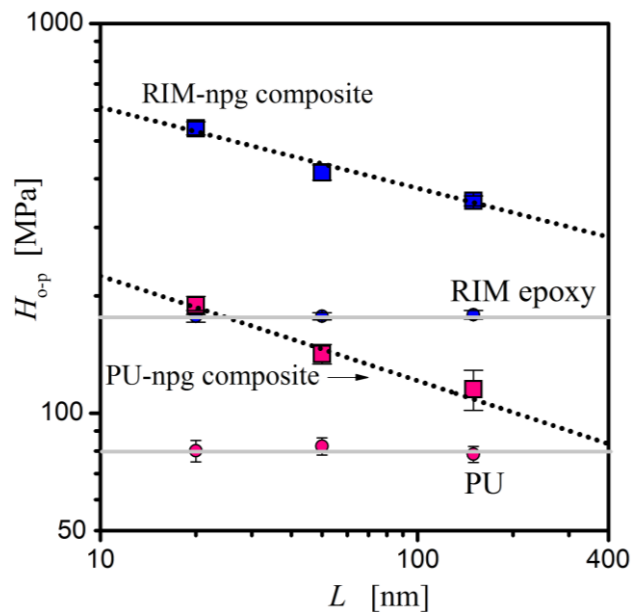


Figure 16: Hardness determined by Oliver and Pharr method,  $H_{o-p}$ , of composites versus ligament size,  $L$ . Polymer samples were taken from the same mould as the corresponding composites and data are plotted at the respective  $L$ -value. The gray line is a guide to the eye. Hardness data are tabulated in Table 1.

Figure 16 shows the hardness value determined by Oliver and Pharr method,  $H_{o-p}$ , for RIM- and PU-based composites and their polymer material, the numerical values are tabulated in Table 1. The source of  $H_{o-p}$  data in case of the polymer were samples collected from the same mould as

the respective composite samples. This data is presented at the  $L$ -value of the respective composite where the grey line serves as a guide to the eye. Moreover, the polymer's hardness data is found to be constant and well reproducible. The  $H_{O-P}$  of RIM epoxy is around  $179\pm 2$  MPa and that of PU is around  $80\pm 4$  MPa. Still, it can be noticed that the hardness values are higher for the composites. For example, with a ligament size reaching 20 nm, the RIM-npg hardness is three times higher compared with the RIM epoxy. The RIM-npg composite hardness data are fit straight-line which gives  $H_V \propto L^{-0.21\pm 0.03}$  and the PU-npg data gives  $H_V \propto L^{-0.27\pm 0.04}$ .

*Table 1: Numerical values from microhardness tests of the composites and of its constituents, nanoporous gold (npg) and polymer.  $L$  – ligament size;  $H_V$  – Vickers hardness,  $H_{O-P}$  – instrumented hardness;  $E$  – elastic modulus, which is calculated according to the load-displacement data of the instrumented hardness test. The instrumented hardness test cannot be performed on the npg samples.*

	$L$ [nm]	$H_V$ [MPa]	$H_{O-P}$ [MPa]	$E$ [MPa]
npg	20nm±5nm	33±4.0	—	—
	50nm±10nm	8.2±3.0	—	—
	80nm±20nm	8.0±2.5	—	—
	150nm±50nm	3.6±0.2	—	—
	250nm±50nm	3.5±0.3	—	—
RIM-npg composites	20nm±5nm	353.4±6.5	538.7±20.5	11.2±0.3
	35nm±10nm	318.5±8.7	479.8±17.7	10.7±0.3
	50nm±10nm	259.7±19	401.9±18.0	10.4±0.2
	80nm±20nm	237.5±5.3	379.7±8.0	10.2±0.5
	120nm±30nm	227.4±7.1	352.0±9.6	10.1±0.4
	150nm±50nm	219.5±8.2	349.2±7.9	9.9±0.4
	250nm±50nm	214.4±5.1	336.8±5.1	9.6±0.3
RIM		114±3.0	179±2.0	4.2±0.2
PU-npg composites	20nm±5nm	144.1±12.1	189.4±10.2	6.0±0.3
	50nm±10nm	126.4±3.7	141.9±8.1	4.9±0.2
	150nm±50nm	—	115.2±13.5	4.4±0.3
PU		—	80.1±4.2	1.6±0.1

### 4.1.1.3 Compression tests

As a preliminary to the results obtained with composite samples, Figure 17 shows compression stress-strain curves of npg samples with different ligament size. The stress-strain curves of npg illustrate the excellent deformability of npg in compression. Three regions may be distinguished for the as-prepared npg with  $L = 20$  nm: an initial regime of apparent linear elastic strain is followed by a gradual elastic-plastic transition region, after which the flow stress continuously increases. For npg samples with larger  $L$ , the yield stress is not resolved, and the plastic flow behavior is characterized by a continuously increasing flow stress, for instance from an initial  $\sim 1$  MPa to  $> 150$  MPa for  $L = 150$  nm sample. The absence of transverse plastic flow, which underlies the work hardening, is illustrated by the images of npg before and after compression, see inset in Figure 17. It is observed in Figure 17 that the plastic flow stress of npg increases with decreasing ligament size.

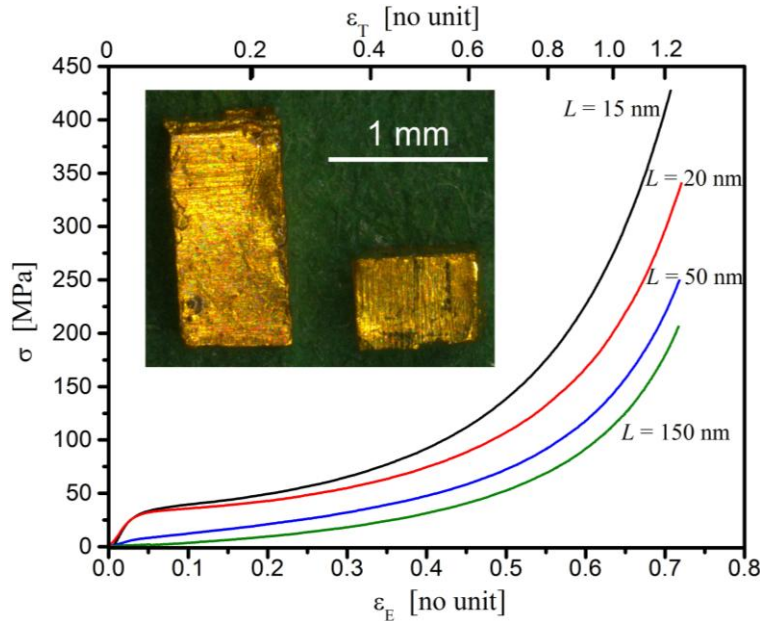


Figure 17: Compressive true stress,  $\sigma$ , versus engineering strain,  $\epsilon_E$ , curves of pure npg with cylinder shape of initial dimension  $\sim 1 \text{ mm}^2 \times 1.7 \text{ mm}$ , with true strain,  $\epsilon_T$ , shown on the top abscissa. Tests were performed to engineering strain of 0.7, corresponding to nearly full density for the nanoporous gold samples. The inset<sup>[36]</sup> displays side views of as-tested npg samples before (left) and after (right) compressive deformation to  $\epsilon_E$  of 0.6, illustrating absence of transverse plastic flow. Data for yield strength is tabulated in Table 2.

Figure 18 shows compressive stress-strain curves for mm-sized composite samples with different ligament size and various polymer phases. The graphs show engineering strain values up  $\epsilon_E = 0.5$ . All samples could be deformed plastically up to higher nominal strain of at least 0.7 without failure, yet the increasing lateral flow at the high strains prevents a meaningful discussion of the

relevant data because an obvious sample barreling was observed after  $\epsilon_E$  of  $\sim 50\%$ . As measures for strength we use – where possible – the 0.2%-offset strain yield strength,  $\sigma_{0.2}^Y$ , as a more robust but less fundamental measure. The  $\sigma_{0.2}^Y$  was determined as the stress where the line with the same slope as the linear elastic curve at 0.2%-offset intersects the stress-strain curve. Table 2 summarizes the 0.2%-offset yield strength for different kinds of composites and their individual constituent npg as well as polymer phase.

The compressive stress-strain curves for the polymers are included in Figure 18. Clear yield points are distinguished for the two epoxies, followed by regions of approximately constant flow stress and a final work hardening stage prior to failure. The PU behaves similarly except for the absence of a clear yield point. The strengths vary considerably, with the RIM being strongest, the BE only about half as strong and the PU again weaker by half.

Composite samples with  $L = 20$  nm typically fail at lesser strain than those with larger ligaments, and also exhibit a somewhat larger sample-to-sample scatter in yield stress. Yet, it is apparent that all composite materials exhibit excellent deformability in compression. The composites showed a significantly different stress-strain behavior as compared to pure npg. Yielding is well defined for the RIM- and BE-based samples. The PU-based material exhibits a more gradual elastic-plastic transition, yet its initial stress-strain response is still considerably steeper than in case of the metal samples. A more gradual increase in the initial stress of the PU-composite at larger ligament size reflects the enhanced initial elastic-plastic compliance of the pure npg samples at larger  $L$ . Each type of composite shows a strong increase in flow stress with decreasing metal ligament size, emphasizing that the strengthening of the metal at small structure size is indeed transferred into the composite. The composites are significantly stronger than the respective pure polymers. For the strongest composite, RIM in  $L = 20$  nm npg, the compressive yield strength reaches 120 MPa.

As opposed to npg, in case of composite samples stress-strain curves show a strong decrease in work hardening. While the work hardening index varies between  $n = 1$  and 0.5 for npg samples in the course of the compression test, whereas the  $n$ -values for the BE-npg composite samples for strains sufficiently beyond the yield point are much smaller, never exceeding  $6 \times 10^{-2}$  for  $L = 20$  nm and  $4 \times 10^{-3}$  for the larger  $L$ .

An exemplary study of the volume change was performed on npg, BE epoxy and the BE-based composites. As expected, the change in macroscopic volume,  $\Delta V$ , is suppressed in the composites. The native npg samples exhibit relative volume shrinkage (density increase) of  $\Delta V/V \sim -0.62 \pm 0.05$  for  $L = 150$  nm and  $\Delta V/V \sim -0.72 \pm 0.04$  for  $L = 50$  nm during an engineering strain of -0.70, bringing the solid fraction,  $\phi$ , after compression close to 1. By contrast, the volume of the BE-npg composite sample changed only slightly. For a compressive strain of -0.71, we found  $\Delta V/V_0 \sim -0.03 \pm 0.01$  for a diameter of 150 nm and  $-0.046 \pm 0.01$  for a diameter of 50 nm. A similar volume change,  $-0.025 \pm 0.01$  is found for the pure epoxy sample. The slight decrease of the composites' macroscopic volume may be understood as the result of the rearrangement of polymer chains under compressive stress.<sup>[163]</sup>

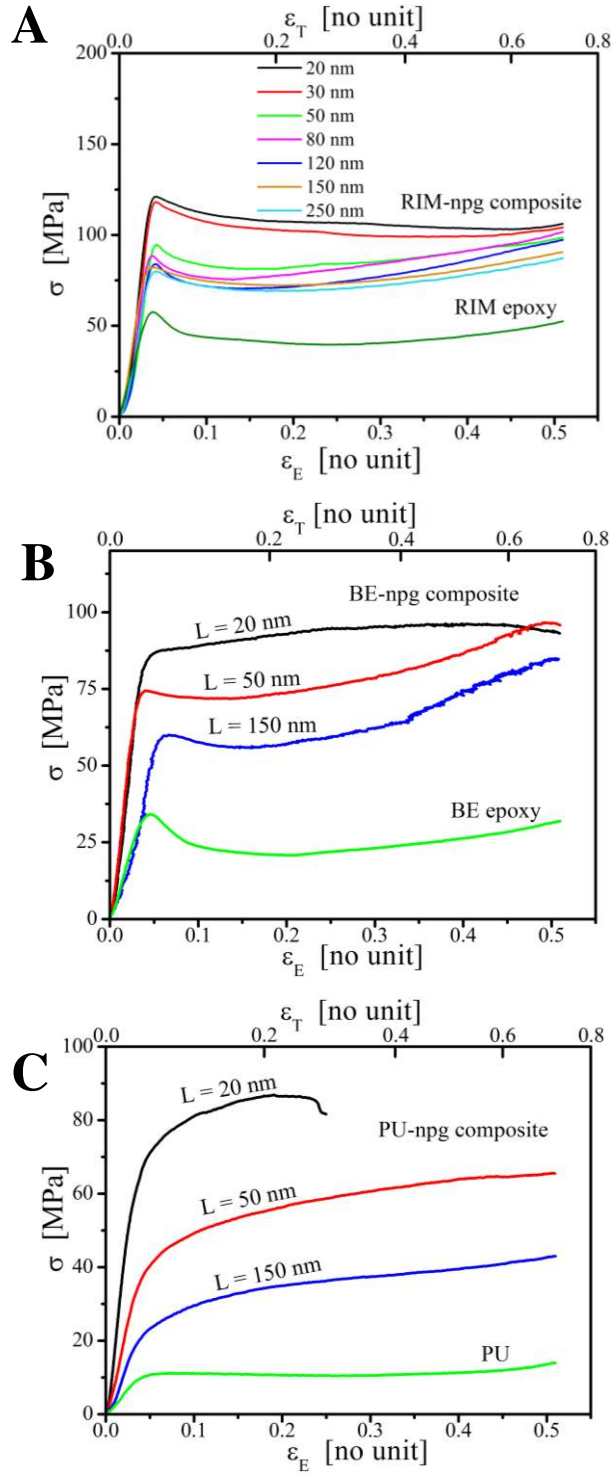


Figure 18: True compressive stress,  $\sigma$ , versus engineering strain,  $\epsilon_E$ , curves of compression tests, with true strain shown on the top abscissa. Tests were performed at strain rate of  $10^{-4} \text{ s}^{-1}$  on composites with different ligament size,  $L$ , and polymers: (A) RIM-npg composites and RIM epoxy, (B)<sup>[36]</sup> BE-npg composites and BE epoxy, (C) PU-npg composites and PU. Data for yield strength are tabulated in Table 2.

Table 2: Numerical values of structural and mechanical characteristics in compression tests of all composites and their constituents, nanoporous gold (npg) and different polymers.  $L$  – ligament size;  $E$  – elastic modulus,  $\sigma_Y^{0.2}$  – 0.2% offset yield stress. For the npg samples with ligament size of 150 nm, elastic region and yielding is not resolved in the stress-strain curves.

	$L$ [nm]	$E$ [GPa]	$\sigma_Y^{0.2}$ [MPa]
npg	20	0.81	20±1
	50	0.17	5.1±0.2
RIM-npg composites	20	4.18	115±5
	35	4.01	112±5
	50	3.34	90±3
	80	3.21	85±1
	120	3.12	78±4
	150	2.98	75±4
	250	2.39	73±3
RIM epoxy	—	1.25	56±3
BE-npg composites	20	2.78	80±10
	50	2.74	66±3
	150	1.69	54±3
BE epoxy	—	1.05	28±3
PU-npg composites	20	2.36	52±1
	50	1.14	32±1
	150	0.71	18±1
PU	—	0.31	9±0.5

Figure 19 shows cross-sectional SEM images of npg and composite samples after compression. The cross-sectional surface of compressed npg was obtained by bending the sample (after the compression test) with the help of tweezers, inducing brittle fracture. Due to their ductility, the composite samples could not be fractured in this way and had to be cut. It is apparent that the metallic ligaments have not failed during the compression tests. This is consistent with the notion of ductile deformation at the nanoscale. Figure 19(a) shows stronger densification in compressed npg, while the SEM image of compressed composite shows an apparent texture, with a preferential alignment of the ligaments normal to the load axis.

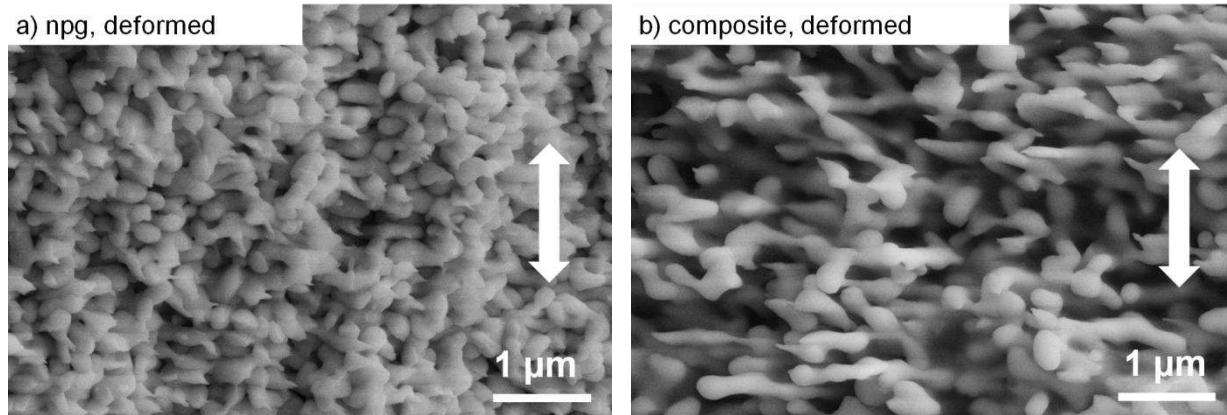


Figure 19<sup>[36]</sup>: Scanning electron micrographs of cross-sections of materials with ligament sizes of 150 nm after compression to engineering strain 0.7 (arrows: compression direction). (a) Cross-sectional surface of the compressed npg sample; (b) Cross-sectional surface of compressed composite. Note the much stronger densification in npg. Also note that ligaments do not break except at the macroscopic cut/fracture surface. The polymer phase is transparent in the images. The SEM image for the composite shows an apparent texture, with a preferential alignment of the ligaments normal to the load axis.

## 4.1.2 Discussion

### 4.1.2.1 Microhardness testing

The microhardness results from the two microhardness tests presented in the previous section were discussed in order to compare the hardness of composite to its parent materials, npg and polymer. The Vickers hardness of both npg and composite is size-dependent. It increases with decreasing ligament dimension. Even though the size-dependence of the hardness is weaker for the composite than for npg, the data shows that the enhanced strength of the nanoscale ligaments propagates into enhanced composite mechanical properties. Remarkably, the hardness of the npg-polymer composite of any  $L$  exceeds that of each of its constituent phases.

The  $H_{o-p}$  values of composites increase with decreasing  $L$ , which agrees well with the previously reported trend in Vickers hardness, even though the deformation and calculation methods are different for the two hardness tests. It was noted that the difference of hardness values between polymer and the composites are bigger when the ligament sizes are smaller. This observation will be discussed together with the results of the compression test.

#### 4.1.2.2 Compressive plastic deformation

From Figure 17 and Figure 18, it is apparent that all materials exhibit excellent deformability in compression although the stress-strain relationship of the composites, nanoporous gold and polymer are different. Figure 17 shows that for npg samples with larger  $L$ , the apparent elastic regime is suppressed in favor of immediate onset of plastic deformation. This agrees with previous results in Ref. [164]. The behavior, in fact, resembles that of well-annealed single crystal samples<sup>[63]</sup>. Figure 18 clearly shows that the strength of the composites at any given  $L$  follows the trends of the polymer strengths, with RIM-composites stronger than BE- and then PU-based composites. Furthermore, the characteristics of the composites also follow the trend of “smaller is stronger” that is so clearly confirmed by the npg samples. Finally, the strength of the composites also exceeds those of the constituent phases at any  $L$ , which agrees well with hardness data.

The work hardening behavior of npg is unusual in as much as the work hardening rate increases with increasing strain. In relation to plasticity, experiments show practically no transverse plastic strain in the macroscopic during plastic compression under uniaxial load. The fact that transverse plastic strain is absent in macroscopic nanoporous material seems to suggest that the process of compression in case of uniaxial stress is conducted by the densification of the ligaments' network. By virtue of the scaling<sup>[64]</sup> of the flow stress,  $\sigma_F$ , with solid volume fraction,  $\varphi$ , as  $\sigma_F \propto \varphi^{3/2}$ , the densification causes a particularly strong work hardening at the macroscopic scale<sup>[19]</sup>.

The study of the volume change with deformed pure npg and the BE-based composites shows that the composite increase the transverse plastic strain and suppress the change in macroscopic volume during plastic compression, whereas the pure npg samples deformed by densification with no detectable transverse plastic strain. As opposed to npg, the composite samples and particularly those RIM epoxy based exhibit extended regimes of almost constant flow stress, see the stress-strain curves in Figure 18. It supports the observation of the suppression of densification which causes work hardening in case of pure metal samples. It is a fact that, work hardening can be suppressed if the densification is suppressed by infiltrating the npg pores with a polymer.

From Figure 19, it is natural to assume that impregnation with polymer changes the mode of deformation of the metal. Similarly to a conventional metal foam,<sup>[64]</sup> the pure nanoporous metal may deform at low stress by local bending of the ligaments. The ensuing densification is apparent when Figure 19 (a) is compared to Figure 8 (left column). In contrast to the pure porous metal case, the embedding in a composite matrix forces the ligaments to strain along with an



essentially volume-conserving macroscopic flow field. This emphasizes axial elongation or shortening of ligaments in the local deformation modes, as supported by the horizontal texture and the elongated aspect of the ligaments in Figure 19 (b).

#### 4.1.2.3 Theory of npg-polymer composite materials

The strength,  $\sigma^{\text{eff}}$ , of nanoporous metal-polymer composites was found to considerably exceed that of each of the constituent phases. This statement is connected with a simple rule of mixtures approach, in which the nanoscale metal network maintains its (effective, macroscopic) strength,  $\sigma^{\text{N}}$ , and in which the polymer component contributes in proportion to its volume fraction,  $1-\varphi$  where  $\varphi$  denotes the metal volume fraction, and to the strength,  $\sigma^{\text{P}}$ , of bulk polymer:

$$\sigma^{\text{eff}} = \varphi \sigma^{\text{N}} + (1-\varphi) \sigma^{\text{P}} \quad (20)$$

It is characteristic of the present type of composites that the reinforcing metal phase exists in the form of load bearing monolithic bulk samples that can be tested, providing experimental data for  $\sigma^{\text{N}}$ . Since  $\varphi$  and  $\sigma^{\text{P}}$  are also known, the prediction of the rule of mixtures, Eq. 20, may be compared to experimental data for the strength of the composite. This experimental strength is found to be much higher than the prediction of the simple estimate. This is not surprising, since the deformation mode of the metal changes when the pore space is filled with polymer, so that load no longer densifies the metal network and plastic deformation is instead carried by a volume-conserving flow field, similar to conventional massive materials. Here, the mechanical behavior of the composites will be discussed in relation to a more conventional rule of mixtures approach.

##### *An alternate rule of mixture*

It is of interest to separate the contributions of the polymer matrix and the embedded metal network to the net load carried by the composite. For the elastic problem this is a classic problem of heterogeneous medium theory that has approximate solutions in the form of, for instance, the Hashin-Shtrikman model.<sup>[132]</sup> Here the focus is on the plastic deformation, which is open to a simpler, if also approximate, analysis.

The key observation is that, as interconnected networks of nanoscale metal ligaments which are infiltrated with a polymer, the npg-polymer materials are interpenetrating phase composites. The reinforcing nanoscale metal network on its own thus forms massive samples that can be tested, see the results in Figure 17. As the experiment sets the strength of the composites several times higher than either the pure nanoporous metal or the pure polymer, a rule of mixture based on the weighted sum of the strength of the individual phases, as in Eq. 20, does not appropriately describe the mechanical behavior of the polymer.

The failure of Eq. 20 is not surprising, since filling the pore space with the polymer changes the mode of the formation of the nanoscale metal network. While compression of the pure nanoporous metal is carried entirely by densification, plastic flow of the composite material at

constant effective macroscopic flow stress  $\sigma^{\text{eff}}$  involves a volume-conserving flow field. In fact, plastic flow of the bicontinuous microstructure is consistent with metal and composite deforming coherently with uniform and identical values of the strain rate,  $\dot{\epsilon}$ , in each phase. This flow field is also consistent with constant (but not necessarily uniform) stress at each material point in each phase and, therefore, with a volume-conserving flow. In fiber-reinforced composites, relaxation at the fiber ends and slip at the fiber-polymer interface are well known to imply a significant deviation from the uniform strain rate that requires correction, for instance by a “strength efficiency factor”.<sup>[97]</sup> Furthermore, the essentially brittle behavior of classic reinforcements such as carbon fibers prevents the coherent plastic deformation of fiber matrix and leads, instead, to failure at small plastic strain. The present material presents a more benign case for analysis, since the stiff phase is locally ductile, and since the requirement of maintaining contiguity in the bicontinuous microstructure enforces the plastic flow to be coherent.

The material used is macroscopically isotropic and it may be safely assumed that this isotropy can be carried over to the local flow field. In doing so, the crystalline anisotropy of the metal is ignored of the metal in each of the randomly oriented grains (a few tens of micron in size<sup>[19]</sup>) of the metal microstructure. The assumption appears reasonable since pure nanoporous gold does deform uniformly at the micron scale.<sup>[19]</sup>

If one accepts the flow field as volume-conserving and the material as isotropic, then the uniaxial load simply leads (in an orthonormal coordinate system) to a strain rate tensor,  $\dot{E} = dE/dt$ , according to

$$\dot{E} = \dot{\epsilon} \begin{pmatrix} -\frac{1}{2} & 0 & 0 \\ 0 & -\frac{1}{2} & 0 \\ 0 & 0 & 1 \end{pmatrix} \quad (21)$$

In other words, the plastic flow is parameterized by the scalar strain rate  $\dot{\epsilon}$  alone, and is therefore identical to that in a pure polymer sample deformed at the same strain rate.

As it is reasonable to assume that the stress in the polymer phase is governed by the strain rate, it is concluded that this stress is identical for composite and pure polymer samples since the test is done at identical strain rate. This makes it possible to exploit the pure polymer experiments for identifying the stress in the polymer phase of the composite.

With the above insights it is straightforward to decompose the net load,  $T$ , on a cut surface (area  $A$ ) through the composite, normal to the load axis, into contributions from metal and polymer according to the rule of mixture

$$T = \sigma^{\text{eff}} A = [\varphi \sigma^{\text{M}} + (1-\varphi) \sigma^{\text{P}}] A . \quad (22)$$

The symbols have the following meaning:  $\varphi$  stands for metal volume fraction,  $\sigma^{\text{M}}$  stands for stress in the metal and  $\sigma^{\text{P}}$  stands for stress in the polymer. An analogous equation is known to apply to the axial strength of fiber-reinforced composites in the limit of very long aligned fibers.<sup>[97]</sup>

The consistency of equation 22 with our data may be checked by inspecting its implications for the strength of the metal ligaments. To this end, Eq. 22 is rearranged into

$$\sigma^M = [\sigma^{\text{eff}} - (1-\varphi) \sigma^P] / \varphi \quad (23)$$

which affords a computation of the metal flow stress from the data for  $\varphi$ ,  $\sigma^P$ , and  $\sigma^{\text{eff}}$  that are measured for the composite and pure polymer samples. Figure 20 shows  $\sigma^M$  obtained in this way. The data is for the deformation at net engineering strain  $\varepsilon_E = 0.1$ , the smallest strain value where the flow stress of all composite samples first tends towards a nearly stationary value. It is seen that samples with ligament size  $L = 20$  and  $50$  nm yield values of  $\sigma^M$  that agree closely (the data for all three composites at  $L = 20$  nm actually superimpose in the graph), independent of the nature of the polymer. This finding is consistent with the notion that the flow stress is characteristic of the metal, and is therefore supportive of the stress decomposition strategy as embodied in Eq. 23.

Figure 20 also includes data for the strength of nanoporous gold ligaments that are estimated from the compression and microhardness tests of Ref.[19].<sup>1</sup> The analysis find that the estimated  $\sigma^M$  values of the composites are of similar magnitude as those estimated for pure nanoporous gold in Ref. [19] which used the same npg synthesis protocol, and in particular the trend of smaller is stronger is reflected by the composite. Overall, this finding gives further support to our data analysis.

Closer inspection of Figure 20 shows that the size-dependence of strength in the composite is somewhat less than what is inferred from pure nanoporous gold. One might speculate on a dependency of the polymer properties on the ligament size, which is ignored in our data analysis. Reconciling the data for strength derived from composite samples and derived from pure nanoporous gold in this way would require that the polymer phase in the composite at small ligament size is weaker than bulk polymer. A weakening at small ligament size might be understood in terms of incomplete curing. This might result from depletion of the resin/hardener mixture in hardener if the hardener molecules would be adsorbed at the ligament surface. The small- $L$  composites have more surfaces per volume and may, therefore, be more prone to this process. In fact, examining the material with  $L = 40$  nm as an example and using the supplier's data for the number-density of amine groups in the hardener, we find that the resin in the pore space contains 300 times fewer hardener molecules than Au surface atoms. This implies that, in principle, all hardener molecules could entirely be withdrawn from the resin by adsorption on the Au surface. Obviously, that extreme scenario is not compatible with the mechanical strength of the composite samples in our study. Yet, the finding - in Figure 20 - of a reduced apparent strength of the polymer component does support a certain degree of hardener depletion at small  $L$ . Studies with systematic addition of extra hardener are in preparation to explore this issue.

---

<sup>1</sup> The data of Fig. 3B of Ref. [19] is used. As indicated there, the Gibson-Ashby scaling relation for the strength,  $\sigma^{\text{eff}} = 0.3\sigma^M\varphi^{3/2}$ , was used to estimate the local strength of the metal ligaments from the effective macroscopic mechanical behavior.

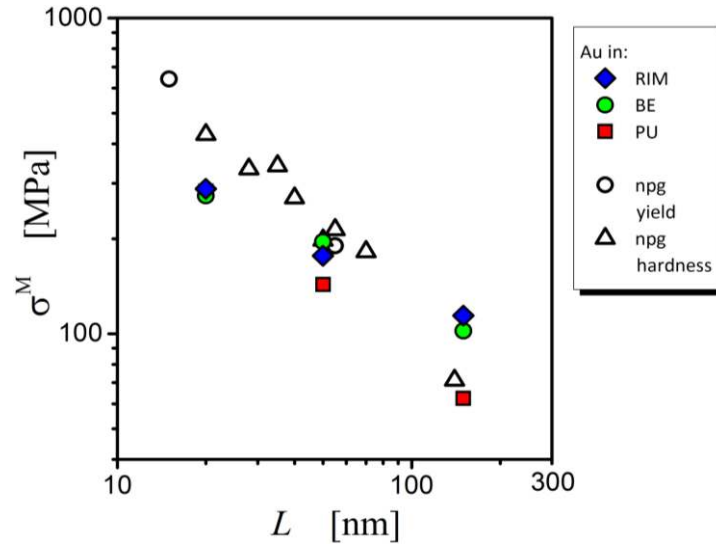


Figure 20: The metal flow strength,  $\sigma^M$ , of the ligaments that are obtained according to eq. 23 as a function of ligament size,  $L$ , for RIM-npg (filled diamond), BE-npg (filled circle) and PU-npg (filled square) composite samples, and the metal flow strength of ligaments for nanoporous gold that are estimated from the compression (open circle) and microhardness tests (open triangle) of Ref.[19] versus ligament size.

### ***Metal flow stress: work hardening***

Figure 21 displays graphs of  $\sigma^M$  at different deformed strain versus true strain,  $\varepsilon_T$ , for RIM-npg, BE-npg and PU-npg composites with different ligament size. It suggests that the ligament strength increases with decreasing ligament size in composites, which confirms that the composites follow the trend of “smaller is stronger”.

For pure npg samples, it is difficult to distinguish the initiative of the increase of the strength during compressive deformation. It can be derived either from the work hardening of the individual nanoscale ligament at the microscopic scale or from the work hardening macroscopically caused by the densification of the network of the ligament. In contrast, the interpenetrating polymer in composites prevents the densification, which gives a chance to study the work hardening of the ligament in this work. In Figure 21, a linear work hardening law at the larger strains and larger ligament sizes were observed. It seems that the formula  $\sigma = \sigma_0 + H\varepsilon$ , where  $H$  stands for the work hardening coefficient, is best suited for observation from a number of various conceivable work hardening laws. The  $H$  was evaluated from the slop of stress-strain curve at the larger strains ( $\varepsilon_T$  of 0.2-0.6) in Figure 21 and tabulated in Table 3. It shows that the work hardening coefficient is more significant for large ligament. The work hardening of the ligament results in the increase of the  $\sigma^M$  at larger deformation.

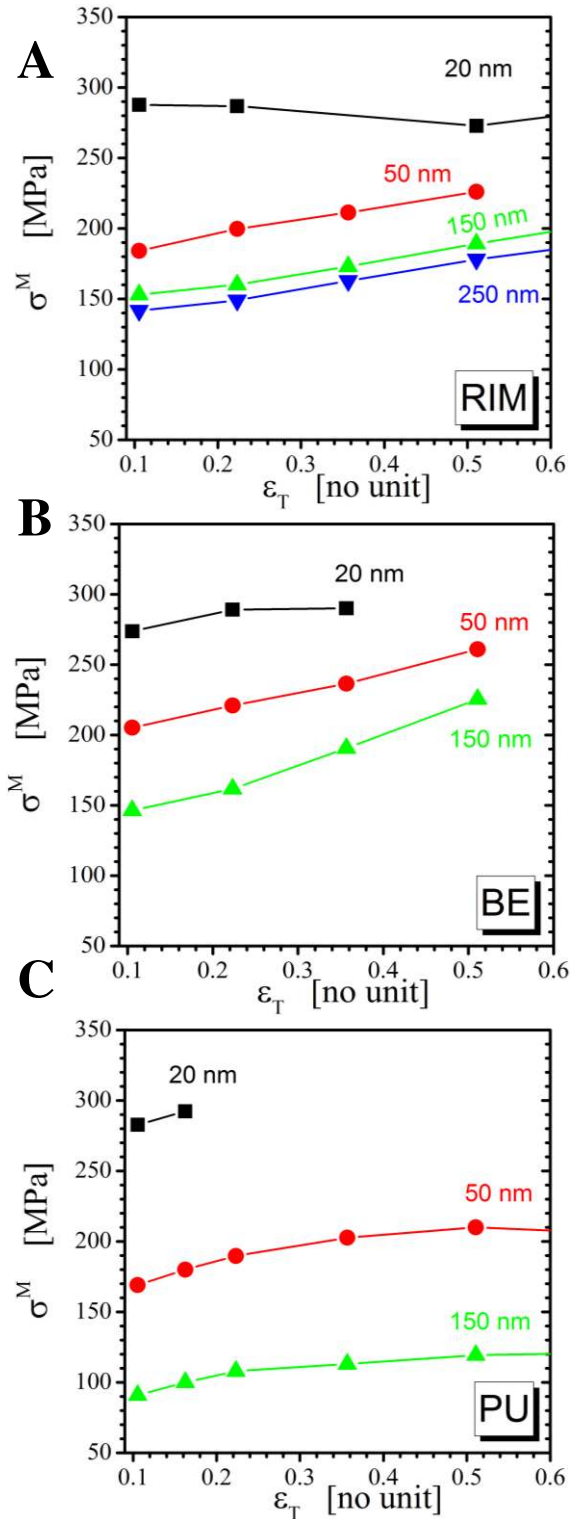


Figure 21: The metal flow stress,  $\sigma^M$ , of ligament at different deformed strain plotted versus true strain,  $\epsilon_T$ , for RIM-npg (A), BE-npg (B) and PU-npg (C) composites with different ligament size.

Table 3: The work hardening coefficient,  $H$ , which is evaluated from the slope of stress-strain curve at the larger strains in Figure 21, for different types of polymer-npg composites with different ligament size,  $L$ .

	$L$ [nm]	$H$ [MPa]
RIM-npg composite	20nm	-38
	50nm	91
	150nm	101
	250nm	101
BE-npg composite	20nm	63
	50nm	136
	150nm	198
PU-npg composite	20nm	-
	50nm	98
	150nm	64

## 4.2 Tension

### 4.2.1 Experimental results

#### 4.2.1.1 Three-point bending test

Previous research and sources show a relatively low number of studies devoted to tensile test of macroscopic nanoporous gold due to a limited access to the equipment suitable for tension test of npg. Mostly researchers studied the failure behavior of nanoporous gold by three-point bending test<sup>[5, 19, 35]</sup>. As a preliminary test of tensile behavior three-point bending experiments were performed for the native npg and the BE-npg composite. Both samples are with ligament size of 150 nm. The stress concentrated under the center of the loading point. Photographs of the as-tested samples are shown in Figure 22. For native npg, crack propagation is very fast under a small load and failure is observed without any sign of plastic deformation (Figure 22A), supporting previous reports of an intrinsic brittleness of npg materials in tension<sup>[5]</sup>. In striking contrast to the brittle failure of native npg, the BE-npg composite (Figure 22b) can be deformed

with no apparent failure in the compressive and tensile regions of the sample. An evaluation of the bending geometry reveals that the maximum true tensile strain was  $\sim 0.1$ .

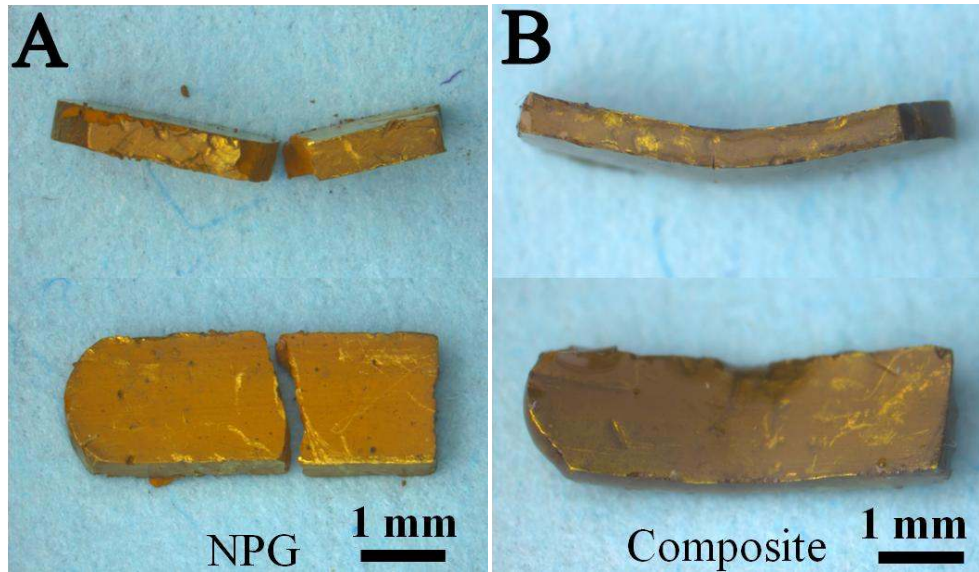


Figure 22<sup>[36]</sup>: Photographs of native npg with ligament size of 150 nm (A) and its composite filled with BE epoxy (B) after the three-point bending tests. Samples are shown edge-on and in top view.

#### 4.2.1.2 Tensile test

To start with, this section discusses tensile stress-strain curves of the pure polymers as presented in Figure 23. While it has been found that the PU and BE have equal strength in tension and compression, the RIM strength in tension is down to half the compression value. From a preliminary compression experiment with strain rate changing, it is apparent that the strain rate sensitivity of RIM is stronger than that of PU. Therefore, it is likely that the strength of RIM epoxy in tension will decrease more as the strain rate changes from  $10^{-4} s^{-1}$  for compression to  $10^{-5} s^{-1}$  for tensile test. All polymers can be deformed to large strain in tension.

The stress-strain curves of tensile tests on the composite samples with ligament size of 50 nm and 150 nm are shown in Figure 24. 0.2%-offset yield stresses,  $\sigma_{0.2}^Y$ , fracture strength and strain were measured and shown in Table 4. The composites are distinguished from pure npg by their noticeable fracture strain. This strain increases with increasing ligament dimensions. The plastic strain to failure is quite small for the RIM-npg samples, but the BE-npg sample with  $L = 150$  nm and all PU samples show appreciable strain, reaching  $> 10\%$  for the PU-composite specimen with  $L = 150$  nm.

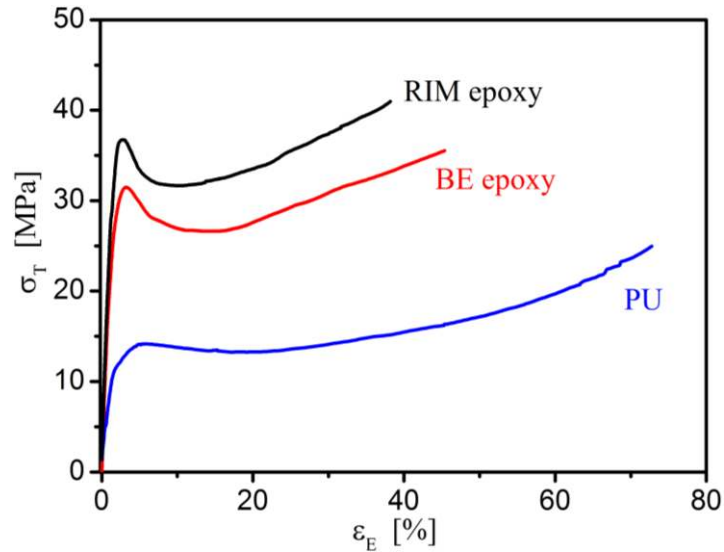


Figure 23: The tensile true stress,  $\sigma_T$ , versus engineering strain,  $\epsilon_E$ , curves of the RIM epoxy, BE epoxy and PU samples of initial dimension  $1 \text{ mm} \times 1 \text{ mm} \times 12 \text{ mm}$  at a nominal strain rate of  $10^{-5} \text{ s}^{-1}$ . Data for yield strength, fracture strength and strain were tabulated in Table 4.

As demonstrated by the compression tests, the composites are stronger in tension than their pure epoxy counterparts. For instance,  $\sigma_{0.2}^Y$  of RIM epoxy-npg with  $L$  of 50 nm is almost 3 times larger than  $\sigma_{0.2}^Y$  of pure RIM epoxy. Furthermore, it is remarkable that the yield stress of composite increases with decreasing ligament size. Similar to  $\sigma_{0.2}^Y$ , the fracture strength also increases with decrease of  $L$ .

Tests with several nominally identical samples found failure mostly within the gauge section, with only occasional failure events at the gripping shoulder. Figure 25 shows photographs of as-tested sample. It shows surface grooves from wire-drawing and small defects which results from handling the nanoporous gold samples in their as corroded and has annealed states, prior to infiltration with the polymer.



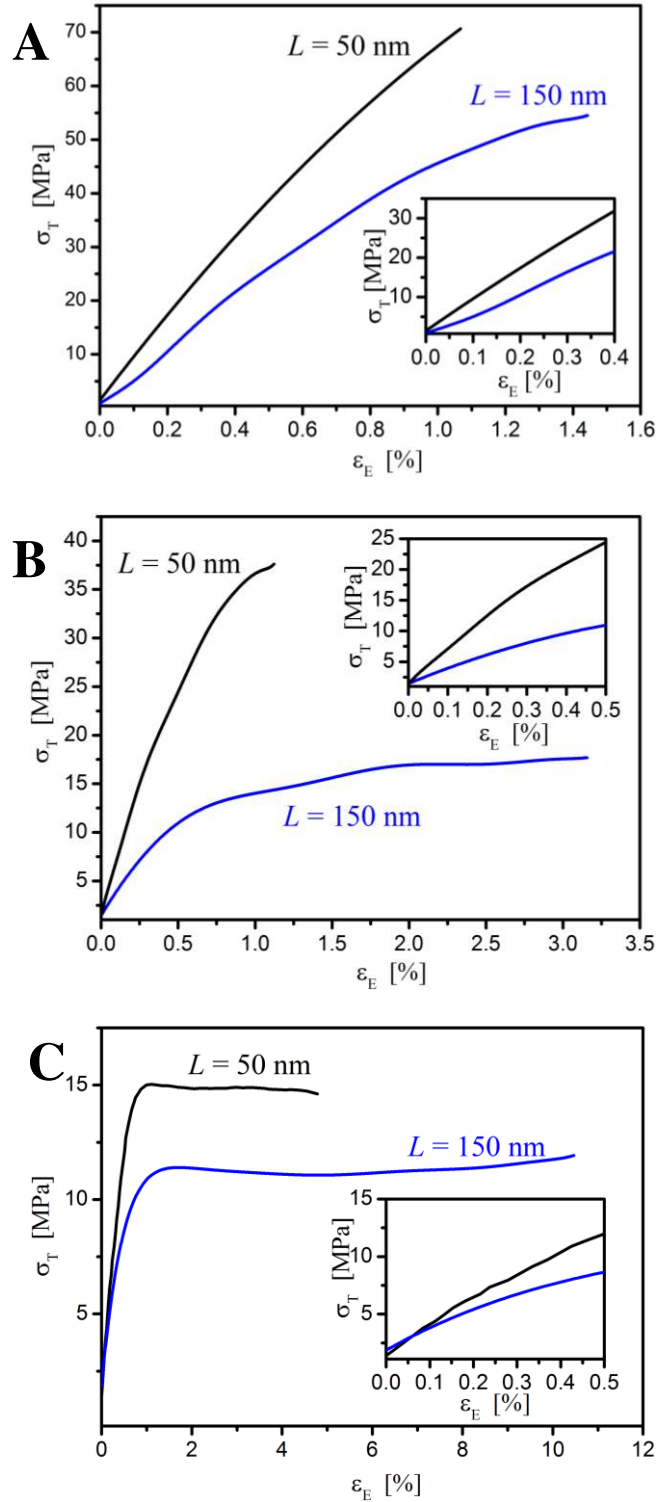


Figure 24: The tensile true stress,  $\sigma_T$ , versus engineering strain,  $\varepsilon_E$ , curves of the samples of initial dimension  $\sim 1.2 \text{ mm}^2 \times 12 \text{ mm}$ : (A) RIM-npg, (B) BE-npg and (C) PU-npg composites with ligament size,  $L$ , of 50 nm and 150 nm at a nominal strain rate of  $10^{-5} \text{ s}^{-1}$ . Data for yield strength, fracture strength and strain are tabulated in Table 4.

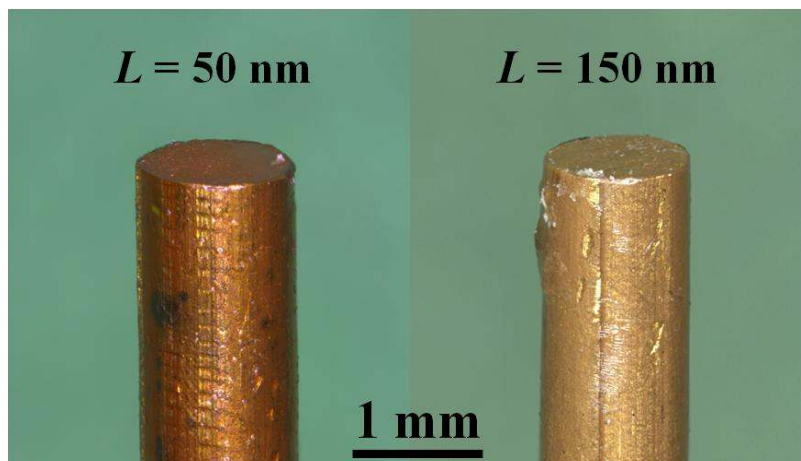


Figure 25: Photographs of fractured RIM based-composite samples from tensile tests with different ligament size,  $L$ :  $L = 50\text{nm}$  (left) and  $L = 150\text{ nm}$  (right). The top surfaces of samples are fracture surfaces. Some surface grooves and small defects were observed, which results from wire-drawing or handling the nanoporous gold samples prior to infiltration with the polymer.

Table 4: Numerical values of structural and mechanical characteristics in tensile tests of the composites and different polymers.  $L$  – ligament size;  $E$  – elastic modulus,  $\sigma_{0.2}^Y$  - 0.2% offset yield stress.

	$L$ [nm]	$E$ [GPa]	$\sigma_{0.2}^Y$ [MPa]	Fracture stress [MPa]	Fracture strain [%]
RIM-npg composites	50	7.78	69.3±0.5	70.1	1.1
	150	4.87	49.5±0.5	54.5	1.4
epoxy RIM	—	2.75	23.0±1	23.3	38.5
BE-npg composites	50	5.48	33.0±0.5	37.2	1.2
	150	2.47	13.1±0.4	17.7	3.2
BE	—	2.35	21.9±0.5	35.5	45.4
PU-npg composites	50	2.64	14.3±0.6	14.8	5.0
	150	1.61	10.3±0.6	11.9	10.5
PU	—	0.90	8.0±0.1	10.1	73.2

#### 4.2.1.3 Four-point bending test

The motivation for the bending test was the suspicion that surface flaws determined the fracture strength. From Figure 25, some surface flaws on tensile tested samples were observed. However, the geometry of the sample prevented applying a satisfactory polish to optimize the surface. The bending test works with samples that can be brought to higher surface finish and should therefore be stronger. Despite the fact that three-point bending tests are generally easier to perform compared with four-point bending test, in this case four-point bending test was conducted to examine composite material's plastic deformation in tension conditions. Stress concentration of four-point bending tests is over a larger region, avoiding premature failure, whereas the stress concentration of three-point bending test is in small region and concentrated under the center of the loading point.

Four-point bending experiment was performed on the rectangular sample of RIM-npg composite with  $L$  of 150 nm. The sample surface was carefully polished. Photographs of the as-tested sample at non-deformed, maximum bending and final unloaded states are shown in Figure 26. From the middle photo of Figure 26, it can be seen that the composite can be deformed to the displacement of 1500  $\mu\text{m}$ , which is a maximal possible measuring range, with no apparent failure in the compressive or tensile regions of the sample.

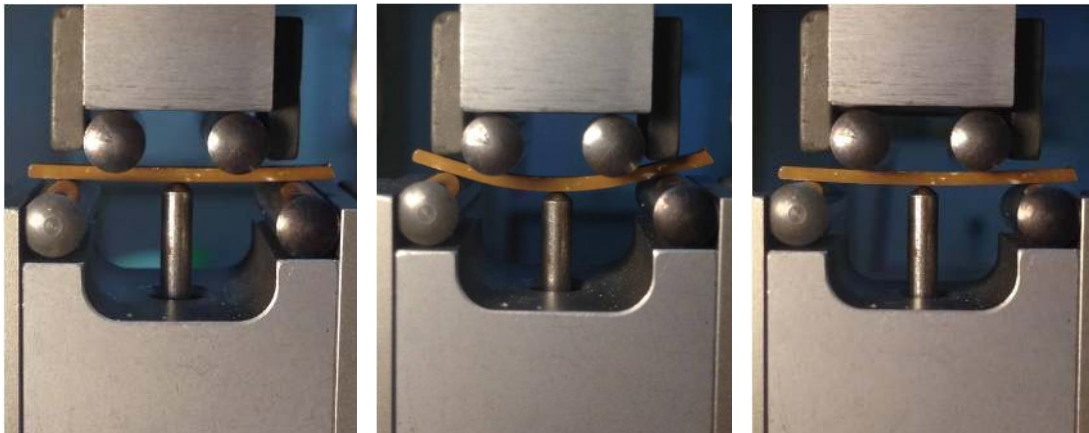


*Figure 26: Photographs of the as-tested RIM-npg composite sample with ligament size of 150 nm at non-deformed (left), maximum bending (middle) and final unloaded (right) states during four-point bending measurement. The sample surface was carefully polished.*

The graph of force,  $F$ , versus displacement,  $\delta$ , was recorded during measurement, which is shown in Figure 27(A). It shows a significantly linear force-displacement behavior. The stress and strain was calculated based on  $F$ - $\delta$  curve according to the equation 18 and 19. At the maximum measuring range, the sample could be deformed at strain of 2% with the stress of 140 MPa, which is stronger and has higher plasticity than the wire-shape RIM-npg sample with  $L$  of 150 nm in tensile test (see in Figure 24(A)).

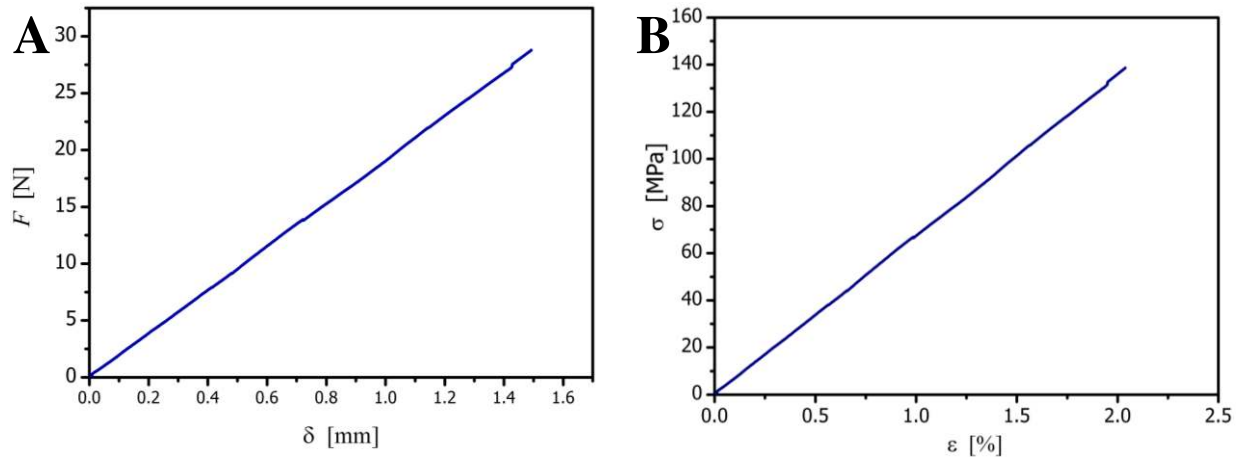


Figure 27: (A) Graph of force,  $F$ , versus displacement,  $\delta$ , which was recorded during four-point bending measurement. (B) The stress,  $\sigma$ , versus strain,  $\epsilon$ , curve of four-point bending test, which was calculated according to the equation 18 and 19.

## 4.2.2 Discussion

### 4.2.2.1 Macroscopic failure behavior of nanoporous gold

Experimental tensile tests so far invariably revealed brittle failure of npg. Balk *et al.*<sup>[29]</sup> developed a testing technique that permits tension tests in small sample volumes. Tests showed that npg exhibit no apparent plastic deformation, even though individual ligaments at the fracture surfaces did deform. Li *et al.*<sup>[5]</sup> investigated npg in three-point bending, linking brittleness to the ratio of sample size to intrinsic pore size. It is a fact that micro- and recently also macroscale nanoporous gold samples exhibit very good deformability properties in compression, still, it has to be added that brittle failure in tension occurs in most studies. This phenomenon has been attributed to a certain property of porous bodies, namely, tension-compression asymmetry of their mechanical behavior.<sup>[36]</sup> Density decrease in tension leads to work softening even though densification of the network would suggest work hardening in compression. The former trend points towards plastic instability with shear localization as well as brittle failure in tension.

Strength and ductility are two of the most important mechanical properties of structural materials. As an ensemble of interconnected ligaments, nanoporous gold offers an implementation of the mechanical properties of nanowires, including specifically their high strength, into a macroscopic material. It has to be added that, even though the nanoscale ligaments are characterized by high local strength, it is crucial that npg are brittle in tension and therefore it is questionable whether they can be regarded as advanced and structural materials. It goes without saying that for ductilization of the material it is important to have a material design able to prevent density change under load.

#### 4.2.2.2 Tension behavior of npg-polymer composite

The discussion in this section will focus on the plastic deformation in tension of composite, because the main motivation of this work is a design of ductile npg reinforced nanocomposites. The results presented in compression section demonstrate that impregnation with a polymer is an efficient method of reducing the density change during plastic flow of nanoporous materials in conditions of uniaxial load. It is conjectured that suppressing the density change would also suppress compression/tension anisotropy of work hardening and the npg-polymer composite should therefore be ductile in tension. In view of the brittle behavior of npg in three-point bending test, it is remarkable that our composite specimens do exhibit ductile deformation. The plastic deformation of the composite in three-point bending testifies to its tensile ductility, which is a promising improvement to the tensile behavior of pure npg material. This drastic enhancement of tensile ductility confirms our strategy. The impregnation indeed leads to ductilization.

The plastic deformation in tension of the composite is investigated under uniaxial loads. As shown in Figure 24, it is found that the amount of plastic deformation of composite in tension depends on the ligament size and the ductility of the interpenetrating polymer. For each type of the composite, plastic deformation prior to failure increases with increasing ligament size. It follows the generic trend of more ductility at lesser strength.<sup>[165]</sup> The different interpenetrating polymer phase makes tensile behavior of composites completely different. The composites follow the trends of the polymer ductility. Noticeable fracture strain was achieved for the PU-based composite, which is a remarkable finding in view of the brittleness of npg samples in all previous studies. However, compared to the deformed strain of polymer in Figure 23, the result is that reinforcing polymer with npg increases the strength of the polymer matrix, but also leads to brittle polymer materials.

Li *et al.*<sup>[5]</sup> determined the fracture strength of 8.2 MPa for millimeter-scale bulk nanoporous gold with ligament size of around 20 nm by carrying out three-point bending tests. Balk *et al.*<sup>[29]</sup> found nearly the same values of tensile yield and fracture strengths measured by tensile testing of bulk npg microspecimens. Both references indicated that npg specimens fractured abruptly in tension test, with no apparent plastic deformation. From the results of bending and tension tests of composite in this work, it has been found that the composite specimens exhibit significantly larger fracture strength. The mechanical features of the composites also follow the trend of “smaller is stronger”.

The comparison of the stress-strain curve of the RIM-npg composite with  $L$  of 150 nm in Figure 24(A) in tension test to that in Figure 27(B) in bending test shows that tensile strength and strain to failure remain low. It appears natural to speculate on the role of the surface finish of the samples on their failure. Microscopic investigation shows surface flaws results from handling the npg samples in their preparation states, prior to infiltration with the polymer. The result of four-point bending test demonstrates that optimized surface equals a stronger and more ductile sample. Figure 27 shows a remarkably linear the force-displacement behavior in four point bending test.

However, the sample cannot be further deformed in such a test because of the measuring range limitations.

# **Chapter 5.**

## **Elastic deformation: A preliminary study**

In this work the elastic deformation behavior of materials was explored with three methods: instrumented indentation test, load-unload compression test and dynamic mechanical analysis. The elastic behavior of interpenetrating polymer phase in composite are affected by a lot of factors which are not studied or illustrated in this chapter, such as frequency, temperature, curing state, ligament size and so on. This chapter only presented a preliminary study of elastic deformation of composite in specific curing state. In future, other mentioned factors should be studied systematically to understand the elastic deformation of the composite.

### **5.1 Experimental results**

#### **5.1.1 Instrumented indentation tests**

The elastic modulus can be determined by analyzing the indentation load-displacement curves of instrumented microhardness test. Figure 28 summarizes the elastic modulus,  $E$ , determined from instrumented hardness tests according to equation 15 for RIM- and PU-based composites and polymers. The elastic modulus of composites is larger than that of its constituent pure polymer. For example, at  $L = 20$  nm the elastic modulus of RIM-npg composite is around 12 GPa, which

is about three times larger than RIM epoxy (around 4 GPa). All the composites are much stiffer than their interpenetrating polymer material. The  $E$  of the composite is ligament size-dependent. It decreases with the increase of  $L$ . For instance, the elastic modulus of the RIM-npg composites with  $L$  of 20 nm, 50 nm and 150 nm is around 9.9 GPa, 10.4 GPa and 11.2 GPa, respectively.

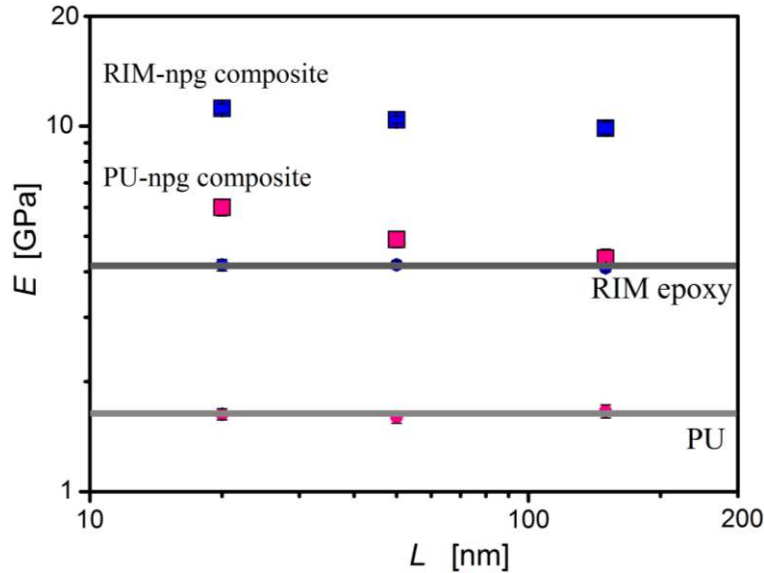


Figure 28: Elastic modulus,  $E$ , evaluated from indentation load-displacement curves of RIM and PU-based composites (squares) and their interpenetrating polymers (circles) versus ligament size,  $L$ . Polymer samples were taken from the same mould as the composites and data are plotted at the respective  $L$ -value. Gray line is a guide to the eye.

### 5.1.2 Load-unload compression tests

Change of elastic modulus during compression was examined in load-unload compression tests. Figure 29(A) shows experimental results of nanoporous gold with ligament size of 20 nm, 50 nm and 150 nm. The graph of true stress versus strain curves of npg is highly consistent with previous results in compression section. Nevertheless, the collected data shows not only the envelope curve of stress compared with strain observed during continuously growing deformation, but also presents intermediate load-unload segments where it is possible to identify the elastic fragment of the deformation. In Figure 29(A), the observation of residual strain after unloading even from quite a small stress indicates early plastic deformation. Figure 29(B) shows the results for elastic modulus of npg determined from load-unload segment, which is plotted vs. engineering strain. It can be seen that the elastic modulus values start out extremely low. Then the plastic compression brings a rapid increase in the modulus. Results of load-unload compression tests for RIM-npg composites with an  $L$  of 50 nm, and RIM epoxy are shown along with the results of npg samples of the same ligament size for comparison (see Figure 29(C)-(D)). It can be seen that the  $E$  of composites is larger than that of native npg and epoxy. The load-



unload segments from which  $E$  is inferred in the compression test exhibit nonlinearity and hysteresis, indicating a partial recovery of the plastic deformation during unloading.

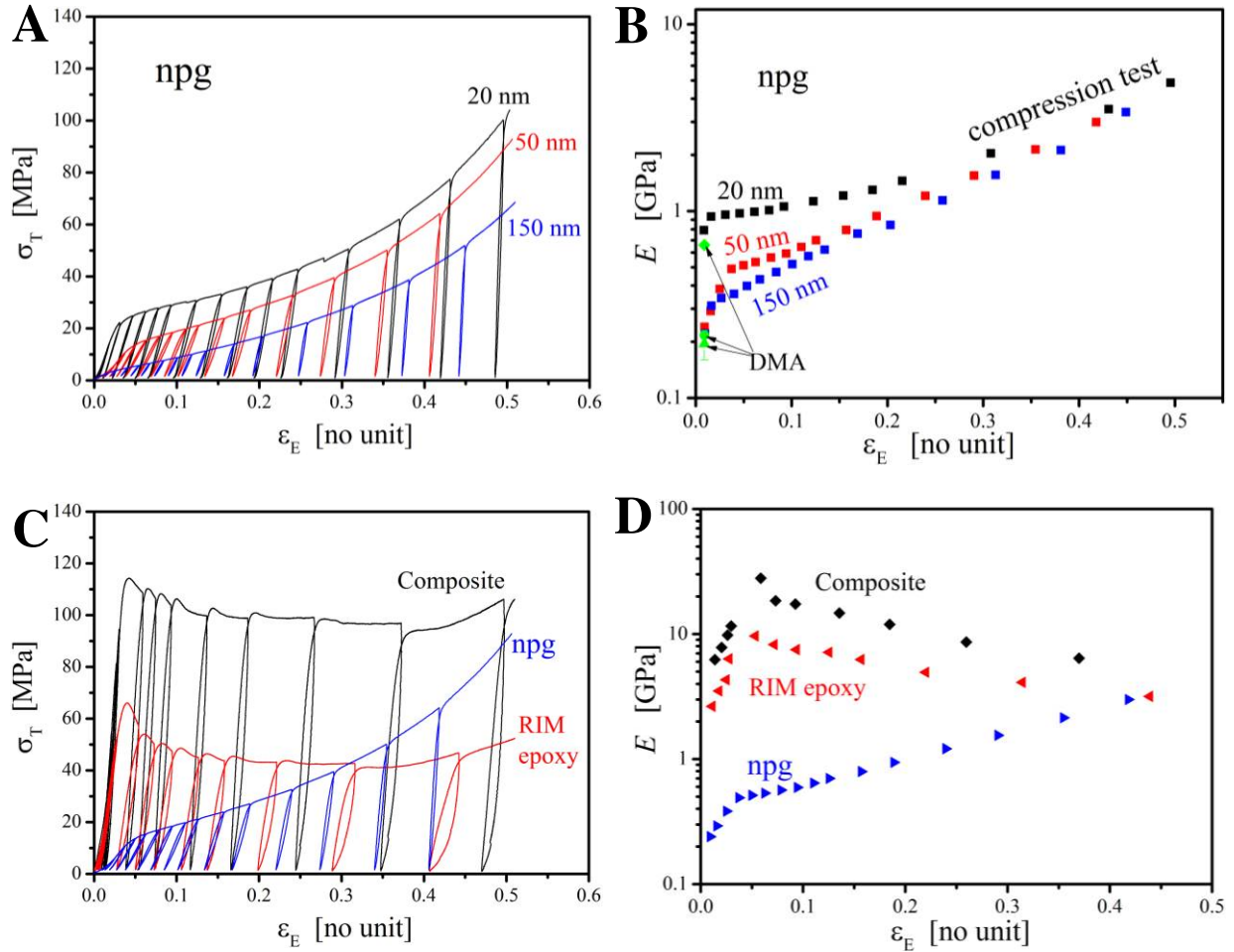


Figure 29: Results of load-unload compression tests: (A) The diagram of load-unload true stress,  $\sigma_T$ , versus engineering strain,  $\epsilon_E$ , for the npg with ligament size,  $L$ , of 20, 50 and 150 nm. (B) Change of elastic modulus,  $E$ , of npg with different ligament size,  $L$ , during load-unload compression (squares). Also shown  $E$  as measured independently in the dynamic mechanical analyzer for the npg samples with  $L$  of 20 nm (green diamond), 50 nm (green circle) and 150 nm (green triangle). The two data sets appear to be consistent. (C) The graph of true stress,  $\sigma_T$ , versus engineering strain,  $\epsilon_E$ , for the RIM-npg composite with  $L$  of 50 nm and its individual constituent RIM epoxy and npg samples. (D) Elastic modulus,  $E$ , determined from the load-unload segments presented in graph (C) versus engineering strain,  $\epsilon_E$ . The unloading curves at minimum applied stress were the source of the engineering strain values.

### 5.1.3 Dynamic mechanical analysis

The modulus measured in dynamic mechanical analysis (DMA) is not exactly the same as the Young's modulus of the classic stress-strain curve. First of all, they are determined in different ways. Young's modulus is calculated from the slope of a stress-strain curve in the initial linear region. By contrast, in case of DMA, a complex ( $E^*$ ), an elastic ( $E'$ ), and an imaginary (loss) modulus ( $E''$ ) are determined from the material response to the sine wave. The various types of moduli help better characterize material's properties, such as its ability to store or return energy ( $E'$ ), to lose energy ( $E''$ ).

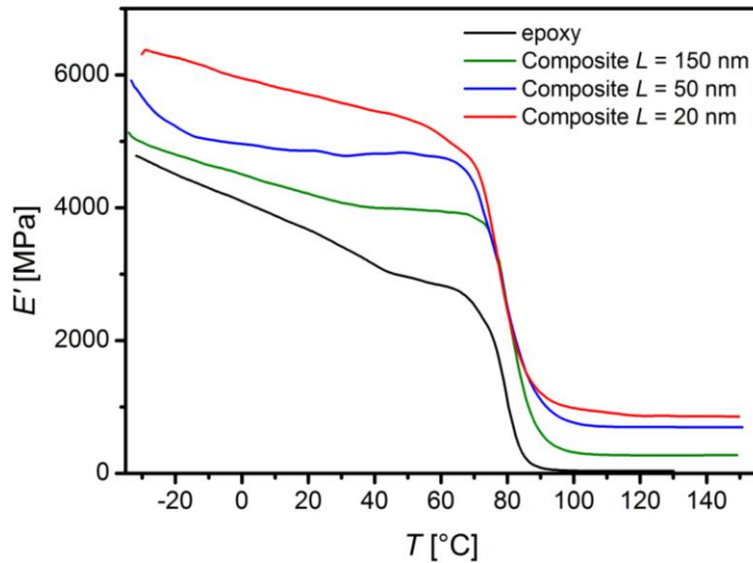


Figure 30: The storage modulus,  $E'$ , of the RIM epoxy and RIM-npg composite with ligament size,  $L$ , of 20, 50 and 150 nm samples versus temperature,  $T$ . All the samples were post-cured at 60°C for 24h. After glass transition, the values of  $E'$  for the RIM-based composites drop drastically.

The macroscopic elastic modulus values obtained by DMA on several npg samples with different ligament size are shown in Figure 29(B) for comparison with the results from the load-unload compression tests. It is apparent that both of the data sets for elastic modulus of npg are consistent. This supports the validity of the DMA data. The section below focuses on studies elastic behaviour of composite and polymer at various temperatures. For thermosets, the degree of cure is a significant parameter in determining the end-use properties, for instance creep or stiffness of a material. Therefore, for stiffness measurement, all the samples were post-cured at 60°C for 24h. The storage modulus,  $E'$ , of the samples versus temperature for post-cured RIM epoxy and RIM-npg composites with different ligament sizes are shown in Figure 30. It can be seen that the  $E'$  of composites at any  $L$  and at any temperature is larger than that of pure RIM

epoxy. It shows that  $E'$  of the RIM-npg composite before transition increases with decreasing the ligament size. For example, at room temperature,  $E'$  of the composites with  $L$  of 20, 50 and 150 nm are 5.6 GPa, 4.8 GPa and 4.1 GPa, respectively. When the temperature is raised to 90 °C (over the  $T_g$ ) the  $E'$  values of the RIM-based composites drop drastically. The  $E'$  of the composites in rubbery state also increases with decreasing the ligament size.

## 5.2 Discussion

### 5.2.1 Elastic modulus of npg

From Figure 29(B), it is apparent that the elastic modulus of npg obtained from DMA and load-unload compression tests at the onset of deformation are consistent. These results agree well with the data of npg with similar ligament size from refs. [166] and [164]. However, as stated in ref. [166], these results for  $E$  of npg are at least one order of magnitude lower than what was deduced in several previous reports on npg. They found  $E$  in the range 3-13 GPa for ligament sizes of 20-40 nm by using nanoindentation, film bending and microtensile or compression tests.<sup>[29, 61, 77]</sup> The npg samples in this work are of the crack-free type that previous studies have shown to be perfectly deformable in compression and to yield strong and ductile nanocomposites when infiltrated with polymer. Therefore, structural imperfections such as native cracks as the origin of the large compliance are ruled out. The origin of the higher stiffness in data by other authors has been discussed by Mameka et al. in reference [166]. These authors suggest the following: The higher stiffness can be explained by densification during loading that occurs in the case of nanoindentation. Another possible reason in the case of thin films may be synthesis. Synthesis by dealloying can be followed by considerable volume shrinkage which leads to densifying and increased stiffness of the material.<sup>[18]</sup> Even in cases when bulk shrinkage is not present, densified layers located near the surface of the macroscopic sample have been found.<sup>[167]</sup> The denser and at the same time stiffer layer constitutes a large part of the sample volume in thin-film samples and it can also affect the whole elastic response. In future studies exact density measurements are needed to help assess the influence of this feature on the npg samples' stiffness.

The analysis of the load-unload segments confirms the pronounced increase in the stiffness of npg as the plastic deformation proceeds (see in Figure 29(B)), as was noted in refs. [164] and [166]. In previous studies, it is significant that npg samples lack transverse plastic strain during compressive deformation, which results in the solid fraction increase during compression. By virtue of the Gibson-Ashby scaling law<sup>[64]</sup> of the modulus with solid volume fraction,  $\phi$ , as  $E \propto \phi^2$ , the densification increases macroscopic stiffness of npg samples. Yet, it is found that the increase is less than the  $\phi^2$  scaling. As was discussed in ref. [164], the npg sample at any state of deformation remains significantly more compliant than it was predicted by the Gibson-Ashby law.

## 5.2.2 Elastic modulus of composite

While studying the mechanical properties of interpenetrating composites, it is necessary to use a theoretical model to describe the relation between its properties and microstructure. For the elastic problem, perhaps Hashin-Shtrikman bound model<sup>[132]</sup> are the most well-known bound for elastic moduli of interpenetrating composite.<sup>[78]</sup> In this model materials were considered to be described as mechanical mixtures of a number of different isotropic and homogeneous elastic phases.<sup>[132]</sup> Considering such a material as quasi-isotropic and quasi-homogeneous when composite has a large enough volume, the elastic moduli of the multiphase material can be estimated in terms of the elastic moduli and volume fractions of the constituting phases.<sup>[132]</sup> The bounds for two-phase material can be presented as the two-sided inequalities:

$$K^*_1 \leq K^* \leq K^*_2, \quad (24)$$

$$G^*_1 \leq G^* \leq G^*_2, \quad (25)$$

where  $K^*$  and  $G^*$  are the effective bulk and shear moduli, respectively<sup>[132]</sup> In this work, the superscript “1” and “2” presents interpenetrating polymer phase and metal phase, respectively. According to Hashin-Shtrikman model<sup>[132]</sup>, the expressions of the effective bulk modulus and shear modulus for the two-phase material can be presented as:

$$K^*_1 = K_1 + \frac{v_2}{\frac{1}{K_2 - K_1} + \frac{3v_1}{3K_1 + 4G_1}}, \quad (26)$$

$$K^*_2 = K_2 + \frac{v_1}{\frac{1}{K_1 - K_2} + \frac{3v_2}{3K_2 + 4G_2}}, \quad (27)$$

$$G^*_1 = G_1 + \frac{v_2}{\frac{1}{G_2 - G_1} + \frac{6(K_1 + 2G_1)v_1}{5G_1(3K_1 + 4G_1)}}, \quad (28)$$

$$G^*_2 = G_2 + \frac{v_1}{\frac{1}{G_1 - G_2} + \frac{6(K_2 + 2G_2)v_2}{5G_2(3K_2 + 4G_2)}}, \quad (29)$$

which can be used in inequalities (24) and (25). The  $v$  is the phase volume fraction. Then the bounds for the elastic modulus,  $E$ , can be obtained by using the usual relation:

$$E = 9GK / (3K + G). \quad (30)$$

In this work, bulk values of (polycrystalline, isotropic) gold were chosen for the elastic parameters of the metal phase. The bulk modulus and shear modulus of bulk gold is 180 GPa and 27 GPa, respectively.<sup>[76]</sup> The elastic modulus of RIM epoxy is obtained from DMA measurement and Poisson's ratio of RIM is 0.35, which is the average value estimated from other literatures.

Figure 31 shows all the previous experimental data of the elastic modulus of the RIM-based composite with  $L$  of 20 nm versus metal volume fraction, together with the Hashin-Shtrikman bounds determined with using equation 24-30. The metal volume fraction for the npg with  $L$  of 20 nm is round 0.27, which has been studied in section 3.1. It can be seen from Figure 31 that all experimental data fall within the Hashin-Shtrikman bound. The model prediction offer upper and

lower bounds to compensate the scatter of the data. The data of elastic modulus for large ligament size samples is not shown in this graph due to the fact that precise solid volume fraction is not determined for these samples. The precise density measurement is indispensable for future studies, in order to assess the role of this parameter for the stiffness of composite samples.

Comparing all of the previously obtained experimental data of the elastic modulus for different ligament size composites, it is concluded that the elastic modulus from the hardness test and ultrasonic velocity measurement correlate really well. And the value of elastic modulus in compression test of a magnitude consistent with that in DMA test. However, it is noted that the  $E$  values in compression and DMA are lower than that in hardness and ultrasonic velocity measurements. Such systematic variations are usually thought to be real and caused by strain rate or frequency dependent stiffness of epoxy. Preliminary study of stiffness of epoxy by DMA in frequency sweep mode found that the stiffness of epoxy increases at higher frequency. Therefore, it is likely that the composites stiffness measured by means of the ultrasonic velocity measurement is higher than that determined with DMA due to the fact that the frequency in ultrasonic velocity tends to be much higher than in case of DMA. At this point, the Hashin-Shtrikman bounds should be recomputed with a higher stiffness value for the pure polymer. However, the required stiffness value of the pure epoxy is not determined yet. In future work, the measurement for the stiffness of epoxy at different frequency is necessary in order to understand the role of this parameter for composite samples' stiffness.

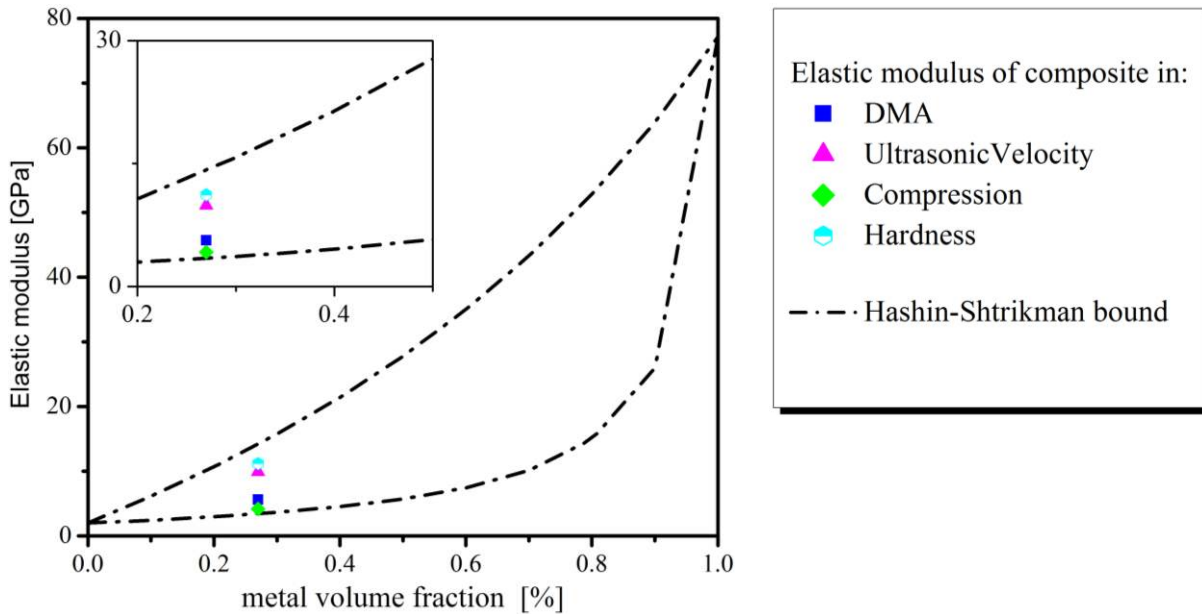


Figure 31: Comparison of experimental data on the elastic modulus of RIM-based composite with ligament size of 20 nm in DMA (square), ultrasonic velocity (triangle), compression (diamond) and hardness (hexagon) measurement with Hashin-Shtrikman bound model as a function of metal volume fraction. The data of elastic modulus of RIM-based composite in ultrasonic velocity was measured by Dr. Grewer at Saarland University, Germany. Experimental data fall within the Hashin-Shtrikman bound.

# Chapter 6.

## Summary and outlook

This work presented a novel type of interpenetrating phase nanocomposite material that exploits the high-strength of metal nanostructures. Dealloying creates macroscopic bodies of a uniform metallic network structure, which is vacuum-impregnated with polymer. Thus formed interpenetrating nanoporous metal-polymer composite material is light-weight, and exhibits a number of unusual and technologically attractive properties, specifically ductility in tension, high electric conductivity and a strength significantly exceeding that of each of the constituent phases.

In recent years, fibre or carbon nanotubes have been widely used as reinforcing materials for polymer based composites. However, a lot of researches found that despite fibre reinforced polymer composites possess excellent in-plane specific mechanical properties, most traditional fibre reinforced polymer composites suffer from a relatively poor out-of plane performance. The application of carbon nanotubes in the role of fillers in polymer composite systems yields great results, however, there is a risk that the dispersion of carbon nanotubes in polymer matrix will not be homogenous and it can affect the resulting composites' mechanical properties. The presented nanoporous metal reinforced composite in this work has great potential for future development owing to its special reinforcement structure which is a uniform metallic network structure. Compared to traditional fibre reinforced polymer composites or carbon nanotubes reinforced polymer composites, this novel interpenetrating nanoporous metal-polymer composite exhibits more homogeneous, isotropic mechanical behavior, opening up the way to further interesting application options.

In this study, the metal host structure is nanoporous gold. Three kinds of polymer were used for infiltration: Bisphenol A epoxy resin, bisphenol F epoxy resin and polyurethane. Evaluation of

SEM images on fracture surfaces of composites reveals mean ligament diameters,  $L$ , of around  $20\pm 5$  nm in the as-prepared material. Samples with different  $L$  could be prepared by annealing in air at  $300\text{ }^\circ\text{C}$  for different times. The complete infiltration was confirmed by the SEM images of polished cross-sectional surfaces of npg and composites samples. It has to be noted that in SEM images the polymer phase is not visible, however, the conservation of the metal nanostructure is a clear sign of its presence. To be more precise, the polished surfaces of native npg look dense and featureless in the SEM due to the fact that the polishing process causes damage to the delicate ligament structure. On the other hand, for composites of different ligament size the ligament structure is perfectly preserved at the composites' polished surfaces. The observation of stable nanoporous microstructures after polishing can only be understood in terms of complete impregnation. TEM and AFM images of cross-section of composite proved the presence of polymer and further confirmed the complete infiltration. Extensive investigations of cross-sectional micrographs revealed no voids in the polymer.

The interpenetrating polymer phase of composite exhibits a glass transition temperature, above which the properties of material such as stiffness degrade significantly. The glass transition temperature is often seen as the upper limit for the use of polymeric composites in order to assure that the mechanical properties is satisfactory in structural application. In this work,  $T_g$  of material is measured by dynamic mechanical analysis. The  $T_g$  of pure epoxy is larger than that of composites. It could be explained by the depletion of the amine hardener in resin/hardener mixture due to the chemisorption of the amine hardener on the gold ligament surface. In addition to this, in case of composites of small ligament size, a decrease in glass transition temperature occurred. It can be possibly down to the growing of the surface-volume ratio for composites of small ligament size. The increase in amine hardener depletion is obtained through the lowering of ligament size and consequently, increasing the surface.

The compression data confirm the trends from the hardness tests, in particular *i*) the strengths of both, npg and composite samples, increase with decreasing  $L$  and *ii*), the composite material at any value of  $L$  is much stronger than each of its constituents. The compression tests showed clearly that suppression of the densification of the ligament network can be achieved by impregnation with polymer. It is particularly important because the densification is the source of work hardening in the process of plastic compression. Indeed, the stress-strain curves in compression evidence a drastic reduction of the work hardening for the composite material. The compression tests also demonstrate interesting mechanical properties of the composites, which maintain the large deformability of npg, and reflect the enhancement of strength with decreasing ligament size. It is suggested that the improved strength of the nanoscale ligaments means improved mechanical properties of composites. This confirms the main design strategy in this work that yield high strength nanocomposites by exploiting the mechanical properties of metal nanostructure. SEM images of microstructure of compressed samples prove that impregnation with polymer changes the mode of deformation of the metal. Pure nanoporous metal is comparable to conventional metal foam in the sense that it may become deformed in low stress conditions due to local bending of the ligaments. As opposed to pure porous metal, the ligaments

in the composite are forced to strain together with the volume-conserving macroscopic flow field by the embedding in a composite matrix.

Testing nanoporous gold or the composite material of this thesis in tension is a serious challenge in view of the smallness of nanoporous gold samples, their lack of machineability, and their brittleness. A major task of this work that designs a protocol for preparing and examining cm-sized bulk samples in tension has been successfully achieved. The tensile ductility behavior of npg-based composites with various polymers was explored. The composite's plastic deformation in tension is a proof of its tensile ductility, despite the fact that native npg is confirmed to be brittle in tension, as shown in the three-point bending test. The finding is important since it confirms the strategy that the impregnation of npg with a polymer leads to ductilization. Regardless of the composite type, the larger the ligament size, the higher the increase in plastic deformation preceding failure which agrees with the more ductility at lesser strength trend. Moreover, the composites follow the polymer ductility trend. A particularly important finding was achieving a noticeable fracture strain in case of the PU-based composite, which is remarkable finding in view of the brittleness of npg samples recorded in previous research. The four-point bending test works on samples with higher surface finish confirmed that surface flaws determine fracture strength in tension and the sample with optimized surface is stronger.

In this work, the consistency of elastic modulus of npg obtained by DMA and load-unload compression tests at the beginning of deformation has been observed. These results are a magnitude consistent with that in ref. [166] and [164]. The elastic modulus data confirms that the composite material is stiffer than each of its constituents. All experimental data of elastic modulus from different methods for npg with  $L$  of 20 nm are compared with the Hashin-Shtrikman bounds model. According to the model prediction, there are upper and lower bounds that compensate for the scattering of data. The experimental data fall within the Hashin-Shtrikman bound. It suggests that it is possible to estimate the composite's elastic modulus with the help of Hashin-Shtrikman bounds. In future studies, it is necessary to measure the precise metal solid volume fraction in assessing the role of this parameter in the stiffness of composite samples.

The present results demonstrate that the compression-tension anisotropy of the work hardening – which leads to instable plastic flow and brittleness in tension – can be suppressed by impregnation the pore space of npg with a polymer. Indeed, a considerable reduction of the work hardening for the composite material is observed in compressive stress-strain curves. Furthermore, tensile ductility of composite is confirmed by the composite's plastic deformation in tension as well as bending tests. These findings, along with the high electric conductivity, have several important implications:

- 1) The materials design strategy in this work points the way towards implementing the high strength of metal nanowires in to a macroscopic structural material. Ligament sizes,  $L$ , in npg can be tuned down to 4-5 nm,<sup>[8, 10]</sup> almost a factor of 3 smaller than the present material, while the compressive ductility and low mass density are maintained.<sup>[19]</sup> Even smaller ligament sizes have been reached when the surface was covered with an atomic monolayer of stabilizing



oxygen species.<sup>[9]</sup> Due to its size-dependence, the strength of the metal phase may be enhanced in such porous materials. Strength can be further enhanced by embedding massive dendritic reinforcements into the porous metal.<sup>[31]</sup> Thus, nanoporous metal based composite materials may reach higher strength than what is reported in the present work.

2) It is remarkable that the composite is substantially stronger and harder than each constituent phase individually. As discussed above, the finding may partly relate to a change in the mode of deformation of the metal, emphasizing axial flow of the ligaments over bending. Yet, other factors may also contribute, such as strengthening by interfacial phenomena. For the nanoporous metal this has been demonstrated by reversible switching of the strength when npg is wetted by an electrolyte and electric charge or adsorbate layers at the surface controlled via the electrode potential.<sup>[16]</sup> Bonds with functional groups of the amine hardener may have a similar effect, such as strengthening of the metal on top of the size-effect. For the polymer, it is well known that the structure in layers – the “interphase” – near the interface with another solid differs from bulk,<sup>[168, 169]</sup> and this may further affect the strength. These considerations point toward interesting size effects to be explored in future studies with smaller structure size.

3) The finding in this work confirms the strategy that the impregnation of nanoporous metal with a polymer leads to ductilization. The ductility of the composites depends on the ligament dimension of npg and the interpenetrating polymer phase. Different polymeric composites were explored and it was shown that - depending on the nature of the polymer - good ductility can be achieved. For composite specimens, the amount of plastic deformation prior to failure increases with increasing ligament size. The noticeable ductile behavior of composite achieved with the PU phase and large ligament size confirms the approach to suppress the npg’s work softening in tension, thereby removing that material’s shear instability and enabling uniform plastic flow in tension.

4) Shaping structural – for instance, fibre-reinforced – composites for application requires time-consuming and labor-intensive curing in a mould. By contrast, the high ductility of the present material suggests shaping by deep-drawing at ambient temperature, a considerably more convenient procedure. Alloy corrosion may be applied to less costly metals, such as Cu or Ni, opening the way to structural nanocomposites for applications that can be manufactured as semi-finished products in sheet form and shaped by conventional drawing, forging or machining.

5) Finally, the material achieves a near metallic conductivity, which makes it suitable for applications where, for instance, static electric charging needs to be avoided or lightning-strike tolerated.

The research in this work implies the deformation behavior of npg-polymer composites can be adapted with respect to the applications by exploiting the mechanical properties of metal nanostructures or by selecting a different type of a component. The strength and ductility of composites can thus be matched to varied structure application. It will be possible to produce light-weights nanoporous metal-polymer composites characterized by adjustable mechanical properties in future. Furthermore, the integration of additional non-mechanical functions will get

more importance. For that purpose, thermal and acoustic insulation or electric conductivity might be realized by the use of different interpenetrating materials.

Alloy corrosion has already been applied to a wide variety of metals, and can yield nanoporous metals with structure sizes well below what was achieved in the present study. At the same time, polymer science offers a wide parameter space in terms of bonding agents and the possible use of thermoplastic or phase-separating materials. Such studies promise insights into size- and interface or interphase effects on the mechanical properties of the metallic and the polymer phases, as well as enables progress towards a new class of strong, ductile and electrically conductive nanocomposites.

# Reference

- [1] M. D. Uchic, D. M. Dimiduk, J. N. Florando, W. D. Nix, *Science* **2004**, *305*, 986.
- [2] J. R. Greer, W. C. Oliver, W. D. Nix, *Acta Materialia* **2005**, *53*, 1821.
- [3] C. A. Volkert, E. T. Lilleodden, D. Kramer, J. Weissmueller, *Applied Physics Letters* **2006**, *89*, 061920.
- [4] J. R. Greer, J. T. M. D. Hosson, *Progress in Materials Science* **2011**, *56*, 654.
- [5] R. Li, K. Sieradzki, *Physical Review Letters* **1992**, *68*, 1168.
- [6] J. Erlebacher, M. J. Aziz, A. Karma, N. Dimitrov, K. Sieradzki, *Nature* **2001**, *410*, 450.
- [7] J. Weissmüller, R. C. Newman, H. J. Jin, A. M. Hodge, J. W. Kysar, *Mrs Bulletin* **2009**, *34*, 577.
- [8] J. Snyder, P. Asanithi, A. B. Dalton, J. Erlebacher, *Advanced Materials* **2008**, *20*, 4883.
- [9] H. J. Jin, S. Parida, D. Kramer, J. Weissmueller, *Surface Science* **2008**, *602*, 3588.
- [10] H. J. Jin, X. L. Wang, S. Parida, K. Wang, M. Seo, J. Weissmueller, *Nano Letters* **2010**, *10*, 187.
- [11] J. Biener, A. M. Hodge, J. R. Hayes, C. A. Volkert, L. A. Zepeda-Ruiz, A. V. Hamza, F. F. Abraham, *Nano Letters* **2006**, *6*, 2379.
- [12] P. S. Kumar, S. Ramachandra, U. Ramamurty, *Materials Science and Engineering a-Structural Materials Properties Microstructure and Processing* **2003**, *347*, 330.
- [13] H. Bei, Y. F. Gao, S. Shim, E. P. George, G. M. Pharr, *Physical Review B* **2008**, *77*, 060103.

- [14] A. T. Jennings, M. J. Burek, J. R. Greer, *Physical Review Letters* **2010**, *104*, 135503.
- [15] R. Maass, L. Meza, B. Gan, S. Tin, J. R. Greer, *Small* **2012**, *8*, 1869.
- [16] H. J. Jin, J. Weissmueller, *Science* **2011**, *332*, 1179.
- [17] J. Weissmueller, R. C. Newman, H. J. Jin, A. M. Hodge, J. W. Kysar, *Mrs Bulletin* **2009**, *34*, 577.
- [18] S. Parida, D. Kramer, C. A. Volkert, H. Rösner, J. Erlebacher, J. Weissmueller, *Physical Review Letters* **2006**, *97*, 035504.
- [19] H. J. Jin, L. Kurmanaeva, J. Schmauch, H. Rosner, Y. Ivanisenko, J. Weissmueller, *Acta Materialia* **2009**, *57*, 2665.
- [20] J. Biener, A. M. Hodge, A. V. Hamza, L. M. Hsiung, J. H. Satcher, *Journal of Applied Physics* **2005**, *97*, 024301.
- [21] A. M. Hodge, J. Biener, J. R. Hayes, P. M. Bythrow, C. A. Volkert, A. V. Hamza, *Acta Materialia* **2007**, *55*, 1343.
- [22] J. Biener, A. Wittstock, T. F. Baumann, J. Weissmüller, M. Bäumer, A. V. Hamza, *Materials* **2009**, *2*, 2404.
- [23] D. Kramer, R. N. Viswanath, J. Weissmüller, *Nano Letters* **2004**, *4*, 793.
- [24] J. Biener, A. Wittstock, L. A. Zepeda-Ruiz, M. M. Biener, V. Zielasek, D. Kramer, R. N. Viswanath, J. Weissmüller, M. Baumer, A. V. Hamza, *Nature Materials* **2009**, *8*, 47.
- [25] N. V. Lavrik, C. A. Tipple, M. J. Sepaniak, P. G. Datskos, *Chemical Physics Letters* **2001**, *336*, 371.
- [26] X. Y. Lang, L. Y. Chen, P. F. Guan, T. Fujita, M. W. Chen, *Applied Physics Letters* **2009**, *94*.
- [27] Y. Ding, M. W. Chen, J. Erlebacher, *Journal of the American Chemical Society* **2004**, *126*, 6876.
- [28] C. X. Xu, J. X. Su, X. H. Xu, P. P. Liu, H. J. Zhao, F. Tian, Y. Ding, *Journal of the American Chemical Society* **2007**, *129*, 42.
- [29] T. J. Balk, C. Eberl, Y. Sun, K. J. Hemker, D. S. Gianola, *JOM* **2009**, *61*, 26.
- [30] C. C. Yang, H. Nakae, *Journal of Alloys and Compounds* **2000**, *313*, 188.
- [31] H. J. Jin, D. Kramer, Y. Ivanisenko, J. Weissmueller, *Advanced Engineering Materials* **2007**, *9*, 849.
- [32] M. Hakamada, M. Mabuchi, *Materials Letters* **2008**, *62*, 483.
- [33] M. Hakamada, M. Mabuchi, *Scripta Materialia* **2007**, *56*, 1003.
- [34] J. Biener, A. M. Hodge, A. V. Hamza, *Deformation Behavior of Nanoporous Metals*, Micro and Nano Mechanical Testing of Materials and Devices, Deformation Behavior of Nanoporous Metals, Springer, New York, **2007**.

- [35] J. Biener, A. M. Hodge, A. V. Hamza, *Applied Physics Letters* **2005**, 87.
- [36] K. Wang, J. Weissmuller, *Advanced Materials* **2013**, 25, 1280.
- [37] W. Haiss, J. K. Sass, *Langmuir* **1996**, 12, 4311.
- [38] H. Lechtman, *Scientific American* **1984**, 250, 56.
- [39] R. B. Brahms, *Trans. Am. Electrochem. Soc* **1992**, 42, 39.
- [40] Pickerin.Hw, C. Wagner, *Journal of the Electrochemical Society* **1967**, 114, 698.
- [41] Pickerin.Hw, *Journal of the Electrochemical Society* **1968**, 115, 143.
- [42] A. J. Forty, *Gold Bulletin* **1981**, 14, 25.
- [43] A. J. Forty, G. Rowlands, *Philosophical Magazine a-Physics of Condensed Matter Structure Defects and Mechanical Properties* **1981**, 43, 171.
- [44] A. J. Forty, P. Durkin, *Philosophical Magazine a-Physics of Condensed Matter Structure Defects and Mechanical Properties* **1980**, 42, 295.
- [45] K. Sieradzki, R. R. Corderman, K. Shukla, R. C. Newman, *Philosophical Magazine a-Physics of Condensed Matter Structure Defects and Mechanical Properties* **1989**, 59, 713.
- [46] J. Rugolo, J. Erlebacher, K. Sieradzki, *Nature Materials* **2006**, 5, 946.
- [47] D. Artymowicza, R. Newmana, J. Erlebacherb, *ESC Transactions* **2007**, 3, 499.
- [48] R. C. Newman, S. G. Corcoran, J. Erlebacher, M. J. Aziz, K. Sieradzki, *Mrs Bulletin* **1999**, 24, 24.
- [49] K. Sieradzki, *Journal of the Electrochemical Society* **1993**, 140, 2868.
- [50] N. A. Senior, R. C. Newman, *Nanotechnology* **2006**, 17, 2311.
- [51] M. Hakamada, M. Mabuchi, *Nano Letters* **2006**, 6, 882.
- [52] J. R. Hayes, A. M. Hodge, J. Biener, A. V. Hamza, K. Sieradzki, *Journal of Materials Research* **2006**, 21, 2611.
- [53] Y. Sun, K. P. Kucera, S. A. Burger, T. J. Balk, *Scripta Materialia* **2008**, 58, 1018.
- [54] Y. Sun, T. J. Balk, *Scripta Materialia* **2008**, 58, 727.
- [55] Y. Zhong, J. Markmann, H.-J. Jin, Y. Ivanisenko, L. Kurmanaeva, J. Weissmüller, *Advanced Engineering Materials*, n/a.
- [56] E. Detsi, M. van de Schootbrugge, S. Punzhin, P. R. Onck, J. T. M. De Hosson, *Scripta Materialia* **2011**, 64, 319.
- [57] M. Hakamada, M. Mabuchi, *Materials Science Forum* **2007**, 561-565, 1657.
- [58] Y. Ding, Y. J. Kim, J. Erlebacher, *Advanced Materials* **2004**, 16, 1897.
- [59] E. Seker, J. T. Gaskins, H. Bart-Smith, J. Zhu, M. L. Reed, G. Zangari, R. Kelly, M. R. Begley, *Acta Materialia* **2007**, 55, 4593.

- [60] J. Z. Zhu, E. Seker, H. Bart-Smith, M. R. Begley, R. G. Kelly, G. Zangari, W. K. Lye, M. L. Reed, *Applied Physics Letters* **2006**, *89*.
- [61] D. Lee, X. Wei, X. Chen, M. Zhao, S. C. Jun, J. Hone, E. G. Herbert, W. C. Oliver, J. W. Kysar, *Scripta Materialia* **2007**, *56*, 437.
- [62] A. M. Hodge, J. Biener, L. L. Hsiung, Y. M. Wang, A. V. Hamza, J. H. Satcher, *Journal of Materials Research* **2005**, *20*, 554.
- [63] D. Lee, M. H. Zhao, X. D. Wei, X. Chen, S. C. Jun, J. Hone, E. G. Herbert, W. C. Oliver, J. W. Kysar, *Applied Physics Letters* **2006**, *89*.
- [64] L. J. Gibson, M. F. Ashby, *Cellular solids: Structure & properties*, Oxford: Pergamon Press, **1988**.
- [65] A. C. Fischer-Cripps, *Nanoindentation*, Springer, **2004**.
- [66] U. Landman, W. D. Luedtke, J. P. Gao, *Langmuir* **1996**, *12*, 4514.
- [67] G. S. Xu, A. S. Argon, *Philosophical Magazine Letters* **2000**, *80*, 605.
- [68] Y. Sun, J. Ye, Z. Shan, A. M. Minor, T. J. Balk, *Jom* **2007**, *59*, 54.
- [69] B. Wu, A. Heidelberg, J. J. Boland, *Nature Materials* **2005**, *4*, 525.
- [70] K. Gall, J. K. Diao, M. L. Dunn, *Nano Letters* **2004**, *4*, 2431.
- [71] A. Stalder, U. Durig, *Journal of Vacuum Science & Technology B* **1996**, *14*, 1259.
- [72] G. Rubio, N. Agrait, S. Vieira, *Physical Review Letters* **1996**, *76*, 2302.
- [73] G. Rubio-Bollinger, S. R. Bahn, N. Agrait, K. W. Jacobsen, S. Vieira, *Physical Review Letters* **2001**, *87*.
- [74] K. S. Kim, J. Y. Song, E. K. Chung, J. K. Park, S. H. Hong, *Mechanics of Materials* **2006**, *38*, 119.
- [75] R. Dou, B. Derby, *Scripta Materialia* **2008**, *59*, 151.
- [76] R. W. Hertzberg, *Deformation and fracture mechanics of engineering materials*, John Wiley&Sons, New York **1989**.
- [77] A. Mathur, J. Erlebacher, *Applied Physics Letters* **2007**, *90*.
- [78] L. D. Wegner, L. J. Gibson, *International Journal of Mechanical Sciences* **2000**, *42*, 925.
- [79] M. P. Groover, *Fundamentals Of Modern Manufacturing*, John Wiley & Sons, Inc., 111 River Street, Hoboken **2004**.
- [80] A. Le Duigou, P. Davies, C. Baley, *Composites Science and Technology*, *70*, 231.
- [81] R. Malkapuram, V. Kumar, Yuvraj Singh Negi, *Journal of Reinforced Plastics and Composites* **2009**, *28*, 1169.
- [82] X. Li, S. Panigrahi, L. G. Tabil, *Appl. Eng. Agric.* **2009**, *25*, 525.

- [83] H. Ku, H. Wang, N. Pattarachaiyakoo, M. Trada, *Composites Part B: Engineering* **2011**, 42, 856.
- [84] I. Ahmad, A. Baharum, I. Abdullah, *Journal of Reinforced Plastics and Composites* **2006**, 25, 957.
- [85] P. Wambua, J. Ivens, I. Verpoest, *Composites Science and Technology* **2003**, 63, 1259.
- [86] S. Iijima, *Nature* **1991**, 354, 56.
- [87] L. S. Schadler, S. C. Giannaris, P. M. Ajayan, *Applied Physics Letters* **1998**, 73, 3842.
- [88] S. R. Dong, J. P. Tu, X. B. Zhang, *Materials Science and Engineering a-Structural Materials Properties Microstructure and Processing* **2001**, 313, 83.
- [89] R. W. Siegel, S. K. Chang, B. J. Ash, J. Stone, P. M. Ajayan, R. W. Doremus, L. S. Schadler, *Scripta Materialia* **2001**, 44, 2061.
- [90] F. H. Gojny, M. H. G. Wichmann, B. Fiedler, K. Schulte, *Composites Science and Technology* **2005**, 65, 2300.
- [91] J. Sandler, M. S. P. Shaffer, T. Prasse, W. Bauhofer, K. Schulte, A. H. Windle, *Polymer* **1999**, 40, 5967.
- [92] C. A. Grimes, C. Mungle, D. Kouzoudis, S. Fang, P. C. Eklund, *Chemical Physics Letters* **2000**, 319, 460.
- [93] H. Ago, K. Petritsch, M. S. P. Shaffer, A. H. Windle, R. H. Friend, *Advanced Materials* **1999**, 11, 1281.
- [94] B. E. Kilbride, J. N. Coleman, J. Fraysse, P. Fournet, M. Cadek, A. Drury, S. Hutzler, S. Roth, W. J. Blau, *Journal of Applied Physics* **2002**, 92, 4024.
- [95] M. J. Biercuk, M. C. Llaguno, M. Radosavljevic, J. K. Hyun, A. T. Johnson, J. E. Fischer, *Applied Physics Letters* **2002**, 80, 2767.
- [96] J. Hone, M. C. Llaguno, M. J. Biercuk, A. T. Johnson, B. Batlogg, Z. Benes, J. E. Fischer, *Applied Physics a-Materials Science & Processing* **2002**, 74, 339.
- [97] J. N. Coleman, U. Khan, W. J. Blau, Y. K. Gun'ko, *Carbon* **2006**, 44, 1624.
- [98] W. D. Callister, *Materials Science And Engineering: An Introduction*, John Wiley & Sons, **2007**.
- [99] J. C. Halpin, J. L. Kardos, *Polymer Engineering and Science* **1976**, 16, 344.
- [100] M. A. L. Machado, L. Valentini, J. Biagiotti, J. M. Kenny, *Carbon* **2005**, 43, 1499.
- [101] G. G. Tibbetts, C. P. Beetz, *Journal of Physics D-Applied Physics* **1987**, 20, 292.
- [102] K. Hata, D. N. Futaba, K. Mizuno, T. Namai, M. Yumura, S. Iijima, *Science* **2004**, 306, 1362.
- [103] E. W. Wong, P. E. Sheehan, C. M. Lieber, *Science* **1997**, 277, 1971.
- [104] M. F. Yu, O. Lourie, M. J. Dyer, K. Moloni, T. F. Kelly, R. S. Ruoff, *Science* **2000**, 287, 637.

- [105] S. S. Xie, W. Z. Li, Z. W. Pan, B. H. Chang, L. F. Sun, *Journal of Physics and Chemistry of Solids* **2000**, *61*, 1153.
- [106] L. Yan, N. Chouw, K. Jayaraman, *Composites Part B: Engineering* **2014**, *56*, 296.
- [107] L. Yan, N. Chouw, X. Yuan, *Journal of Reinforced Plastics and Composites*, *31*, 425.
- [108] K. Charlet, C. Baley, C. Morvan, J. P. Jernot, M. Gomina, J. Breard, *Composites Part a-Applied Science and Manufacturing* **2007**, *38*, 1912.
- [109] K. Oksman, *Journal of Reinforced Plastics and Composites* **2001**, *20*, 621.
- [110] I. Van de Weyenberg, T. C. Truong, B. Vangrimde, I. Verpoest, *Composites Part a-Applied Science and Manufacturing* **2006**, *37*, 1368.
- [111] Q. Liu, M. Hughes, *Composites Part a-Applied Science and Manufacturing* **2008**, *39*, 1644.
- [112] M. Assarar, D. Scida, A. El Mahi, C. Poilane, R. Ayad, *Materials & Design*, *32*, 788.
- [113] S. Liang, P. B. Gning, L. Guillaumat, *Composites Science and Technology*, *72*, 535.
- [114] R. Günther, T. Klassen, B. Dickau, F. Gärtner, A. Bartels, R. Bormann, *Journal of the American Ceramic Society* **2001**, *84*, 1509.
- [115] R. Günther, T. Klassen, B. Dickau, F. Gärtner, A. Bartels, R. Bormann, *Advanced Engineering Materials* **2002**, *4*, 121.
- [116] M. S. Newkirk, A. W. Urquhart, H. R. Zwicker, E. Breval, *Journal of Materials Research* **1986**, *1*, 81.
- [117] M. C. Breslin, J. Ringnalda, J. Seeger, A. L. Marasco, G. S. Daehn, H. L. Fraser, in *Proceedings of the 18th Annual Conference on Composites and Advanced Ceramic Materials—A: Ceramic Engineering and Science Proceedings*, John Wiley & Sons, Inc., **2008**, 104.
- [118] W. Liu, U. Koster, *Materials Science and Engineering a-Structural Materials Properties Microstructure and Processing* **1996**, *210*, 1.
- [119] W. Liu, U. Koster, *Scripta Materialia* **1996**, *35*, 35.
- [120] S. A. Jones, J. M. Burlitch, *Materials Letters* **1994**, *19*, 233.
- [121] C. Toy, W. D. Scott, *Journal of the American Ceramic Society* **1990**, *73*, 97.
- [122] M. K. Aghajanian, J. T. Burke, D. R. White, A. S. Nagelberg, *Sampe Quarterly-Society for the Advancement of Material and Process Engineering* **1989**, *20*, 43.
- [123] F. F. Lange, B. V. Velamakanni, A. G. Evans, *Journal of the American Ceramic Society* **1990**, *73*, 388.
- [124] S. Schön, H. Prielipp, R. Janssen, J. Rödel, N. Claussen, *Journal of the American Ceramic Society* **1994**, *77*, 701.
- [125] H. Prielipp, M. Knechtel, N. Claussen, S. K. Streiffer, H. Muellejans, M. Ruehle, J. Roedel, *Materials Science and Engineering: A* **1995**, *197*, 19.



- [126] M. Knechtel, H. Prielipp, H. Mullejans, N. Claussen, J. Rodel, *Scripta Metallurgica Et Materialia* **1994**, *31*, 1085.
- [127] T. J. Fitzgerald, V. J. Michaud, A. Mortensen, *Journal of Materials Science* **1995**, *30*, 1037.
- [128] J. Roedel, H. Prielipp, N. Claussen, M. Sternitzke, K. B. Alexander, P. F. Becher, J. H. Schneibel, *Scripta Metallurgica Et Materialia* **1995**, *33*, 843.
- [129] F. Peters, *Materials and Methods* **1946**, *23*, 987.
- [130] E. Kopecki, *The Iron Age* **1946**, *157*, 50.
- [131] E. Sachs, H. Guo, E. Wylonis, J. Serdy, D. Baranzio, M. Rynerson, M. Cima, S. Allen, *Rapid Prototyping* **1996**, *2*, 1.
- [132] Z. Hashin, S. Shtrikman, *Journal of the Mechanics and Physics of Solids* **1963**, *11*, 127.
- [133] S. Torquato, G. Stell, *J. Chem. Phys.* **1983**, *78*, 3262.
- [134] S. Torquato, *Journal of Statistical Physics* **1986**, *45*, 843.
- [135] L. V. Gibiansky, S. Torquato, *Journal of the Mechanics and Physics of Solids* **1995**, *43*, 1587.
- [136] S. Torquato, *Applied Mechanics Reviews* **1991**, *44*, 37.
- [137] D. C. Zipperian, in *PACE Technologies Metallographic Handbook*, USA **2011**, 51.
- [138] J. P. Sauer, T. Leonhardt, A. R. Geary, in *1st, United thermal spray conference*, USA **1998**, 959.
- [139] M. Alava, M. Dube, M. Rost, *Advances in Physics* **2004**, *53*, 83.
- [140] S. Gruener, P. Huber, *Journal of Physics-Condensed Matter* **2011**, *23*.
- [141] W. F. Gum, W. Riese, H. Ulrich, Oxford University Press, New York **1992**.
- [142] G. A. L. Oertel, *Polyurethane handbook : chemistry, raw materials, processing, application, properties*, Hanser Publishers ; Distributed in the USA by Macmillan Pub. Co., Munich; New York; New York **1985**.
- [143] G. Woods, *The ICI polyurethane book* John Wiley & Sons, Inc., New York **1990**.
- [144] Y. Breton, G. Desarmot, J. P. Salvetat, S. Delpeux, C. Sinturel, F. Beguin, S. Bonnamy, *Carbon* **2004**, *42*, 1027.
- [145] F. H. Gojny, M. H. G. Wichmann, U. Kopke, B. Fiedler, K. Schulte, *Composites Science and Technology* **2004**, *64*, 2363.
- [146] P. Guo, X. H. Chen, X. C. Gao, H. H. Song, H. Y. Shen, *Composites Science and Technology* **2007**, *67*, 3331.
- [147] M. Aufray, A. A. Roche, *Applied Surface Science* **2008**, *254*, 1936.
- [148] A. P. Dianin, *J. Russ. Phys. Chem. Soc.* **1891**, *23*, 488.

- [149] J. D. Durig, "Comparisons of epoxy technology for protective coatings and linings in wastewater facilities", presented at *The Industrial Protective Coatings Conference and Exhibit*, USA, **1999**.
- [150] U. B. Balachandran, K. T. Hartwig, D. Gubser, V. Bardos, C. A. Baldan, C. Y. Shigue, U. M. C. Maciel, E. R. Filho, in *Advances in Cryogenic Engineering Materials*, Springer US, **2000**, 205.
- [151] O. Bayer, *Angewandte Chemie* **1947**, *59*, 257.
- [152] K. P. Menard, *Dynamic Mechanical Analysis: A Practical Introduction*, CRC Press, Boca Raton, FL, USA **1999**.
- [153] T. Hatakeyama, F. X. Quinn, *Thermal Analysis: Fundamentals and Applications to Polymer Science*, John Wiley & Sons, Inc., Chichester **1999**.
- [154] W. C. Oliver, G. M. Pharr, *Journal of Materials Research* **1992**, *7*, 1564.
- [155] W. C. Oliver, G. M. Pharr, *Journal of Materials Research* **2004**, *19*, 3.
- [156] S. K. Kang, J. Y. Kim, C. P. Park, H. U. Kim, D. Kwon, *Journal of Materials Research* **2010**, *25*, 337.
- [157] [http://www.supermagnete.de/docs/uhu\\_plus\\_endfest\\_300.pdf](http://www.supermagnete.de/docs/uhu_plus_endfest_300.pdf).
- [158] O. A. Bauchau, J. I. Craig, in *Structural Analysis*, Vol. 163, Springer Netherlands, **2009**, 173.
- [159] E. Oberg, F. D. Jones, H. L. Horton, H. H. Ryffel, *Machinery's Handbook*, Industrial Press INC., New York **2000**.
- [160] P. A. Eggertsen, K. Mattiasson, *International Journal of Material Forming* **2010**, *3*, 127.
- [161] Q. F. Cheng, J. P. Wang, J. J. Wen, C. H. Liu, K. L. Jiang, Q. Q. Li, S. S. Fan, *Carbon* **2010**, *48*, 260.
- [162] J.-P. Pascault, H. Sautereau, R. J. J. Williams, J. Verdu, *Thermosetting polymers*, Marcel Dekker, New York **2002**.
- [163] A. L. Volynskii, T. E. Grokhovskaya, V. V. Lyulevich, L. M. Yarysheva, A. V. Bol'shakova, A. S. Kehek'yan, N. F. Bakeev, *Polymer Science Series A* **2004**, *46*, 130.
- [164] N. Huber, R. N. Viswanath, N. Mameka, J. Markmann, J. Weissmuller, *Acta Materialia* **2014**, *67*, 252.
- [165] R. Valiev, *Nat Mater* **2004**, *3*, 511.
- [166] N. Mameka, J. Markmann, H.-J. Jin, J. Weissmueller, *Acta Materialia* **2014**, *76*, 272.
- [167] S. Cattarin, D. Kramer, A. Lui, M. M. Musiani, *Journal of Physical Chemistry C* **2007**, *111*, 12643.
- [168] T. Ramanathan, H. Liu, L. C. Brinson, *Journal of Polymer Science Part B-Polymer Physics* **2005**, *43*, 2269.
- [169] K. I. Winey, R. A. Vaia, *Mrs Bulletin* **2007**, *32*, 314.

# Curriculum Vitae

## Personal Data

<b>Name</b>	Wang
<b>First Name</b>	Ke
<b>Date of Birth</b>	03 May, 1985
<b>Place of Birth</b>	Guizhou, People's Republic of China

## Education

<b>09.1991 - 07.1997</b>	Elementary school in Guizhou, Nanming Elementary School
<b>09.1997 - 07.2000</b>	Junior high School in Guizhou, Guiyang No.18 Middle School
<b>09.2000 - 07.2003</b>	High school in Guizhou, Guiyang No.1 Middle School
<b>09.2003 - 06.2007</b>	Undergraduate study at Department of Polymer Materials and Engineering, Jiangnan University, Jiangsu, China Degree: Bachelor of Engineering Title of Thesis: <i>Preparation and Characterization of Special Morphology of Microsphere PAN/PS-g-PNVA with In-situ Reduction of Silver Nano Particles Immobilized on its Surface.</i>
<b>04.2008 - 07.2010</b>	Graduate study at Polymer Science Program, a joint Master Program of Free University, Humboldt University, Technical University and University of Potsdam, Berlin, Germany Degree: Master of Science Title of Thesis: <i>Comprehensive Characterization of the Shape-Memory Properties of Crosslinked Ethylene-co-Vinyl Acetate Random Copolymers with Variable Crosslink Densities.</i>
<b>11.2010 - 03.2015</b>	Ph.D study at Institute of Materials Physics and Technology, Hamburg University of Technology, Hamburg, Germany Title of Thesis: <i>Composites of Nanoporous Gold and Polymer.</i>